Title
Thermal insulating layers for window energy efficiency

Author
Kou, Rui

Publication Date
2020

UNIVERSITY OF CALIFORNIA SAN DIEGO

Thermal insulating layers for window energy efficiency

A dissertation submitted in partial satisfaction of the
requirements for the degree Doctor of Philosophy

in

Structural Engineering

by

Rui Kou

Committee in Charge:

Professor Yu Qiao, Chair
Professor Shengqiang Cai
Professor Renkun Chen
Professor Veronica Eliasson
Professor Alicia Kim

2020

The dissertation of Rui Kou is approved, and it is acceptable in quality and form for publication on microfilm and electronically:

Chair

University of California San Diego

2020

DEDICATION

To my family.

To all who supported me.

To all who helped me to learn and grow.

TABLE OF CONTENTS

LIST OF FIGURES

LIST OF TABLES

ACKNOWLEDGEMENTS

I would like to express my deepest appreciation to my advisor, Professor Yu Qiao, for his great support and inspiration. His advice and guidance will always be invaluable in my scientific pursuits. I would like to thank my committee members, Professor Veronica Eliasson, Professor Alicia Kim, Professor Renkun Chen, and Professor Shengqiang Cai for their valuable suggestions and time.

Special thanks for Dr. Ying Zhong, who offered important help with this work, and Dr. Meng Wang, Dr. Jeongmin Kim, Mr. Qingyang Wang, Mr. Jian Zeng and Ms. Yun Zhou. Support from other members in the Multifunctional Materials Research Lab, Dr. Yang Shi, Dr. Anh V. Le, Dr. Daniel J. Noelle, Dr. Brian Chow, Mr. Zhaoru Shang, Mr. Kiwon Oh, Mr. Haozhe Yi and Mr. Mingyuan Zhang is also gratefully acknowledged.

I would like to thank my parents for their unconditional support, generous tolerance, and infinite love. I would also like to thank all my friends, who have been standing by my side along the way.

Chapter 2, in part, is a reprint of the material as it appears in Applied Physics Letter. Rui Kou, Ying Zhong and Yu Qiao. Effects of anion size on flow electrification of polycarbonate and polyethylene terephthalate. 115(7), p.073704. The dissertation author was the primary investigator and first author of the paper.

Chapter 3, in part, is currently being prepared to be submitted for publication. Rui Kou, Ying Zhong, Qingyang Wang, Jeongmin Kim, Renkun Chen and Yu Qiao. The dissertation author was the primary investigator and first author of the paper.

Chapter 4, in part, is currently being prepared to be submitted for publication. Rui Kou, Ying Zhong, Qingyang Wang, Jeongmin Kim, Jian Zeng, Renkun Chen and Yu Qiao. The dissertation author was the primary investigator and first author of the paper.

Chapter 5, in part, is a reprint of the material as it appears in Energy and Buildings. Rui Kou, Ying Zhong, Jeongmin Kim, Qingyang Wang, Meng Wang, Renkun Chen and Yu Qiao. Elevating low-emissivity film for lower thermal transmittance. 193, pp.69-77. The dissertation author was the primary investigator and first author of the paper.

Chapter 6, in part, is currently being prepared to be submitted for publication. Rui Kou, Ying Zhong, Qingyang Wang, Yun Zhou, Renkun Chen and Yu Qiao. The dissertation author was the primary investigator and first author of the paper.

VITA

2015 Bachelor of Engineering, Harbin Institute of Technology, Harbin, China

2016 Master of Science, University of California San Diego, USA

2020 Doctor of Philosophy, University of California San Diego, USA

PUBLICATIONS

[1] **Kou, R.,** Zhong, Y., Kim, J., Wang, Q., Wang, M., Chen, R., & Qiao, Y. (2019). Elevating low-emissivity film for lower thermal transmittance. Energy and Buildings, 193, 69-77.

[2] **Kou, R.,** Zhong, Y., & Qiao, Y. (2019). Effects of anion size on flow electrification of polycarbonate and polyethylene terephthalate. Applied Physics Letters, 115(7), 073704.

[3] Zhong, Y., **Kou, R.** (co-first-author), Wang, M., & Qiao, Y. (2019). Electrification mechanism of corona charged organic electrets. Journal of Physics D: Applied Physics, 52(44), 445303.

[4] Wang H., **Kou, R.,** Harrington T., & Vecchio, K. S. (2020). Electromigration Effect in Fe-Al Diffusion Couples with Field-Assisted Sintering. Acta Materialia. In press.

[5] Oh, K., Chen, T., Gasser, A., **Kou, R.,** & Qiao, Y. (2019). Compaction self-assembly of ultralow-binder-content particulate composites. Composites Part B: Engineering, 175, 107144.

[6] Zhong, Y., **Kou, R.,** Wang, M., & Qiao, Y. (2019). Synthesis of centimeter-scale monolithic SiC nanofoams and pore size effect on mechanical properties. Journal of the

European Ceramic Society, 39(7), 2566-2573.

[7] Su, H., Hong, Y., Chen, T., **Kou, R.,** Wang, M., Zhong, Y., & Qiao, Y. (2019). Fatigue Behavior of Inorganic-Organic Hybrid "Lunar Cement". Scientific reports, 9(1), 2238.

[8] Chen, T., Chow, B. J., Zhong, Y., Wang, M., **Kou, R.,** & Qiao, Y. (2018). Formation of polymer micro-agglomerations in ultralow-binder-content composite based on lunar soil simulant. Advances in Space Research, 61(3), 830-836.

ABSTRACT OF THE DISSERTATION

Thermal insulating layers for window energy efficiency

by

Rui Kou

Doctor of Philosophy in Structural Engineering

University of California San Diego, 2020

Professor Yu Qiao, Chair

Polymer-air multilayer (PAM) was developed to improve the building window energy efficiency. It consists of multiple layers of polymer films, separated by spacer bars at the edges. The air gap between adjacent polymer layers is 0.5~1 mm thick. PAM enhances window thermal insulation by suppressing all of conductive, convective, and radiative heat transport. The *U*-factor of a 6-mm-thick 4-layer PAM can be close to or below 0.5 Btu/(h· $\mathrm{ft}^2 \cdot$ °F).

Corona charging and liquid flow electrification were investigated to generate a repulsive pressure of the polymer layers. It helps with materials handling and assembling and improves the structural stability. Dipolar charges can be controlled by the grid voltage in corona charging. Surface charges can be adjusted by liquid flow with appropriate ion size, ion concentration, and flow rate.

To further raise the resistance to radiative heat transfer, a low-emissivity (low-e) coating could be applied on the outer surface of PAM. Because a typical low-e coating would decrease the visual transmittance by more than 20%, in order to keep the overall visual transmittance above 70%, the layer count of PAM should be reduced to 1 or 2. A 4-mm-thick 1-layer PAM or a 3-mm-thick 2-layer PAM could achieve a low *U*-factor around 0.5 $\mathrm{Btu/(h \cdot ft^2 \cdot °F)}$.

Anti-reflection (AR) coating was utilized to maximize the visual transmittance of PAM. The top candidate of the coating material is polymethyl methacrylate (PMMA). With a thin PMMA AR coating, the visual transmittance of 4-layer PAM, 1-layer PAM, and 2-layer low-emissivity PAM were enhanced to 80.3%, 76.9% and 74.5%, respectively. Haze of all the samples was below 1%.

The PAM technology has broad applications not only for building windows, but also for smart walls, roofs, and doors. In addition, it may also be relevant to the automobile, electronics, aerospace, and military industry.

Chapter 1 Introduction

1.1 Window energy efficiency

Currently, there are over 85 million residential and commercial buildings in the U.S. Every year, they account for about 40% of the primary energy consumption and total carbon dioxide emission [1], while 40% (~15 quadrillion British thermal units, shorted as “quads”) of which is associated with building heating, ventilation, and air conditioning (HVAC) [2–4]. With the growth rate of about 1 million new buildings per year, the existing buildings will continue to dominate the market in decades [1,2].

Windows, as one of the most essential and costly elements of the building envelopes, consume about 4 quads of primary energy per year [1,5,6]. Figure 1.1 shows the estimated primary energy use in the four broad Census Bureau regions in the U.S. [7] In the modern buildings, double-pane or triple-pane windows have been adopted for desirable thermal insulation properties. However, 30~40% of present-day windows are still single-pane windows, which are responsible for over 50% of the total window-related energy loss. [8] Windows replacement is high-cost (about $50~100/ft2 [8]) and slow (only 2% of the existing single-pane is replaced per year [9]). If the remaining stock of single-pane windows can be successfully retrofitted, it will reduce the total energy consumption by 1.2 quads per year in the U.S. [1]. Reducing the energy lost through single-pane windows will not only directly economically benefit both residential homes and commercial business, but also mitigate the environmental impacts [10,11].

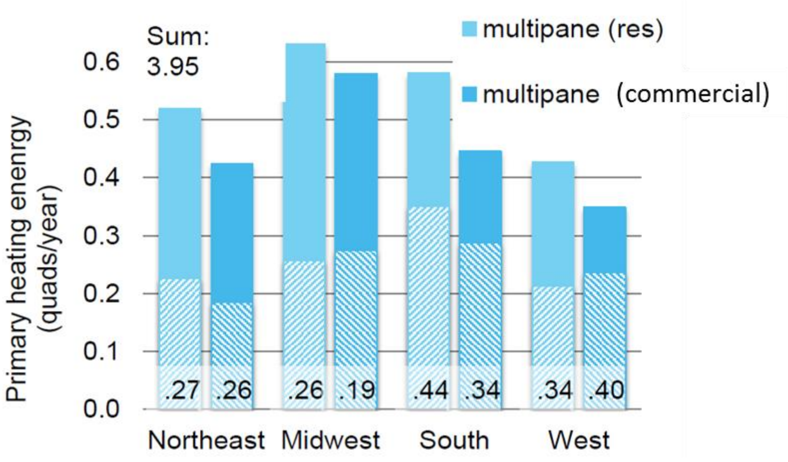

Figure 1.1 Estimated primary energy usage for heat flow through the windows of existing buildings in four U.S. census regions. The results including the energy usage for all of single-pane, double-pane, and multiplane windows in residential and commercial buildings. The area fraction of the single-pane windows in each region is shown at the bottom of each bar. [12]

1.2 Mechanisms of heat loss through window glass

Heat transfer from the room side to the exterior side through window pane happens in three forms: conduction, convection and radiation. Conduction is a type of heat transfer that occurs within a solid, liquid, or gas. For a single-pane window, when there is a temperature difference across it, the heat transfer rate is given by the Fourier law [13]

$$q_{\mathrm{cond}} = -k\frac{\Delta T}{t} \tag{1.1}$$

where ΔT represents the temperature difference, *k* is the thermal conductivity, and *t* is the material thickness.

Convection is heat transfer by the large-scale movement of air, which occurs at the exterior surface, the interior surface, and the air gaps in multipaned pane windows. Heated regions of air will become less dense, and tend to rise. Subsequently, cooler air will take its place. The convective heat transfer rate can be expressed as [14][15]

$$q_{\mathrm{conv}} = h_{\mathrm{conv}}\Delta T \tag{1.2}$$

where h_{conv} is the convective heat transfer coefficient of air.

Radiation refers to heat transfer through electromagnetic waves. When light or heat energy is transfered to the window glass, it would be either reflected or absorbed, and reradiated to both sides. The capacity of the material to absorb and reradiate energy is defined as its emissivity [16]. In winter, when heat is transferred from the room to the window glass, the window reflects a portion of the thermal energy and absorbs the rest. The less heat the window absorbs, the better insulating properties it has. The radiative heat transfer rate at the interior surface of window can be expressed as [17]:

$$q_{\mathrm{rad,in}} = \varepsilon_{\mathrm{P}}\sigma\left({T_{\mathrm{in}}}^4 - {T_{\mathrm{Glass,in}}}^4\right) \tag{1.3}$$

where the Stefan Boltzmann constant $\sigma = 5.67 \times 10^{-8}\,\mathrm{W/m^2K^4}$ and ε_{P} is the surface emissivity of window glass.

The overall heat loss rate with the combined effects of conduction, radiation, and convection is described by the *U*-factor. For single-pane windows, *U*-factor is around 1~1.2 Btu/(h· $\mathrm{ft}^2 \cdot$ °F) [18], which is inefficient for thermal insulation.

1.3 Window retrofitting

Over years, people have investigated a few retrofitting techniques for single-pane windows, to improve the *U*-factor. They are summarized below. In general, all of them suffer issues of high cost or low performance, or both. New technology is needed to offer an economically feasible approach to enhance the building window energy efficiency.

1.3.1 Storm windows

Mounting a storm window onto a single-pane window could be more cost-efficient than replacing it [19–22]. It can help reduce air infiltration, and decrease heat loss. Storm windows can be either installed on the interior of the original window, or on the exterior. In most cases, interior storm windows are more convenience than exterior ones, since installation, disassembling, and maintenance are easier. Moreover, sealing of interior storm windows is generally better. Storm windows can be made of inexpensive plastic sheets for short-term use, or clear glass for long-term use [20]. Wood, aluminum, and vinyl are the most used materials for window frames. To install a storm window, weather stripping should be ensured at all movable joints.

The glass or special plastic sheets and the frame of storm window need to be customized into size, which increases the retrofitting cost. In many cases, water condensation may be formed in the storm windows, which is visually obstructive. More maintenance may be needed if there is a sealing problem in framing.

1.3.2 Low-emissivity coating

Window glass can emit radiative heat in the form of long-wave, far-infrared energy, depending on its surface temperature. Low-emissivity (low-e) coating, a technology commercialized in the 1980s, was designed to prevent the long-wave radiative energy from passing through window glass, while allowing the passage of visual light [1]. Generally, low-e film is a thin, transparent coating, composed of a thin layer of silver or other low-emissivity material that reflects infrared energy [17,23]. When it is applied in the interior surface of a window, in the cold winter, it can help block heat transfer from the room side and halve the energy lost compared to an uncoated window [24]. The emissivity of a standard clear glass is 0.84; i.e., 84% of long-wave radiative energy striking the glass surface can be absorbed and 16% is reflected. In comparison, with a surface emissivity lower than 10%, the low-e coating can reflect ~90% of the radiative energy. [16,23]

However, most low-e films have a natural grey haze and create a slight tint, affecting the window appearance [16,25,26]. Because of the relatively low visual transmittance, occupants would suffer reduced lighting. Moreover, once water condensation is formed on the low-e coating in cold winter, the effectiveness of thermal insulation will be lost [27]. The high materials and installation costs also prevent it from being used more widely.

1.3.3 Aerogels

In the past decade, aerogels were intensively studied, as lightweight, transparent or translucent, highly thermal insulating materials. Among all the aerogels, silica aerogel received the most attention. Silica aerogel is a synthetic porous material, which has an excellent thermal conductivity (k) as low as 0.012 W/(m·K) [28,29], partly due to the high porosity > 90% and partly due to the Knudsen effect of rarified air in nanopores [30,31]. It is made by extracting liquid from the network of a silica gel, and preserving >95% volume of the gel framework by supercritical drying. Well-developed silica aerogels are generally transparent, exhibiting no color and any chromatic aberration, thanks to the nanopore size much smaller than the visual light wavelength [32,33].

Yet, because of its high porosity, silica aerogel has a very low strength and fracture toughness. Its high flexibility and fragility make it irrelevant for window coating applications [34]. To improve the structural integrity, the porosity should be much reduced, but it will result in a drastic increase in thermal conductivity. Once the porosity reaches ~50%, the thermal conductivity would be 0.04~0.1 W/(m·K), much higher than that of air [32]. Moreover, haze of most of silica aerogels is large, due to the pore size distribution [30,31,35–37].

1.4 Polymer-air multilayer

In the current research, we investigated polymer-air multilayers (PAM). PAM is formed by completely separating flat films of transparent polymer by thin air gaps, with spacers on the edges, as depicted in the Figure 1.2. A layer of low-e coating can be applied on the outmost surface. With a low-e coating, because would reduce the visual transmittance by more than 20% [16,23], to keep the overall visual transmittance over 70%, only 1 and 2 layers of polymer should be used. PAM can be classified as: 4-layer PAM, 2-layer low-e PAM, and 1-layer low-e PAM. The multiple polymer films and low-e coating can reduce the radiative heat transfer. The air gap is thinner than 3 mm, wherein the convective heat transfer is trivial. Thanks to the low thermal conductivity of air, the thermal conductivity of PAM can as low as 0.3 W/(m·K). Since all of conductive, convective, and radiative heat transfer paths are suppressed, PAM possesses excellent thermal insulating properties. The optical properties of PAM are also desirable.

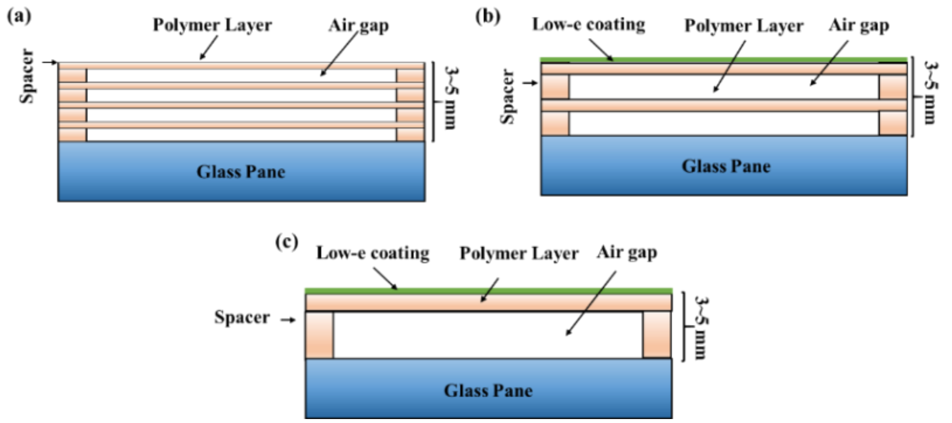

Figure 1.2 Schematics of a) 4-layer PAM, b) 2-layer PAM, and c) 1-layer PAM

1.5 Technoeconomic Analysis (TEA)

1.5.1 Overview

Here, we perform a preliminary analysis of the manufacturing process and cost of polymer-air multilayer (PAM) for a local market of apartments. The purpose is to prove the economic feasibility of this technology.

Assume that on average one apartment has six windows and each window is 2 ft by 3 ft large [38]. The area of the windowpanes is ~36 ft^2 in each apartment. Assume that the average sales in a local area is ~30,000 sets/year, or ~1 million ft^2/year [39].

There are three designs of PAM: 4-layer (4L) PAM, 2-layer low-e (2L) PAM, and 1-layer low-e (1L) PAM. 4L PAM is formed by 4 liquid charged polyethylene terephthalate (PET) films, with 1 set of frame. 2L PAM consists of 1 outer low-e film and 1 middle surface treated PET film, separated by one set of frame. 1L PAM consists of 1 low-e film, with 1 set of frame.

We consider all the major operations involved in the PAM processing, including film treatment, sectioning, packaging and handling, and assembling and installation.

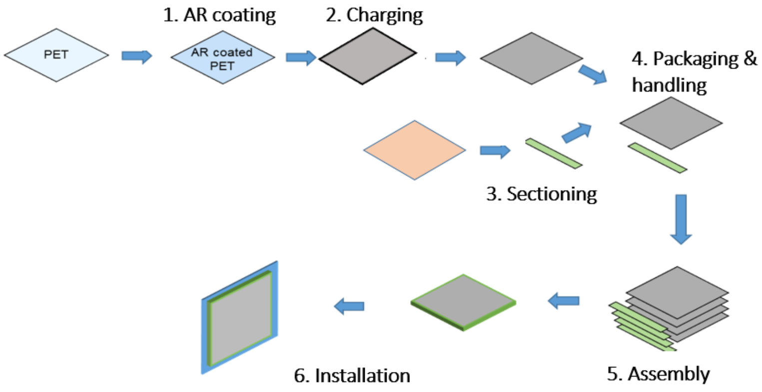

Figure 1.3 The processing procedure of 4-layer PET PAM.

1.5.2 4-Layer PET PAM

Figure 1.3 shows the processing procedure of 4-layer PET (4P) PAM, which includes: 1) Anti-reflection (AR) coating on PET films, 2) liquid charging on AR-coated

PET films, 3) sectioning of films and frame, 4) packaging and handling, 5) assembly, and 6) installation of PAM on window pane.

1.5.2.1 Materials cost

For a 1-ft^2 4-layer PET (4P) PAM, 4 ft^2 PET film and 16 ft frame bars are needed. The width of frame bar is set to 1/4”. Table 1.1 lists the materials costs.

The frame can be made of PET, polycarbonate (PC), nylon, high-density polyethylene (HDPE), etc. To be conservative, we assume that the unit cost of frame material is the same as that of the high-end PET film.

Table 1.1 Materials cost of film and frame

Material	Unit Cost ($/ft^2)	Cost for 4L PAM($/ft^2)	References
PET film	0.22	**0.88**	[40]
Frame bar	0.22	**0.08**	[40]

Table 1.2 Cost of coating materials

Material	Unit cost	Needed mass (g/ft^2)	Waste material*	PAM Cost ($\$/ft^2$)	Ref.
Sodium Formate	$100/kg	0.1	50%	0.02	[41]
AR Coating: PMMA in anisole (solvent)	$202/kg	0.1	50%	0.04	[42]

[*] It is assumed that 50% of coating materials are wasted.

Table 1.3 Equipment cost for AR coating and Liquid Charging and Sectioning

	Equipment	Cost ($)	Installation, upfit, MRO*	PAM cost** ($\$/ft^2$)	Ref.
AR dip coating	Dip coater	$100,000	2.2	0.02	[43]
Dip charging	Dip coater	$100,000	2.2	0.02	[43]
Sectioning	Cutter	$22,000	2.2	0.01	[44]

[*] Annual machinery maintenance, repair, and operation (MRO) cost is the same as the depreciation. Cost of machine installation and associated building upfit is taken as 20% of equipment cost.

[**] Assume 10-year linear depreciation.

Table 1.4 Labor cost for AR coating and Liquid Charging and Sectioning

	Work Hours (h/yr)	Hourly Labor cost ($/h)	PAM Cost ($/ft^2)
PAM Manufacturing			
1. AR dip coater	2,000	26	0.05
2. Charging dip coater	2,000	26	0.05
3. Cutter	2,000	26	0.05
Assembly and Installation	90,000	26	2.34

Table 1.5 Other cost

Costs	Amount ($)	PAM Cost ($/ft^2)	References
Packaging/handling		0.05	[45]
Rent (4,000 ft^2)	45,000/yr	0.045	[46]
Waste Management	12,000/yr	0.01	[47]

1.5.2.2 AR coating and Liquid Charging

AR coating is conducted with anisole solution of PMMA, with the unit cost of ~202 $/kg [6]. The major materials cost of AR coating comes from the solvent (anisole); it is a cost-efficient solvent commonly used in the industry. Liquid charging is conducted with 1 mM Sodium Formate aqueous solution.

The materials costs associated with AR and liquid charging are summarized in Table 1.2. In the coating process, we assume that 50% of the coating materials (active materials and solvents) would be wasted and cannot be recycled.

Both AR and liquid charging will be performed through dip coating. Table 1.3 lists the needed equipment: one dip coater dedicated to AR coating and another dip coater dedicated to liquid charging. The two dip coaters can be the same. A mid-sized dip coater costs ~\$100,000 [47]. Dip coaters are for continuous mass production, with the capacity well exceeding the required 1 million ft^2 per year.

Linear depreciation in 10 years is assumed. Annual machinery maintenance, repair, and operation (MRO) cost is assumed to be the same as the depreciation. The operation cost includes electricity cost. In addition, we assume that the cost of machine installation and building upfit takes 20% of the equipment cost. One cutter is needed for sectioning of the coated PET films and frames. A mid-sized cutter costs ~\$22,000 [47]. Table 1.3 summarizes the equipment related costs.

1.5.2.3 Labor cost of PAM processing

For each dip coater and cutter, 1 dedicated worker will be employed. This is a conservative assumption, since in reality one experienced worker may handle multiple similar machines, e.g. two dip coaters. It is assumed that there are 250 workdays per year and 8 working hours per day. The hourly labor cost is taken as \$26/hour [48].

In general, dip coating is a fast and cost-efficient mass manufacturing method commonly used in the plastics industry. Table 1.4 summarizes the labor costs associated with AR coating, liquid charging, and film/frame sectioning.

1.5.2.4 Packaging/handling, rent, and waste management

Other costs associated with PAM processing include costs of packaging/handling, rent, and waste management, summarized in Table 1.5. Packaging and handling cost of mass-produced window films is less than 0.05 $\$/ft^2$ [48]. Rent and waste management costs are assessed through market research.

1.5.2.5 Assembling and installation of PAM

We assume that assembling and installation of each set of PAM take 3 hours. Because the average sales in a local area is ~30,000 sets/year [48], the total work hours per year would be 90,000 hours (Table 1.4). Labor cost dominates the assembling and installation costs. Miscellaneous items, such as tools and equipment, are ignored.

Table 1.6 Total cost of installed 4L PAM

	Cost ($/ft^2)
Materials	0.96
AR coating	0.04
Liquid charging	0.02
Sectioning	0.01
Packaging/handling	0.05
Other	0.06
Assembly/installation	2.34
Total 4L PAM Cost (installed)	3.48

1.5.2.6 Total cost of installed PAM

Table 1.6 summarizes the estimated total cost of installed PAM. Materials cost includes the costs of polymer films and frame bars. AR coating and liquid charging costs account for the associated materials cost, equipment and maintenance/repair/operation cost, and labor cost. Other cost accounts for rent and waste management.

1.5.3 2-Layer Low-e PAM

A 2-layer low-e (2L) PAM consists of 1 layer of low-e film and 1 layer of surface-treated PET film, and 1 set of frame. The PET film of 2L PAM is the same as that of 4L PAM. The film cost is 1/4 of that of 4P PAM ($0.22 per ft^2 PAM).

Table 1.7 Total cost of installed 2L PAM

	Cost ($/ft^2)
Low-e film	3
PET film	0.22
AR coating and charging	0.14
Frame	0.08
Sectioning	0.01
Packaging/handling	0.05
Other	0.06
Assembly/installation	1.67
Total 2L PAM Cost (installed)	5.23

AR coating and charging procedures of 2L PAM are similar to those of 4L PAM, with the total film surface area much reduced. In Table 1.7, the cost of AR coating and charging of 2L PAM is taken as 1/2 of that of 4L PAM.

The frame bars of 2L PAM can be extruded, made from PC, PET, nylon, HDPE, or polyvinyl chloride (PVC). Its cross-section can be U-shaped or L-shaped, with a total thickness of ~3 mm and the width of 1/4". For a 1 ft^2 2L PAM, 4 ft such frame bars are needed. The typical manufacturing cost of extruded plastic bars is quite low. To be conservative, we assume that the frame bar cost of 2L PAM is the same as that of 4L PAM (0.08 $\$/ft^2$).

A major cost item of 2L PAM is the low-e film cost. Retail price of 3M CC75 low-e film is $\$12/ft^2$ [49]. The manufacturing cost of low-e film is usually less than 25% of the retail price. Thus, our assessment of low-e film cost is $\$3/ft^2$.

The costs associated with sectioning, packaging/handling, rent, and waste management are assumed to be the same as those of 4L PAM. Assembly/installation cost of 2L PAM is assumed to be 1/2 of that of 4L PAM, as the layer count is reduced.

The total cost of 2L PAM is summarized in Table 1.7, wherein other accounts for rent and waste management. The assessed total cost of installed 2L PAM is about $\$5.23/ft^2$. There are a few cost items that may be improved.

Table 1.8 Total cost of installed 1L PAM

	Cost ($/ft^2)
Low-e film	3
Frame	0.08
Sectioning	0.01
Packaging/handling	0.05
Other	0.06
Assembly/installation	0.78
Total 1L PAM Cost (installed)	3.98

1.5.4 1-Layer Low-e PAM

A 1-layer low-e (1L) PAM consists of 1 low-e film and frame bars. The frame of 1L PAM is similar to that of 2L PAM, except that the cross-section can be simpler (square or rectangle). To be conservative, we assume that the frame cost of 1L PAM is the same as that of 4L PAM (0.08 $/ft^2). The cost of low-e film is the same as that of 2L PAM.

The cost of sectioning is ~1/2 of that of 4P PAM, since the use of materials is less. The costs associated with packaging/handling, rent, and waste management are assumed to be the same as those of 4P PAM. Assembly/installation cost of 1L PAM is assumed to be 1/3 of that of 4L PAM, since there is only 1 layer in 1L PAM.

The total cost of 1L PAM is summarized in Table 1.8, wherein other includes the costs of rent and waste management.

1.6 Structure of the thesis

In Chapter 2 and part of Chapter 3, the mechanism of liquid flow electrification and corona charging were studied. The electrified polymer films were utilized to form polymer-air-multilayer (PAM) structure. The thermal, optical, and structural performance of PAM were investigated in Chapter 3. In chapter 4, to improve radiative heat resistance of PAM, the low-emissivity coating and layer count effects on PAM have been investigated. In Chapter 5, the effect of elevating one-layer of low-emissivity film from window has been studied. In Chapter 6, anti-reflection coating on PAM structure has been investigated to further improve its optical properties.

References

[1] U.S. DOE, Windows and Building Envelope Research and Development: Roadmap for Emerging Technologies, US Dep. Energy, Build. Technol. Off. Washington, DC. (2014).

[2] US Department of Energy, Research and Development Roadmap for Emerging HVAC Technologies, US Dep. Energy, Build. Technol. Off. Washington, DC. (2014) 121.

[3] A. Afram, F. Janabi-Sharifi, Theory and applications of HVAC control systems–A review of model predictive control (MPC), Build. Environ. 72 (2014) 343–355.

[4] N. Lu, An evaluation of the HVAC load potential for providing load balancing service, IEEE Trans. Smart Grid. 3 (2012) 1263–1270.

[5] D. Arasteh, E. Finlayson, J. Huang, C. Huizenga, R. Mitchell, M. Rubin, State-of-the-art software for window energy-efficiency rating and labeling, Lawrence Berkeley National Lab., CA (US), 1998.

[6] B.I. Abonyi, J. Tang, C.G. Edwards, Evaluation of energy efficiency and quality retention for the Refractance Window (drying system, Res. Rep. (1999).

[7] Single -Pane Highly Insulating Efficient Lucid Designs (SHIELD) Program Overview, (2014) 1–13.

[8] U.S. DoE, Buildings energy databook, Energy Effic. Renew. Energy Dep. (2011).

[9] How Much Does Window Replacement Cost? | Angie's List, (2015).

[10] F. Horowitz, M.B. Pereira, G.B. de Azambuja, Glass window coatings for sunlight heat reflection and co-utilization, Appl. Opt. 50 (2011) C250–C252.

[11] J. Carmody, S. Selkowitz, E. Lee, D. Arasteh, T. Willmert, Window System for High-Performance Buildings, (2004).

[12] Single -Pan Highly Insulating Efficient Lucid Designs (SHIELD) Program Overview, (2014) 1–13.

[13] T.L. Bergman, F.P. Incropera, D.P. DeWitt, A.S. Lavine, Fundamentals of heat and mass transfer, John Wiley & Sons, 2011.

[14] F.P. Incropera, A.S. Lavine, T.L. Bergman, D.P. DeWitt, Fundamentals of heat and

mass transfer, Wiley, 2007.

[15] J.L. Wright, A correlation to quantify convective heat transfer between vertical window glazings, ASHRAE Trans. 102 (1996).

[16] C. Schaefer, G. Bräuer, J. Szczyrbowski, Low emissivity coatings on architectural glass, Surf. Coatings Technol. 93 (1997) 37–45.

[17] J.R. Howell, M.P. Menguc, R. Siegel, Thermal radiation heat transfer, CRC press, 2015.

[18] J. Apte, D. Arasteh, Window-related energy consumption in the US residential and commercial building stock, (2008).

[19] D.W. Dockery, J.D. Spengler, Indoor-outdoor relationships of respirable sulfates and particles, Atmos. Environ. 15 (1981) 335–343.

[20] C. Turrell, Storm Windows Save Energy, HOME ENERGY. 17 (2000) 20–23.

[21] J.H. Klems, Measured winter performance of storm windows, Lawrence Berkeley National Lab.(LBNL), Berkeley, CA (United States), 2002.

[22] T.D. Culp, S.H. Widder, K.A. Cort, Thermal and Optical Properties of Low-E Storm Windows and Panels, Pacific Northwest National Lab.(PNNL), Richland, WA (United States), 2015.

[23] R.J. Martın-Palma, L. Vazquez, J.M. Martınez-Duart, Silver-based low-emissivity coatings for architectural windows: Optical and structural properties, Sol. Energy Mater. Sol. Cells. 53 (1998) 55–66.

[24] J. Fricke, W.L. Borst, Essentials of energy technology: sources, transport, storage, conservation, John Wiley & Sons, 2013.

[25] J. Szczyrbowski, A. Dietrich, K. Hartig, Bendable silver-based low emissivity coating on glass, Sol. Energy Mater. 19 (1989) 43–53.

[26] J. Szanyi, The origin of haze in CVD tin oxide thin films, Appl. Surf. Sci. 185 (2002) 161–171.

[27] 2 SHIELD Program Overview. doi:10.1016/j.rmed.2008.09.011.

[28] T. Gao, B.P. Jelle, T. Ihara, A. Gustavsen, Insulating glazing units with silica aerogel granules: The impact of particle size, Appl. Energy. 128 (2014) 27–34.

[29] U. Berardi, The development of a monolithic aerogel glazed window for an energy retrofitting project, Appl. Energy. 154 (2015) 603–615.

[30] Y.-L. He, T. Xie, Advances of thermal conductivity models of nanoscale silica aerogel insulation material, Appl. Therm. Eng. 81 (2015) 28–50.

[31] H. Maleki, L. Durães, A. Portugal, An overview on silica aerogels synthesis and different mechanical reinforcing strategies, J. Non. Cryst. Solids. 385 (2014) 55–74.

[32] R.P. Patel, N.S. Purohit, A.M. Suthar, An overview of silica aerogels, Int. J. ChemTech Res. 1 (2009) 1052–1057.

[33] M. Reim, W. Körner, J. Manara, S. Korder, M. Arduini-Schuster, H.-P. Ebert, J. Fricke, Silica aerogel granulate material for thermal insulation and daylighting, Sol. Energy. 79 (2005) 131–139.

[34] M. Schwan, M. Rößler, B. Milow, L. Ratke, From fragile to resilient insulation: synthesis and characterization of aramid-honeycomb reinforced silica aerogel composite materials, Gels. 2 (2016) 1.

[35] R. Baetens, B.P. Jelle, A. Gustavsen, Aerogel insulation for building applications: a state-of-the-art review, Energy Build. 43 (2011) 761–769.

[36] X.-D. Wang, D. Sun, Y.-Y. Duan, Z.-J. Hu, Radiative characteristics of opacifier-loaded silica aerogel composites, J. Non. Cryst. Solids. 375 (2013) 31–39.

[37] Y. Zhong, R. Kou, M. Wang, Y. Qiao, Synthesis of centimeter-scale monolithic SiC nanofoams and pore size effect on mechanical properties, J. Eur. Ceram. Soc. 39 (2019) 2566–2573.

[38] Standard Window Size, Retrieved from Https//Modernize.Com/Windows/Standard-Sizes. (n.d.).

[39] Gorence N (2016), Techno-economic analysis (TEA) for ARPA-E SHIELD Performers..

[40] Blanchet G (2017). Email communication: "…quote by Dupont for a super clear heat stabilized film ST504 in moderate volume from large master roll is about 0.22 $/ft2." According to our previous market research, factory prices of mid- to high-end PET films .

[41] https://www.scbt.com/p/sodium-formate-141-53-7?lang=en&cur=usd&gclid=CjwKCAiA3abwBRBqEiwAKwICA1uH6c3RianXFUZZajpMx3T5rayUEL1g2-evAnJtzPP-OFG4HRc3PxoCtA0QAvD_BwE.

[42] https://www.net32.com/vendor/17396.

[43] https://www.alibaba.com/product-detail/dip-coating-

machine_60208665602.html?spm=a2700.7724838.2017115.8.4a82e310WNL7SC&s=p.

[44] https://www.alibaba.com/product-detail/Auto-window-film-Cutting-Machine_60369278984.html?spm=a2700.7724838.0.0.xk4HIv&s=p.

[45] Richard Chen from Rightint (2017). Private conversations..

[46] http://www.us.jll.com/united-states/en-us/news/4302/long-island-industrial-rents-surpass-11-per-square-foot.

[47] https://www.wm.com/location/california/ventura-county/_documents/SVLRC_2013_Rate_Schedule.pdf.

[48] https://www.bls.gov/news.release/empsit.t19.htm.

[49] Dr. Raghu Padiyath, Division Scientist, Commercial Solutions Division, 3M (2017). Private conversations.

Chapter 2 Flow Electrification of Polycarbonate and Polyethylene Terephthalate

2.1 Introduction

It is well known that when a liquid, e.g. an aqueous solution of electrolyte, flows across a polymer surface, the polymer can be electrified [1–6], owning to the charge separation at solid-liquid interface [7] and the charge accumulation [8–10]. Uncontrolled surface charges could be harmful in many circumstances for petroleum industry, electrical systems, and electronic devices [11,12]. Controlled surface charges can be beneficial and have wide applications for biosensors and bioactuators, electronics, drug delivery, energy harvesting, etc. [13–18], especially for our electret structures. We envision that if multiple polymer layers are like charged, they would repel each other, helping stabilize a hollow solid-air multilayer configuration. The small air gaps block conductive heat transfer and suppress air convection, and the polymer layers reduce radiative heat transfer. Because the polymer-air interfaces are large and flat, they cause little light scatter.

When a polymer is exposed to an electrolyte solution, ionization and/or dissociation of surface groups (e.g. dissociation of proton from carboxylic group) would render the solid phase negatively charged and form a positively charged electrical double layer (EDL) [7,19]. Since the force fields across the solid-liquid interface are asymmetric, the ion distribution is anisotropic. In the close proximity to the solid surface, there is a Stern layer, wherein counter-ions are adsorbed or specifically adsorbed. Farther away from the solid surface, there is a diffuse layer, which extends into the bulk liquid phase, as depicted in Figure 2.1(a). Within the shear plane in the diffuse layer, the solid may be viewed as a single entity [7,20]. When a liquid flow removes a portion of counter-ions beyond the shear plane, it will break the static equilibrium of the EDL and induce a surface potential [7,21], as illustrated in Figure 2.1(b). Currently, many details of the flow electrification are still under investigation [22–24]. One of the critical factors that has not been fully understood is the ion size.

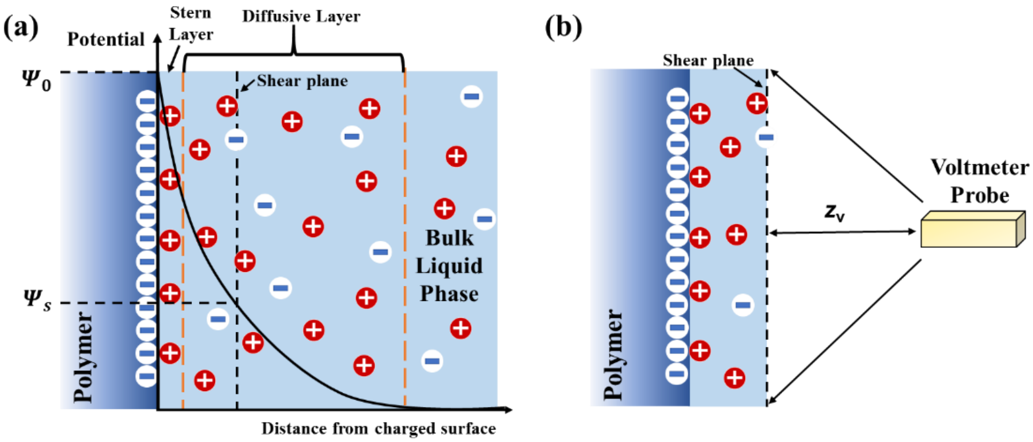

Figure 2.1 (a) A charged polymer surface exposed to an aqueous electrolyte solution. (b) Residual surface charges after liquid flows across the polymer surface; a voltmeter can be employed to measure the surface potential.

2.2 Experimental

Flow electrification experiment was carried out on a set of aqueous solutions of sodium salts. The polymer was either polycarbonate (PC) or polyethylene terephthalate (PET) film about 125- μm thick, obtained from McMaster-Carr (Product No. 85585K102 and 8567K52). The solutions were prepared by ultrasonically dissolving salts in de-ionized (DI) water for 5 min. The molarity was 3 mM. Table 2.1 lists the sodium salts under investigation: sodium formate (SF), sodium acetate (SA), sodium propionate (SP), sodium butyrate (SB), sodium hexanoate (SH), sodium octanoate (SO), sodium decanoate (SD), and sodium stearate (SS). The cation was always sodium. The anions had similar functional groups but various carbon chain lengths, increasing from SF to SS. We also tested sodium dodecanoate (SDD) and sodium dodecyl (SDS), which have different functional groups from the other salts.

PC or PET films were cut into 38×38 mm squares, and ultrasonically cleaned first in isopropyl alcohol (IPA) for 10 min and then in DI water for 5 min, followed by vacuum drying at 60°C for 24 hr. One side of the PC or PET film was attached to the loading grip of a type-5582 Instron machine by duct tapes. As shown in Figure 2.2(a), the film was lowered into a container containing an electrolyte solution and immediately pulled out at a constant rate of 4 mm/sec. For SF, SB and SO, additional electrification was conducted with various salt concentrations from 0.1 mM to 100 mM. For PC film with 1 mM SF solution, the lifting rate was varied in the range from 0.01 to 8 mm/sec. Surface potential (V) was measured by a Trek Model-344 voltmeter, with the probe distance z_{volt} =25 mm (Figure 2.1(b)). The capacitive probe allows for non-contact and non-destructive evaluation of V. All the tests were performed in ambient air at ~23 ^{o}C, with the relative humidity of ~60%.

Table 2.1 List of electrolytes under investigation

Electrolyte	Abbreviation	Molecular formula	Chain length (Number of C-C bonds in anion)	Sigma-Aldrich Product No.
Sodium Formate	SF	HCOONa	0	71539
Sodium Acetate	SA	CH_3COONa	1	W302406
Sodium propionate	SP	$CH_3(CH_2)COONa$	2	P1880
Sodium butyrate	SB	$CH_3(CH_2)_2COONa$	3	B5887
Sodium hexanoate	SH	$CH_3(CH_2)_4COONa$	5	C4026
Sodium octanoate	SO	$CH_3(CH_2)_6COONa$	7	C5038
Sodium decanoate	SD	$CH_3(CH_2)_8COONa$	9	C4151
Sodium dodecanoate	SDD	$CH_3(CH_2)_{10}COONa$	11	L9755
Sodium Stearate	SS	$CH_3(CH_2)_{16}COONa$	17	S3381
Sodium dodecyl sulfate	SDS	$CH_3(CH_2)_{11}SO4Na$	11	436143

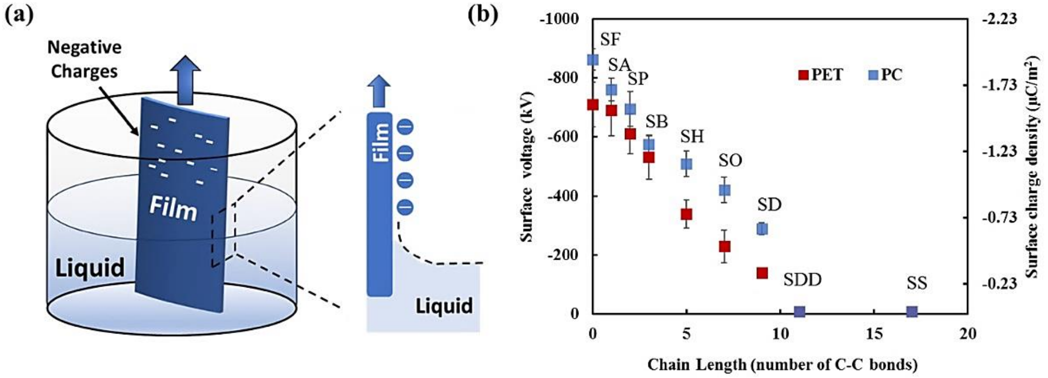

Figure 2.2 (a) Schematic of the experimental setup. (b) The surface potential and the residual surface charge density as functions of the anion size.

2.3 Results and Discussion

Figure 2.2(b) shows the surface potential of PET and PC upon flow electrification. All the samples are negatively charged. As the anion size increases from SF to SS, the magnitude of surface potential keeps decreasing. The surface potential can be calculated as $V(z) = \int_{-L/2}^{L/2}\int_{-L/2}^{L/2} \frac{\sigma_s}{4\pi\varepsilon_0\sqrt{x^2+y^2+z^2}}\,\mathrm{d}x\,\mathrm{d}y$, where σ_s is the average surface charge density, L is the polymer sample size, ε_0 is the air permittivity, x and y are the in-plane dimensions, and z is the distance to film surface [25]. Solving this integral equation gives

$$\sigma_s = -2\pi\varepsilon_0 V\left\{2z_{\text{volt}} \times \text{ArcTan}\left(\frac{L^2}{4z_{\text{volt}}\sqrt{\frac{L^2}{2}+z_{\text{volt}}^2}}\right) + L\left[\ln\left(-\frac{L}{2}+\sqrt{\frac{L^2}{2}+z_{\text{volt}}^2}\right) - \ln\left(\frac{L}{2}+\sqrt{\frac{L^2}{2}+z_{\text{volt}}^2}\right)\right]\right\}^{-1} \tag{2.1}$$

In the classic Gouy-Chapman model, with the Debye-Huckel approximation [7,19], the ions in the diffuse layer lead to an exponential potential decay along the z-direction:

$$\psi = \psi_0 e^{-\kappa z} \tag{2.2}$$

where ψ_0 is the electric potential at the polymer surface, $\kappa^2 = [(e^2/\varepsilon k_B T) \sum_i z_i{}^2 n_{i\infty}]$, $n_{i\infty} = 1000 M_i N_A$ is the number of ions of type i per unit volume, z_i is the ion charge, k_B is the Boltzmann constant, T is temperature, e is the electron charge, and ε is the liquid permittivity. Based on the Poisson equation, the relationship between the potential and the charge density (ρ) is:

$$\frac{\partial^2 \psi}{\partial^2 z} = -\frac{\rho}{\varepsilon}. \tag{2.3}$$

Combination of Eqs. (2.2) and (2.3) results in

$$\rho = -\psi_0 \kappa^2 \varepsilon e^{-\kappa z} \tag{2.4}$$

The excess charges in the liquid phase must be balanced by the charges at polymer surface (σ_0); that is

$$\int_0^\infty \rho \, \mathrm{d}z + \sigma_0 = 0. \tag{2.5}$$

In accordance with Eq. (2.4) and (2.5),

$$\sigma_0 = \psi_0 k \varepsilon \tag{2.6}$$

As the liquid flows, the boundary layer adheres to the polymer surface. Along the shear plane, the relative velocity is zero [26]. The shear plane location (z_s) is beyond the Stern layer. Upon liquid-polymer separation, the excess charges within the non-slip region ($\int_0^{z_s} \rho \cdot \mathrm{d}z$) stay with the polymer. Consequently,

$$\sigma_s = \int_0^{z_s} \rho \cdot \mathrm{d}z + \sigma_0 = \sigma_0 e^{-z_s \sqrt{(e^2/\varepsilon k_B T) \sum_i z_i^2 n_{i\infty}}} \; . \tag{2.7}$$

From Eq. (2.7), it can be seen that the residual surface charge density depends on z_s, $n_{i\infty}$, and σ_0. Figure 2.3(a) shows the ratio of residual surface charge density (σ_s) over the solid-surface charge density σ_0 for 1:1 electrolyte. Clearly, σ_s (and also the magnitude of surface voltage, V) increases with a lower electrolyte concentration or a closer shear plane. Figure 2.3(b) and (c) compares the experimental data of SF, SB, SO and SDD electrified polymer samples. The trend can be captured by Eq. (2.7) quite well. To best fit the data, σ_0 should be set to 3.03, 3.07, 3.00, and 2.95 μC/m^2, respectively, for the four salts. The difference is within the data scatter. That is, the anion size has little influence on the solid-surface charge density, which implies that compared with the anion charge, the anion size is only a secondary factor of the dissociation of polymer surface groups.

The correlation between σ_s and the anion size is mainly related to the shear plane position. For SF, SB, SO and SDD, z_s are 2.44 nm, 5.32 nm, 6.56 nm and 41.1 nm, respectively. As the ion size rises, the effective liquid viscosity becomes larger [27]. Thus, the boundary layer is thicker, so that more excess charges remain on the polymer surface in the adhered liquid film, which counterbalances σ_0 and reduces the overall surface charge density. The variation in z_s may also be influenced by the polymer-liquid interface tension (γ). As larger ions tend to be adsorbed by the polymer, γ would be reduced. Figure 2.4 shows the contact angle measurement results by using a Ramé-hart Model-200 Contact Angle Goniometer. The measurement was performed on droplets of 100 mM electrolyte solutions on a flat surface of PC or PET. The testing data confirm that γ is lower when the electrolyte has a larger anion size; that is, larger ions tend to be adsorbed, so that the shear plane is farther away from the solid surface.

The contact angle of 10 mM Sodium dodecyl sulfate (SDS) with PC is 37.8°, less than that of SDD, 67.5°. As illustrated in Figure 2.3(c), with sulfate radical instead of carboxyl group, although SDS has a similar chain length with SDD, its residual surface charge density is less, due to the low interface tension (γ).

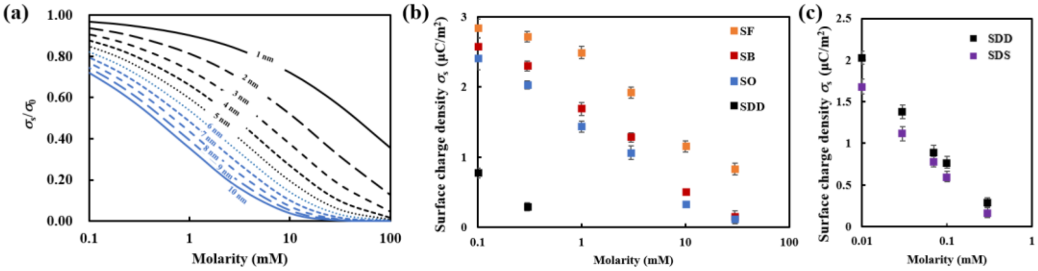

Figure 2.3 a) The ratio of the residual surface charge density (σ_s) to the solid-surface charge density (σ_0) as a function of the electrolyte concentration; the numbers on the curves indicate the shear plane distance to the polymer surface (z_S). b) and c) The experimental data of residual surface charge density of SF, SB, SO, SDD, and SDS, compared with Eq. (2.7).

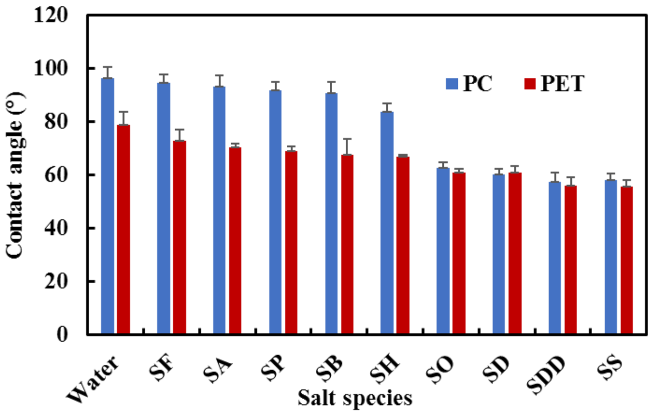

Figure 2.4 The contact angle measurement results

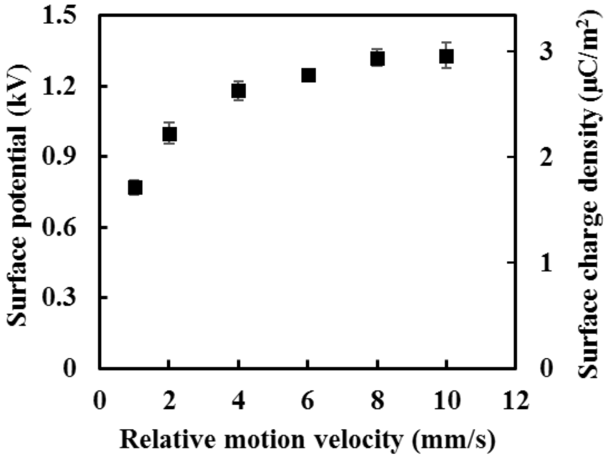

Figure 2.5 The flow rate effect on the surface voltage. In all the tests, 1 mM aqueous solution of SF flows across PC film surface.

We also analyzed the effect of flow rate (*v*), as shown in Figure 2.5. When the film is taken out of the liquid faster, the residual surface charge density is increased, and eventually converges to about 3 μC/m^2. It is interesting that when *v* is small, the surface charge is nearly zero; i.e., mere exposure of polymer to electrolyte solution would not cause surface electrification. The liquid velocity profile plays a critical role. This is consistent with the literature data [28,29], as well as Eq.(2.7). The charge separation depends on the relative motion between the liquid phase and the polymer surface. The effective shear plane distance (z_s) is infinitely large if $v = 0$, and is small when v is large. Therefore, the residual surface charge density and the surface voltage are negatively correlated to the flow rate.

2.4 Conclusion

We performed flow electrification experiment on PC and PET films with dilute aqueous solutions of a variety of sodium salts. The testing data suggest that the surface voltage and the residual surface charge density would be higher if the ion size or the ion concentration decreases, or the liquid flows faster. An equation (Eq.2.7) is derived based on the classic Gouy-Chapman model, which takes into account the solid-surface charge density and the shear plane distance. Comparison of the numerical result and the experimental data suggests that for the salts with the same functional group, the ion size has little influence on the solid-surface charge density; i.e. the dissociation processes of surface groups of all the electrolytes are similar. The key factor is the shear plane distance, which is dependent on the liquid viscosity, the solid-liquid interface tension, as well as the flow rate.

Acknowledge

Chapter 2, in part, is a reprint of the material as it appears in Applied Physics Letter. Rui Kou, Ying Zhong and Yu Qiao. Effects of anion size on flow electrification of polycarbonate and polyethylene terephthalate. 115(7), p.073704. The dissertation author was the primary investigator and first author of the paper.

References

[1] S.S. Dukhin, B.V. Deriaguine, Surface and Colloid Science: Electrokinetic Phenomena: Translated from the Russian by A. Mistetsky and M. Zimmerman, Plenum Press, 1974.

[2] H.F. Richards, The contact electricity of solid dielectrics, Phys. Rev. 22 (1923) 122.

[3] B.A. Kwetkus, Particle triboelectrification and its use in the electrostatic separation process, Part. Sci. Technol. 16 (1998) 55–68.

[4] G. Touchard, Flow electrification of liquids, J. Electrostat. 51 (2001) 440–447.

[5] D.J. Montgomery, Static electrification of solids, in: Solid State Phys., Elsevier, 1959: pp. 139–197.

[6] Y. Qiao, A. Han, V.K. Punyamurtula, Electrification of a nanoporous electrode in a continuous flow, J. Phys. D. Appl. Phys. 41 (2008) 85505.

[7] P.C. Hiemenz, R. Rajagopalan, Principles of Colloid and Surface Chemistry, revised and expanded, CRC press, 1997.

[8] A.L. Sumner, E.J. Menke, Y. Dubowski, J.T. Newberg, R.M. Penner, J.C. Hemminger, L.M. Wingen, T. Brauers, B.J. Finlayson-Pitts, The nature of water on surfaces of laboratory systems and implications for heterogeneous chemistry in the troposphere, Phys. Chem. Chem. Phys. 6 (2004) 604–613.

[9] Z. Lin, G. Cheng, L. Lin, S. Lee, Z.L. Wang, Water–Solid Surface Contact Electrification and its Use for Harvesting Liquid-Wave Energy, Angew. Chemie. 125 (2013) 12777–12781.

[10] Y. Awakuni, J.H. Calderwood, Water vapour adsorption and surface conductivity in solids, J. Phys. D. Appl. Phys. 5 (1972) 1038.

[11] K. Yatsuzuka, Y. Higashiyama, K. Asano, Electrification of polymer surface caused by sliding ultrapure water, IEEE Trans. Ind. Appl. 32 (1996) 825–831.

[12] W.D. Rees, Static hazards during the top loading of road tankers with highly insulating liquids: flow rate limitation proposals to minimize risk, J. Electrostat. 11 (1981) 13–25.

[13] M.C. Wiles, T. VanderNoot, D.J. Schiffrin, Electrosorption of amphiphilic affinity

dyes at liquid/liquid interfaces for biosensor applications, J. Electroanal. Chem. Interfacial Electrochem. 281 (1990) 231–244.

[14] D.-R. Chen, C.H. Wendt, D.Y.H. Pui, A novel approach for introducing bio-materials into cells, J. Nanoparticle Res. 2 (2000) 133–139.

[15] B. Fan, A. Bhattacharya, P.R. Bandaru, Enhanced voltage generation through electrolyte flow on liquid-filled surfaces, Nat. Commun. 9 (2018) 4050.

[16] Z. Wang, M. Lemmon, Stability analysis of weak rural electrification microgrids with droop-controlled rotational and electronic distributed generators, in: Power Energy Soc. Gen. Meet. 2015 IEEE, IEEE, 2015: pp. 1–5.

[17] A.K. Bajpai, S.K. Shukla, S. Bhanu, S. Kankane, Responsive polymers in controlled drug delivery, Prog. Polym. Sci. 33 (2008) 1088–1118.

[18] S. Park, S. Park, R.-A. Jeong, H. Boo, J. Park, H.C. Kim, T.D. Chung, Nonenzymatic continuous glucose monitoring in human whole blood using electrified nanoporous Pt, Biosens. Bioelectron. 31 (2012) 284–291.

[19] L.H. Sperling, Introduction to physical polymer science, John Wiley & Sons, 2005.

[20] L. Joly, C. Ybert, E. Trizac, L. Bocquet, Hydrodynamics within the electric double layer on slipping surfaces, Phys. Rev. Lett. 93 (2004) 257805.

[21] S.S. Bahga, O.I. Vinogradova, M.Z. Bazant, Anisotropic electro-osmotic flow over super-hydrophobic surfaces, J. Fluid Mech. 644 (2010) 245–255.

[22] D.J. Lacks, R.M. Sankaran, Contact electrification of insulating materials, J. Phys. D. Appl. Phys. 44 (2011) 453001.

[23] M.M. Apodaca, P.J. Wesson, K.J.M. Bishop, M.A. Ratner, B.A. Grzybowski, Contact electrification between identical materials, Angew. Chemie Int. Ed. 49 (2010) 946–949.

[24] H.T. Baytekin, A.Z. Patashinski, M. Branicki, B. Baytekin, S. Soh, B.A. Grzybowski, The mosaic of surface charge in contact electrification, Science (80-.). (2011) 1201512.

[25] Y. Zhong, R. Kou, M. Wang, Y. Qiao, Electrification Mechanism of Corona Charged Organic Electrets, J. Phys. D. Appl. Phys. (2019).

[26] B.R. Munson, T.H. Okiishi, W.W. Huebsch, A.P. Rothmayer, Fluid mechanics, Wiley Singapore, 2013.

[27] R.J. Hunter, Foundations of colloid science, Oxford university press, 2001.

[28] Y. Sun, X. Huang, S. Soh, Using the gravitational energy of water to generate power by separation of charge at interfaces, Chem. Sci. 6 (2015) 3347–3353.

[29] S. Ghosh, A.K. Sood, N. Kumar, Carbon nanotube flow sensors, Science (80-.). 299 (2003) 1042–1044.

Chapter 3 Thermal Insulating Polymer-Air Multilayer

3.1 Introduction

Thermal management of buildings, particularly mitigation of heat loss ofs building windows, is of immense importance to energy efficiency and sustainability. Among all the consumed energy related to buildings in the U.S., 40% is used for building heating, ventilation, and air conditioning (HVAC), in which ~25% is lost because of the inefficient thermal insulation of windows [1]. Currently in the U.S., 30~40% of windows are still single-pane, responsible to ~50% of window thermal energy loss; in the next 40 years, hardly could they be fully replaced by more energy efficient double-pane or triple-pane insulated glass units (IGU) [2].

Low-cost, transparent, and highly thermal insulating coating materials are still lacking. Silica aerogel, for example, can have an excellent thermal conductivity (k) as low as 0.012 W/(m·K) [3,4], partly due to the high porosity > 99% and partly due to the Knudsen effect of rarified air in nanopores [5,6]. Its visual transmittance can be satisfactory, as the nanopore size is much smaller than the visual light wavelength [7,8]. However, with the structural integrity being considered, the porosity must be quite low and therefore, the ultralow thermal conductivity may not be realized. With a porosity ~50%, the thermal conductivity would be 0.04~0.1 W/(m·K), higher than that of air [7].

Moreover, haze of silica aerogel tends to be large, due to the pore size distribution [5,6,9–11].

Low-emissivity (low-e) film, for another example, blocks radiative heat transfer in the infrared (IR) range. An issue of low-e film is water condensation. Low-e film does not reduce conductive heat transfer. If its surface is in contact with a water layer, heat conduction would dominate the thermal properties [12–14]. The large decrease in visual transmittance and the change in color [15], as well as the relatively high materials and installation costs [16], are also of major concerns.

In the current research, we develop and characterize a polymer-based coating structure, referred as the polymer-air multilayer (PAM). Figure 3.1(a) shows a side view of PAM, comprising multiple transparent polymer films separated by air gaps. The polymer layer thickness ranges from less than 10 μm to more than 100 μm and the air gap thickness ranges from less than 0.1 mm to more than 1 mm. The layer separation is achieved by slightly stretching the polymer films, aided by like charges induced by corona charging and liquid electrification [17,18]. As the air gaps are thinner than 5 mm, air convection in them is negligible [19]. The air gaps have a low thermal conductivity ~0.026 W/m·K. In addition, if the polymer absorbs IR radiation from the indoor direction and equally re-emits the absorbed energy to indoor and outdoor directions, each polymer layer would block the radiation heat loss by roughly 50%. Because all the conductive, radiative, and convective heat transports are reduced, PAM should possess excellent thermal insulation properties. Its optical properties, such as visual transmittance and haze, are dominated by the transparency and flatness of the polymer layers.

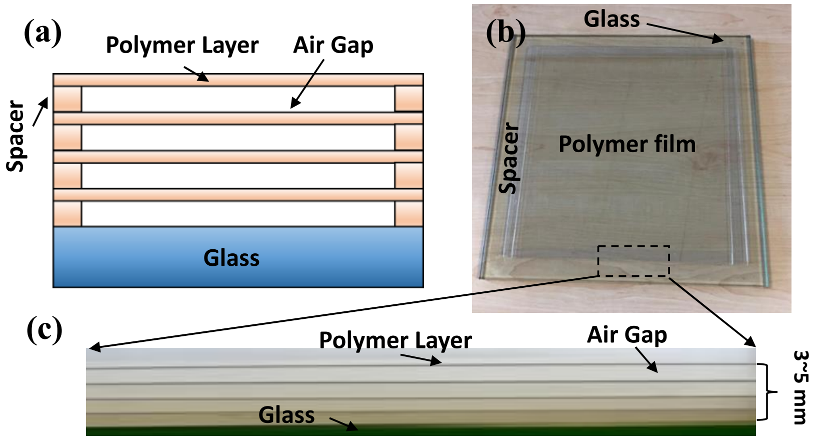

Figure 3.1 (a) A schematic of the polymer-air multilayer (PAM) structure; (b) the top view and c) the side view of a typical PAM sample.

3.2 Experimental Procedure

PAM samples were formed by 4 layers of 125-μm-thick 0.3×0.3 m electrified polyethylene terephthalate (PET) films, with 4 sets of spacers made of 0.25''-wide polycarbonate (PC) at the edges. It was mounted on a 10-mm-thick 0.3556-mm-large glass pane, as shown in Figure 3.1. The spacer thickness ranged from 500 μm to 1 mm, which determined the thickness of the air gaps. The spacers were affixed by adhesives (3M CA5) that cured at ambient temperature.

3.2.1 Polymer electrification and repulsive force measurement

Corona charging and liquid electrification were performed. PET films were ultrasonically cleaned in isopropyl alcohol (IPA) for 10 min and then in de-ionized (DI) water for 5 min, and dried in vacuum at 60 ℃ for 24 hr. Figure 3.2(a) and 3.2(b) show the corona charging setup, which follows the work of Zhong et al. [17,18]. A 0.75-inch-long 0.059-inch-diameter tungsten needle electrode and a grid mesh made of stainless steel 304 wires (with the wire diameter of 0.016 inches and the mesh size of #20) were connected to two Glassman FJ Series 120 Watt regulated high-voltage DC power supplies, with the capacities respectively being 40 kV and 20 kV. The PET film was placed on a grounded stainless-steel plate. The grid mesh was 4 mm away from the polymer surface. The distance between the needle and the grid was 4 mm. The corona polarity was kept negative; the charging time was 60 sec.

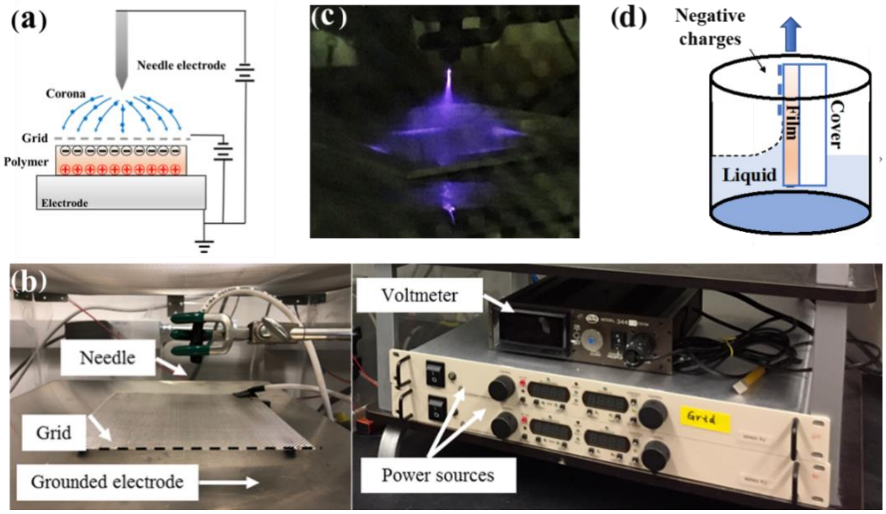

Figure 3.2 (a) Schematic and (b) a photo of the corona charging system. (c) A photo of the corona discharging process. (d) Flow electrification.

Corona charging induced a dipolar voltage distribution (V_d) along the polymer film thickness direction. After the PET film was lifted from the grounded steel plate, the positively charged side was covered by a Plastic container made of polycarbonate. The negatively charged side was dipped into an aqueous solution of sodium formate (SF) and dried in air, similar to the process presented in Chapter 2. The SF concentration (c) was 0.3, 1,3, 10, 30, or 100 mM. We also investigated the effect of the grid voltage (V_{grid}). PET films were corona-charged with various V_{grid} (-1, -1.5, -2, -2.5, or -3 kV) and then flow-electrified by 10 mM SF solution. Surface voltages were measured by a Trek Model 344 voltmeter from both sides of the treated films, with the probe distance of 25 mm. All the experiments were carried out in lab air at room temperature, with the relative humidity ~60%.

A force measurement system was developed to characterize the repulsive pressure between the charged films. It consisted of an analytical balance (Ohaus Explorer Scale-220), two polycarbonate (PC) sample-holding racks, and a glass cage. The lower rack was affixed on the balance and the upper rack was affixed on the cage ceiling. One electrified PET film was placed on the bottom rack and the scale was calibrated to zero. Then, another electrified film was attached on the upper rack, with the edges aligned with the bottom film. The repulsive pressure, P, was calculated as F/A, where F is the repulsive force and A is the film area. In our measurement, the gap between the two polymer film samples, d, was in the range from 2 mm to 8 mm.

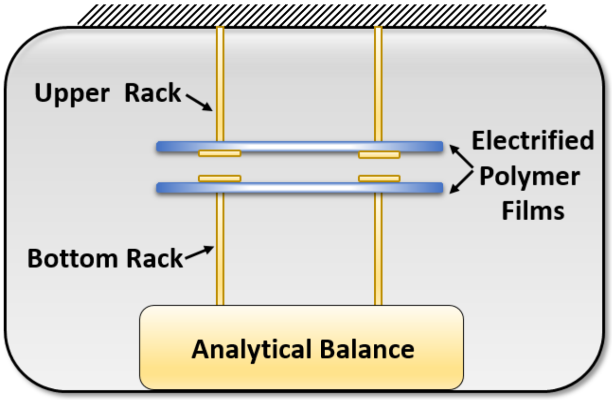

Figure 3.3 Schematic of the force measuring system

3.2.2 Thermal transmittance (*U*-factor) measurement

The rate of heat loss through windows can be characterized by the *U*-factor. Figure 3.4 shows the *U*-factore measurement system, which follows ASTM C1199, ASTM C518, NFRC-100, and NFRC-102. The system was developed by Jeongmin Kim in Professor Renkun Chen's lab at the University of California, San Diego. Inside of a 0.39-m-long 0.47-m-wide 0.47-m-tall environmental chamber, the temperature (T_{ext}) was maintained at about -18 ℃. Outside of the chamber, the lab ambient temperature (T_{in}) was ~21℃. A PAM sample was mounted on the 0.37×0.37 m large glass window in the chamber wall. To monitor the heat flux, a gSKIN XI heat flux sensor was attached to the outer surface of the PAM sample. T_{ext} and T_{in}, as well as the temperatures at the innermost surface and the outermost surface of PAM ($T_{\mathrm{PAM,in}}$ and $T_{\mathrm{PAM,ext}}$) were monitored by four Omega type-K thermocouples, respectively. According to ASTM

C1199 and NFRC-100, the standard boundary heat transfer coefficients to the exterior side ($h_{\mathrm{ST,ext}}$) was set to 30 W/($\mathrm{m^2 \cdot K}$), and the interior side coefficient ($h_{\mathrm{ST,in}}$) is

$$h_{\mathrm{ST,in}} = 1.46\left[\frac{\left(T_{\mathrm{in}} - T_{\mathrm{PAM,in}}\right)}{H}\right]^{0.25} + \sigma\varepsilon\left[\frac{(T_{\mathrm{in}} + 273.16)^4 - \left(T_{\mathrm{PAM,in}} + 273.16\right)^4}{\left(T_{\mathrm{in}} - T_{\mathrm{PAM,in}}\right)}\right] \tag{3.1}$$

where H is the sample height, $\sigma = 5.67 \times 10^{-8}\ \mathrm{W/m^2 \cdot K^4}$ is the Stefan Boltzmann constant, and ε represents the surface emissivity of the innermost surface of polymer film. The thermal transmittance (U-factor) evaluates the rate of heat transfer under steady-state condition per unit area and per unit temperature difference. It is equal to the reciprocal of the total thermal resistance,

$$U = \left(\frac{1}{h_{\mathrm{ST,ext}}} + \frac{T_{\mathrm{PAM,in}} - T_{\mathrm{PAM,ext}}}{q} + \frac{1}{h_{\mathrm{ST,in}}}\right)^{-1} \tag{3.2}$$

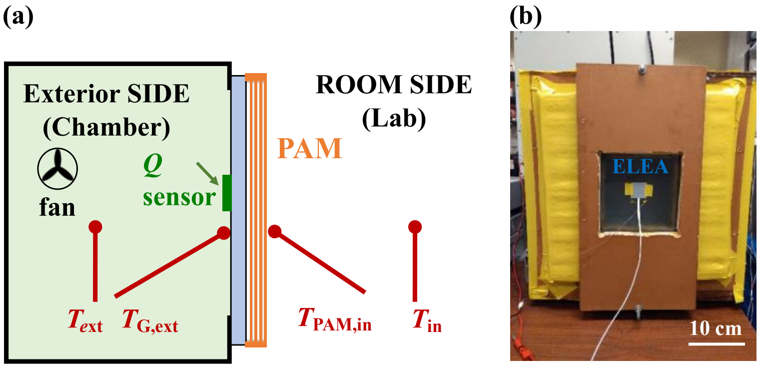

Figure 3.4 (a) Schematic and (b) a photo of the thermal transmittance (U-factor) measurement setup.

3.2.3 Measurement of optical properties

Visual transmittance measurement was conducted for the spectral range from 380 nm to 780 nm, using a JASCO V770 UV-VIS spectrometer, following ASTM D1003. A UV-Vis spectrophotometer was employed as the light source. The PAM sample was placed in front of the entrance port of the integrating sphere, in which the visible light could be collected by a photo detector. The visible light transmittance (V_T) is defined in ASTM G173 as

$$V_T = \frac{\int \tau(\lambda)E(\lambda)d\lambda}{\int E(\lambda)d\lambda}, \tag{3.3}$$

among which $E(\lambda)$ is the solar spectral irradiance and $\tau(\lambda) = \tau_t/\tau_i$, where τ_t is the light transmitted through the sample and τ_i is the incident light.

Haze was calculated from the sample diffusion $\tau_{s,d}$ and the instrument diffusion $\tau_{i,d}$:

$$\text{Haze} = \tau_{s,d}/\tau_t - \tau_{i,d}/\tau_{i.} \tag{3.4}$$

The transparency color perceptions of PAM was depicted by the CIE 1931 chromaticity diagram, designed to represent the colors perceptible to human eyes. CIE tristimulus values were obtained using the CIE 1931 standard observer:

$$X = \int_{380}^{780} SPD(\lambda)\bar{x}(\lambda)d\lambda \tag{3.5}$$

$$Y = \int_{380}^{780} SPD(\lambda)\bar{y}(\lambda)d\lambda, \tag{3.6}$$

$$Z = \int_{380}^{780} SPD(\lambda)\bar{z}(\lambda)d\lambda. \tag{3.7}$$

where $\bar{x}(\lambda)$, $\bar{y}(\lambda)$, and $\bar{z}(\lambda)$ are the standard observer's color matching functions (CMFs) from ASTM E308. The CIE 1931 (x, y) chromaticity values are

$$x = \frac{X}{X+Y+Z} \tag{3.8}$$

$$y = \frac{Y}{X+Y+Z}. \tag{3.9}$$

The color difference between the TCS illuminated by the light through the sample and by the reference white light source was computed, and

$$CRI = 100 - 4.6\Delta E_{\mathrm{uvw}}, \tag{3.10}$$

where ΔE_{uvw} is the measured color difference.

3.2.4 Structural integrity of PAM

Robustness and resilience tests were performed on 4-layer PAM samples with the initial thickness of ~4 mm. The PET films were 0.125 mm thick and the air gap thickness was ~0.875 mm. Compression test was conducted by using a Type 5582 Instron machine. The loading rod had a 5-mm-radius round tip. The crosshead speed was set to 0.01 mm/s and the total displacement was 3.5 mm. 4000 loading-unloading cycles were applied and the thickness at the center point was measured periodically by a micrometer. To monitor the long-term stability, a PAM sample was placed in open lab air for one year (relative humidity: 50% to 60%), and the center-point thickness was measured periodically.

3.3 Modelling of thermal properties

Heat transfer through PAM depends on the solid and air heat conduction (R_{cond}), air convection in air gaps and at outer surface (R_{conv}), and the radiative heat flow across the reflective polymer film surfaces and glass pane surface (R_{rad}). Since the aspect ratio of PAM is greater than 40, the thermal properties may be investigated through 1D parallel plate analysis [19]. The following model was developed by Qingyang Wang in Professor Renkun Chen's lab in the University of California, San Diego.

Assume that there are *N* layers of polymer film and one glass pane. Each surface of film and glass pane is isothermal. The steady-state thermal balance equation of nodes is

$$\begin{aligned} q_{\mathrm{rad,ext}} + q_{\mathrm{conv,ext}} &= q_{\mathrm{cond,G}} \\ &= q_{\mathrm{rad,gap,i}} + q_{\mathrm{cond,gap,i}} + q_{\mathrm{conv,gap,i}} = q_{\mathrm{cond,P,i}} \\ &= q_{\mathrm{rad,in}} + q_{\mathrm{conv,in}} \end{aligned} \tag{3.11}$$

where $q_{\mathrm{rad,ext}}$ and $q_{\mathrm{conv,ext}}$ are radiative and convective heat fluxes from the weather side to the exterior window surface, respectively; $q_{\mathrm{cond,G}}$ and $q_{\mathrm{cond,P,i}}$ are conductive heat fluxes through the glass and the *i*-th layer of polymer film; $q_{\mathrm{rad,gap,i}}$, $q_{\mathrm{cond,gap,i}}$ and $q_{\mathrm{conv,gap,i}}$ are respectively the radiative, the conductive, and the convective heat fluxes through the air gaps; $q_{\mathrm{rad,in}}$ and $q_{\mathrm{conv,in}}$ are respectively the radiative and the convective heat fluxes from the innermost polymer film to the room side. Subscripts "in" and "ext" indicate interior and exterior, respectively; subscripts "cond", "rad", and "conv" indicate conduction, radiation, and convection, respectively; and "G", "gap", and "P" indicate window glass, air gap, and polymer film, respectively.

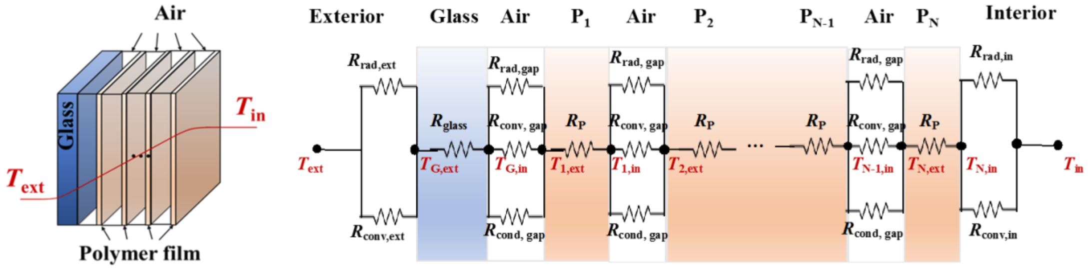

Figure 3.5 Thermal analysis for PAM. The thermal nodes represent, from the left to right, T_{ext}: the exterior temperature, $T_{G,ext}$ and $T_{G,in}$: the exterior and interior temperatures of window glass, $T_{i,ext}$ and $T_{i,in}$: the exterior and interior temperatures of the i-th layer of polymer film, and T_{in}: the interior temperature. According to ASTM C1199 and ASHRAE Handbook [20], the exterior weather side and the room side temperatures are set to T_{ext} = -18 °C and T_{in} = 21°C; the exterior heat transfer coefficient (h_{ext}) is 30 W/(m^2·K).

The conductive heat transfer through glass, air, and polymer film follows the Fourier law [21],

$$q_{cond} = -k\nabla T \tag{3.12}$$

where ΔT represents temperature difference and k is the medium thermal conductivity. The radiative heat transfer between two layers is governed by the Kirchhoff Law [19],

$$q_{rad,i} = \frac{\sigma\left({T_{i,ext}}^4 - {T_{i-1,in}}^4\right)}{\frac{1}{\varepsilon_{i,ext}} + \frac{1}{\varepsilon_{i-1,in}} - 1} \tag{3.13}$$

where the Stefan Boltzmann constant $\sigma = 5.67 \times 10^{-8}\ \mathrm{W/m^2K^4}$. The radiative heat transfer and the thermal resistance on the interior/exterior surface of innermost layer can be written as:

$$q_{\mathrm{rad,in}} = \varepsilon_{\mathrm{P}}\sigma\left({T_{\mathrm{in}}}^4 - {T_{N,\mathrm{in}}}^4\right) \tag{3.14}$$

$$q_{\mathrm{rad,ext}} = \varepsilon_{\mathrm{P}}\sigma\left({T_{G,\mathrm{ext}}}^4 - {T_{\mathrm{ext}}}^4\right)$$

For the convective heat transfer in air gap and at the outermost surfaces of window glass and polymer film, the heat flux is

$$q_{\mathrm{conv}} = h_{\mathrm{conv}}\Delta T \tag{3.15}$$

where h_{conv} is the convective heat transfer coefficient of air in air gap or at the outermost vertical surfaces. Churchill and Chu [20] derive the following equation for air convection adjacent to a vertical plane:

$$h_{\mathrm{conv,in}} = \frac{Nu \cdot k_{\mathrm{air}}}{L} \tag{3.16}$$

where *Nu* is the mean Nusselt number [22][23], k_{air} is the thermal conductivity of air, and *L* is the surface height. The thermal resistance can be expressed as

$$R = \frac{\Delta T}{q}. \tag{3.17}$$

Finally, *U*-factor can be calculated as

$$U = \Bigg[R_{\mathrm{rad,ext}} + R_{\mathrm{cond,G}} + \sum_{i=1}^{N}\left({R_{\mathrm{rad,gap,i}}}^{-1} + {R_{\mathrm{cond,gap,i}}}^{-1} + {R_{\mathrm{conv,gap,i}}}^{-1}\right)^{-1} + N \cdot R_{\mathrm{cond,P}} + \left({R_{\mathrm{rad,in}}}^{-1} + {R_{\mathrm{conv,in}}}^{-1}\right)^{-1}\Bigg]^{-1} \tag{3.18}$$

3.4 Results and discussion

3.4.1 Polymer electrification

Figure 3.6(a) and 3.6(b) illustratex typical results of dipolar voltage (V_d) distribution of a 125-μm-thick PET film charged with a needle voltage of 10 kV. Without the grid mesh between the needle electrode and the plate electrode, the dipolar voltage distribution fits with “bell jar shape”. As a grid mesh with the grid voltage (V_grid) of 2 kV is inserted in the system, the charges become much more uniform. The magnitude of V_d can be controlled by V_grid, as illustrated in Figure 3.6(c). Figure 3.6(d) shows the decay measurement result for the dipolar voltage of a 125-μm-thick 3×3” PET film exposed to lab air. The voltage was periodically measured for 9 months.

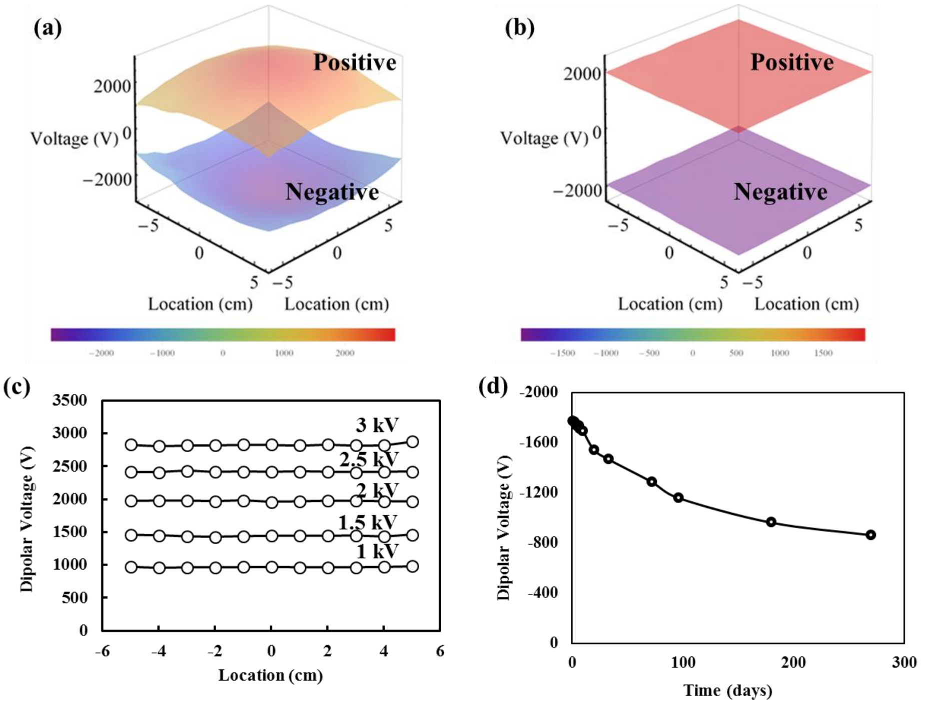

Figure 3.6 Dipolar voltage distribution of the positive and the negative sides of corona charged 125-μm-thick PET films (a) without mesh grid and (b) with a mesh grid (V_{grid}=2 kV). (c) Dipolar voltage distribution of PET films, with the mesh grid voltage varying from 1 kV to 3 kV, measured along the center line of the polymer film. (d) Dipolar voltage decay over 9 months. The initial dipolar voltage is -1.8 kV. The needle voltage is 10 kV; the needle-electrode distance is 4 cm; the charging duration is 60 s.

To better adjust the surface voltages, flow electrification provides “additional” surface charges (σ_s). As shown in Figure 3.7(a), with the increase in the SF concentration, the surface voltages of the negative side (V_{n}) and the positive side (V_{p}) were conditioned. The dipolar component was quite stable. When the grid voltage of corona charging was changed, the dipolar component of surface voltage was varied, as illustrated in Figure 3.7(b). For the pure dipolar-charged polymer film, the magnitudes of surface voltage at the positive side and the negative side are close to each other, so are the surface charge densities; i.e., $\sigma_p \approx \sigma_n$. Subscripts "p" and "n" indicate positive side and negative side, respectively.

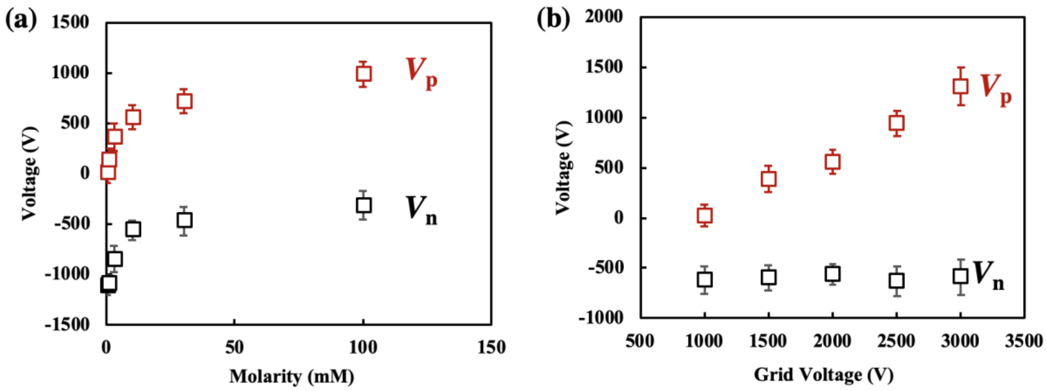

Figure 3.7 (a) Effects of the molarity of SF on the surface voltages of the positive and the negative sides. (b) Effects of grid voltage on the surface voltages of the positive and the negative sides. The negative sides of all the films are exposed to 10 mM SF solution. The samples are 125-µm-thick and 76.2 mm×76.2 mm large.

When two like-charged polymer films are placed in proximity, there would be a repulsive force, *F*. Repulsive pressure measurement was conducted on a set of 125-µm-thick 76.2 × 76.2 mm large PET films. The films were electrified through corona charging, with the grid voltage being 1 kV, 2 kV, or 3 kV. The negative sides were then liquid-electrified by 3 mM, 10 mM, or 100 mM SF solution. As shown in Fig.3.8, the repulsive pressure is significant, which helps separate the polymer films for PAM assembly. However, because the surface voltage would decrease over time (Fig.3.6d), it may not contribute to the long-term stability of the hollow structure.

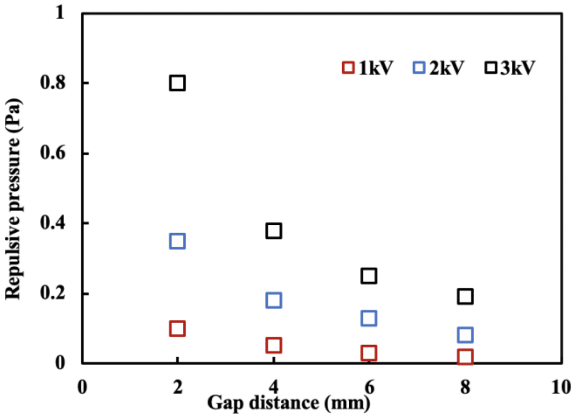

Figure 3.8 The effects of gap distance on the repulsive pressure between two dipolar-electrified polymer films.

3.4.2 *U*-factor evaluation

Four 0.3048-m-large polymer films were assembly into a PAM sample. The total thickness was ~6 mm. Figure 3.9(a) and 3.9(b) show the measurement results of T_{ext}, T_{in}, $T_{\text{PAM,ext}}$, $T_{\text{PAM,in}}$, and the heat flux q under different wind speeds at the exterior side. When the wind speed was increased, the temperatuer difference and the heat flux across the PAM sample became larger, while the *U*-factor did not vary much. The U-factor was calculated by Eq. (3.2) to be around 0.5 Btu/(h· $\text{ft}^2 \cdot$ °F).

Figure 3.9(c) shows the *U*-factor of a 4-layer and a 1-layer PAM sample with respect to the total thickness. The solid lines are the numerical predication, and the data dots are the measurement results. Clearly, the U-factor is much reduced when the total sample thickness is increased. The multilayer struture has better thermal insulation properties than the single layer structure.

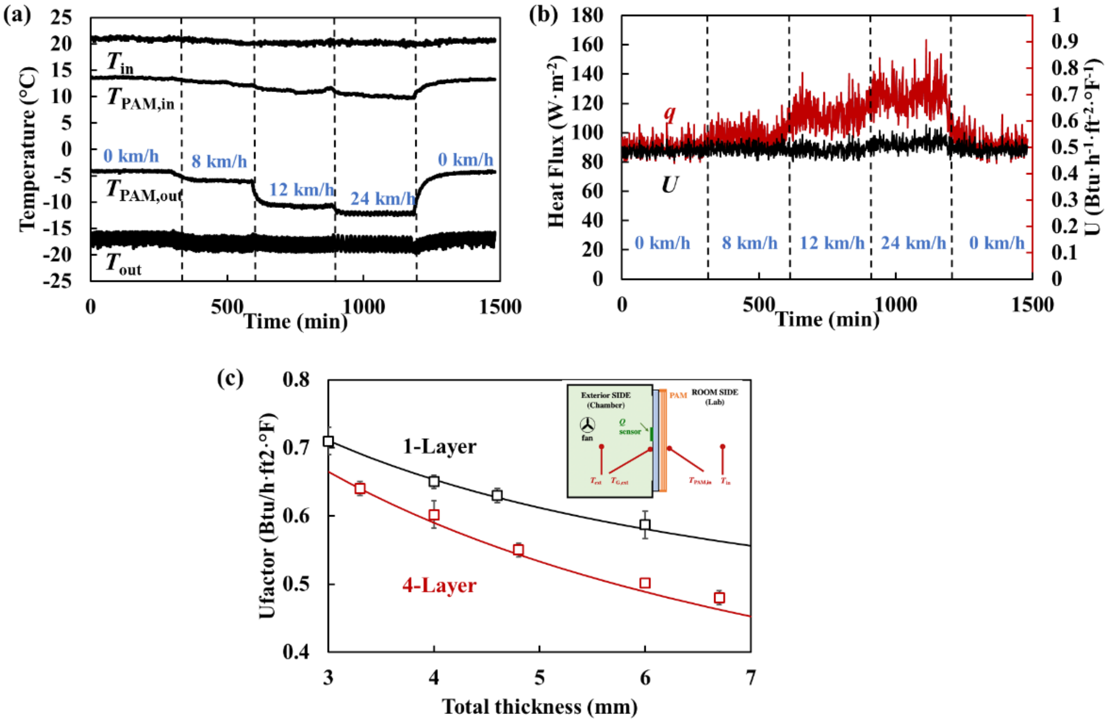

Figure 3.9 The exterior wind speed effect on the temperature difference across PAM and the U-factor. (a) T_{ext}, T_{in}, $T_{\text{PAM,ext}}$, and $T_{\text{PAM,in}}$ and (b) the heat flux q and U-factor at the steady state (t_{PAM}=6 ±0.1 mm). (c) The relationship between the U-factor and the total thickness of 1-Layer and 4-Layer PAM.

3.4.3 Optical properties

Figure 3.10 and Table 3.1 show the measured optical properties of a pristine PET film and a typical PAM sample (4 layers of 125-µm-thick PET films). The visual transmittance (Vt) of a single PET layer is 90.67%, and that of PAM is 76.44%, which is superior to most of low-emissivity films [12]. Although Vt of PAM is ~15% lower than that of a single PET layer, the effective emissivity of PAM is only 21% of pristine PET, which can much reduce the radiative heat conduction. The haze of PAM is lower than 2%. From the color coordinates CIE 1931 (x,y) and CRI values of PAM, it can be seen that it has good achromatic and neutral color sensation, and it is able to provide high-quality illumination with achromatic sensation.

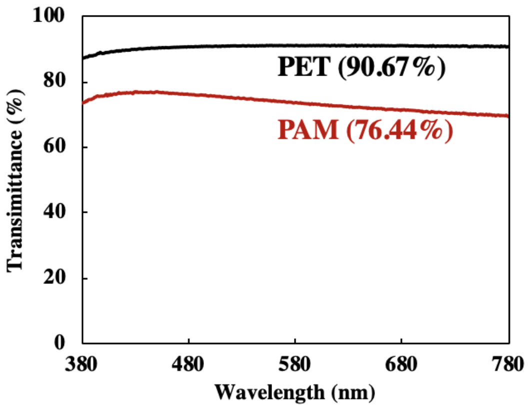

Figure 3.10 The visual transmittance of pristine PET film and PAM sample.

Table 3.1 Summary of the optical properties of PET

Optical properties		Pristine PET	PAM (PET-based)
V_T (%)		90.7	76.44
Emissivity (%)		76.4	16.73
Haze (%)		0.2	1.6
CRI	Color coordinates	(0.339319, 0.352434)	(0.334388, 0.347274)
	CRI value	99.66	95.5

3.4.4 Structural integrate

Figure 3.11(a) shows the compression test results of a 0.3048-m-large PAM sample, with the initial thickness (t_{PAM}) being ~4 mm. The force required to flatten the PAM sample is around 1.1 N. After 4000 times of repeated flattening, the hollow multilayer structure can still be restored instantaneously when the loading was removed, as illustrated in Figure 3.11(b). The satisfactory structural robustness should be attributed to the large aspect ratio. When the air gaps are flattened, the maximum strain in polymer films is less than 0.3%, well within than the linear elastic limit of PET [24].

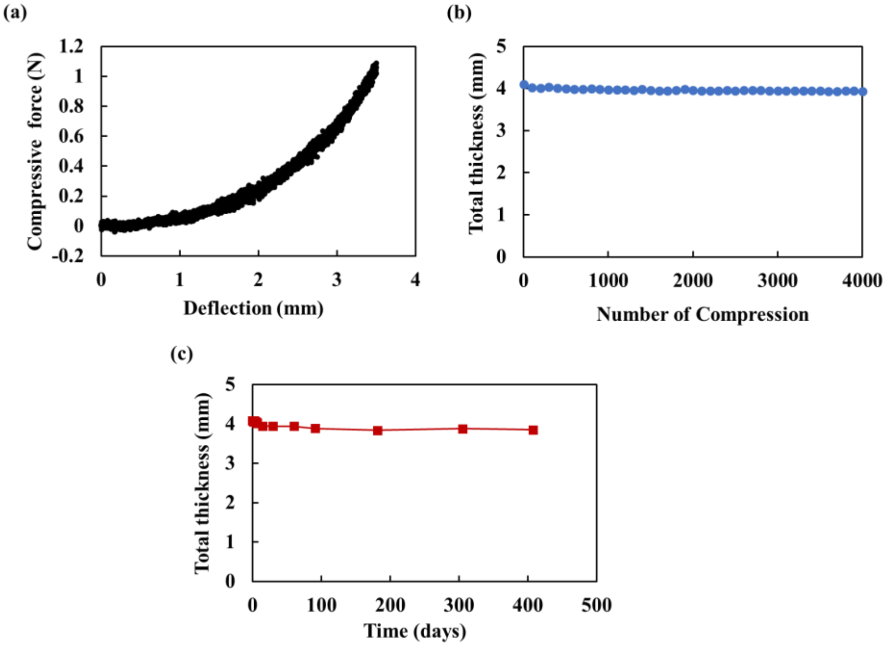

Figure 3.11 (a) Experimental results of compression of PAM. (b) The stability of air gap thickness upon repeated compression. (c) The stability of air gaps over time.

3.5 Installation

Figure 3.12 shows an on-site assembly and installation procedure of 4-Layer PAM, including: sectioning of polymer films, film clamping and stretching, spacer insertion, adhesive curing, trimming, and mounting. In general, like-charged PET films would not adhere to each other, relatively easy to handle. They will be shear-cut into size and shape. The clamp is a portable device formed by metal bars, which holds and separates the polymer films. The clamped PAM set is affixed on a stretcher, and the polymer films are slightly stretched. In this process, surface charging is beneficial. A small tensile force is sufficient to render the films planar, as they “float” on top of each other. Next, adhesive-sprayed spacer bars are inserted into the film stack along the edges. The structure is secured, as the adhesive is cured at room temperature for about 10 min. Finally, the edges of the PAM are trimmed, and the entire set is attached to a window pane, by using adhesives on the outer spacer bars at the edges. No adhesives is needed across the inner layer surface and the glass pane surface.

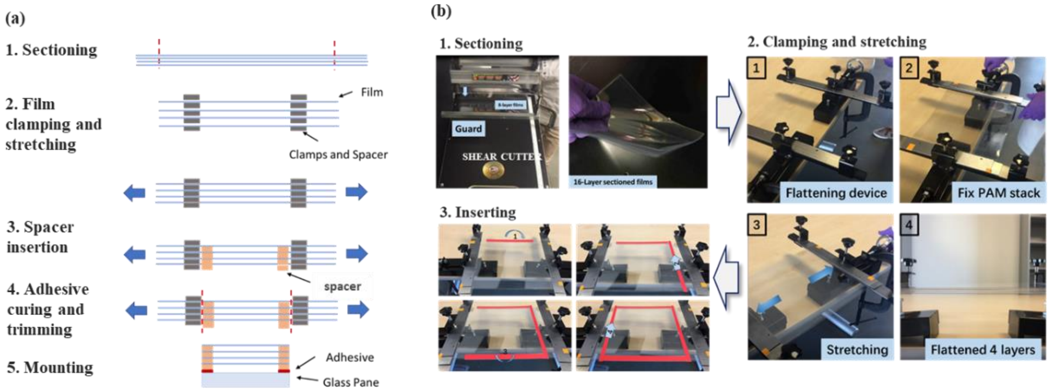

Figure 3.12 (a) a schematic of the installation of PAM. (b) Photos of demonstration for film sectioning, film clamping, stretching and spacer insertion.

3.6 Concluding remarks

To summarize, we investigate the transparent polymer-air multilayer (PAM) structure. Four flat 125-μm-thick PET films are separated by a set of spacer bars at the edges and mounted on the window glass pane. The air gap between adjacent layers is 0.5~1 mm thick. Corona charging followed by flow electrification can render the polymer surfaces like charged, which leads to a non-trivial repulsive pressure, helpful for materials handling, assembly, and installation. The surface voltage would decrease after a few months. Long-term structural stability of PAM is achieved by slightly stretching the films and keeping the aspect ratio ultra-large. It was measured that such 4-layer PAM had a low thermal transmittance (*U*-factor) less than 0.5 Btu/(h$\cdot$ ft$^2 \cdot$ °F), as the conductive, convective, and radiative heat transfer was all suppressed. The visual transmittance and haze of PAM were higher than 70% and lower than 2%, respectively. The emissivity was below 0.2. The PAM structure was flexible and resilient. There was no sign of degradation upon repeated flattening for 4000 cycles, or after exposure to lab air for 1 year. This technology not only is useful for retrofitting of single-pane windows, but also may be applied for electrical insulation, soundproof layers, as well as enhancement of double-pane and triple-pane IGUs.

Acknowledge

Chapter 3, in part, is currently being prepared to be submitted for publication. Rui Kou, Ying Zhong, Qingyang Wang, Jeongmin Kim, Renkun Chen and Yu Qiao. The dissertation author was the primary investigator and first author of the paper.

References

[1] US Department of Energy, Research and Development Roadmap for Emerging HVAC Technologies, US Dep. Energy, Build. Technol. Off. Washington, DC. (2014) 121.

[2] U.S. DoE, Buildings energy databook, Energy Effic. Renew. Energy Dep. (2011).

[3] T. Gao, B.P. Jelle, T. Ihara, A. Gustavsen, Insulating glazing units with silica aerogel granules: The impact of particle size, Appl. Energy. 128 (2014) 27–34.

[4] U. Berardi, The development of a monolithic aerogel glazed window for an energy retrofitting project, Appl. Energy. 154 (2015) 603–615.

[5] Y.-L. He, T. Xie, Advances of thermal conductivity models of nanoscale silica aerogel insulation material, Appl. Therm. Eng. 81 (2015) 28–50.

[6] H. Maleki, L. Durães, A. Portugal, An overview on silica aerogels synthesis and different mechanical reinforcing strategies, J. Non. Cryst. Solids. 385 (2014) 55–74.

[7] R.P. Patel, N.S. Purohit, A.M. Suthar, An overview of silica aerogels, Int. J. ChemTech Res. 1 (2009) 1052–1057.

[8] M. Reim, W. Körner, J. Manara, S. Korder, M. Arduini-Schuster, H.-P. Ebert, J. Fricke, Silica aerogel granulate material for thermal insulation and daylighting, Sol. Energy. 79 (2005) 131–139.

[9] R. Baetens, B.P. Jelle, A. Gustavsen, Aerogel insulation for building applications: a state-of-the-art review, Energy Build. 43 (2011) 761–769.

[10] X.-D. Wang, D. Sun, Y.-Y. Duan, Z.-J. Hu, Radiative characteristics of opacifier-loaded silica aerogel composites, J. Non. Cryst. Solids. 375 (2013) 31–39.

[11] Y. Zhong, R. Kou, M. Wang, Y. Qiao, Synthesis of centimeter-scale monolithic SiC nanofoams and pore size effect on mechanical properties, J. Eur. Ceram. Soc. 39 (2019) 2566–2573.

[12] C. Schaefer, G. Bräuer, J. Szczyrbowski, Low emissivity coatings on architectural glass, Surf. Coatings Technol. 93 (1997) 37–45.

[13] R.J. Martın-Palma, L. Vazquez, J.M. Martınez-Duart, Silver-based low-emissivity coatings for architectural windows: Optical and structural properties, Sol. Energy Mater. Sol. Cells. 53 (1998) 55–66.

[14] R. Kou, Y. Zhong, J. Kim, Q. Wang, M. Wang, R. Chen, Y. Qiao, Elevating low-emissivity film for lower thermal transmittance, Energy Build. 193 (2019) 69–77.

[15] N. Sándor, J. Schanda, Visual colour rendering based on colour difference evaluations, Light. Res. Technol. 38 (2006) 225–239.

[16] How Much Does Window Replacement Cost? | Angie's List, (n.d.). https://www.angieslist.com/articles/how-much-does-window-replacement-cost.htm (accessed March 22, 2019).

[17] Y. Zhong, R. Kou, M. Wang, Y. Qiao, Electrification Mechanism of Corona Charged Organic Electrets, J. Phys. D. Appl. Phys. (2019).

[18] R. Kou, Y. Zhong, Y. Qiao, Effects of anion size on flow electrification of polycarbonate and polyethylene terephthalate, Appl. Phys. Lett. 115 (2019) 73704.

[19] W. Elenbaas, Heat dissipation of parallel plates by free convection, Physica. 9 (1942) 1–28.

[20] A. Handbook, Fundamentals, Am. Soc. Heating, Refrig. Air Cond. Eng. Atlanta. 111 (2001).

[21] T.L. Bergman, F.P. Incropera, D.P. DeWitt, A.S. Lavine, Fundamentals of heat and mass transfer, John Wiley & Sons, 2011.

[22] F.M. White, I. Corfield, Viscous fluid flow, McGraw-Hill New York, 2006.

[23] J.L. Wright, A correlation to quantify convective heat transfer between vertical window glazings, ASHRAE Trans. 102 (1996).

[24] K.K. Chawla, M.A. Meyers, Mechanical behavior of materials, Prentice Hall Upper Saddle River, 1999.

Chapter 4 Hollow Bilayer Structure with Low-Emissivity Coating

4.1 Introduction

As discussed in the previous chapters, in order to enhance energy efficiency and energy security, it is imperative to develop advanced thermal insulating materials for building windows, especially to retrofit the large stock of single-pane windows. About 30~40% of present-day windows in the U.S. are still single-pane and they are responsible to ~50% total thermal energy loss associated with building heating, ventilation, and air conditioning (HVAC), which is ~4 quads per year [1][2]. The replacement rate of single-pane windows will be quite slow in the next 40~60 years [2]. The rate of heat loss through windows can be characterized by the *U*-factor. The *U*-factor of single-pane window is typically ~1 Btu/(h·ft^2·°F), much higher than the Energy Star standard (0.3 to 0.4 Btu/(h·ft^2·°F)) [3]. It is envisioned that if highly transparent, low-haze, and highly thermal insulating material can be produced and attached to single-pane windows, the energy saving and the improvement in occupant comfort would be significant.

Conventional thermal insulating materials, such as silica aerogels, suffer poor haze and poor structural integrity [4,5]. Low-emissivity (low-e) films can block a considerable portion of infrared (IR) radiation, yet does not reduce thermal conductivity; their efficiency may be largely reduced if water condensation is formed in a cold weather, as the conductive thermal transport through water layer becomes the dominant factor [6,7].

In Chapter 3, we investigated the concept of polymer-air multilayer (PAM), which is both low-e and thermal insulating [8,9]. The previously developed PAM comprised four polymer layers fully separated by air gaps from glass pane; the layer separation is aided by polymer electrification [9,10]. Although multilayer polymer films block a large portion heat loss by radiation, the overall radiative thermal resistance is still much lower than that blocked by a low-e film [8]. To further increase the radiative thermal resistance of PAM, a low-e coating can be applied on its outer surface. However, because low-e coating would reduce the visual transmittance (V_t) by more than ~20% [11][12], to keep the overall visual transmittance (V_t) above 0.7, only 1 inner polymer layers can be placed between the low-e layer and the window pane, based on the assumption that V_t of polymer is ~90% [8]. In this chapter, we construct and characterize a 2-layer (2L) PAM, with the outer surface being enhanced by a low-e coating. Compared with the 4-layer (4L) PAM in Chapter 3, it has a lower emissivity, and is easier to install.

4.2 Modelling of thermal properties

As depicted in Figure 4.1, the 2L-PAM consisted of two layers of polymer films, mounted on a glass pane. The polymer films and the glass pane were separated by air gaps about 1.25~2.25 mm thick. A low-e coating was attached to the outer polymer film, facing the indoor temperature (T_{in}); the glass pane is exposed to the exterior weather side, with temperature of $T_{\mathrm{ext.}}$ Because the aspect ratio of 2L-PAM is larger than 40, the heat transfer model will be simplified as an one-dimensional (1D) parallel-plates system [13]. The important factors include the solid/air heat conduction (R_{cond}), the air convection at outer surface and in air gaps (R_{conv}), and the radiative heat flow across the reflective surfaces (R_{rad}). The model was originally developed by Mr. Qingyang Wang in Professor Renkun Chen's group at the University of California, San Diego.

Consider one glass pane and two polymer films (indicated by "1" and "2", separately). The outer polymer film (layer 2) has a low-e coating. Assume that all surfaces are isothermal. The steady state thermal balance equation of all nodes can be written as

$$\begin{aligned} q_{\mathrm{rad,ext}} + q_{\mathrm{conv,ext}} &= q_{\mathrm{cond,G}} \\ &= q_{\mathrm{rad,gap,i}} + q_{\mathrm{cond,gap,i}} + q_{\mathrm{conv,gap,i}} = q_{\mathrm{cond,P,i}} \\ &= q_{\mathrm{rad,in}} + q_{\mathrm{conv,in}} \end{aligned} \tag{4.1}$$

where, $q_{\mathrm{rad,ext}}$ and $q_{\mathrm{conv,ext}}$ are the radiative and the convective heat fluxes from the weather side to the exterior window surface, respectively; $q_{\mathrm{cond,G}}$, and $q_{\mathrm{cond,P,i}}$ are the conductive heat fluxes through the glass and the *i*-th layer of polymer film, respectively

(i = 1,2); $q_{\mathrm{rad,gap,i}}$, $q_{\mathrm{cond,gap,i}}$ and $q_{\mathrm{conv,gap,i}}$ are the radiative, the conductive, and the convective heat fluxes through the air gaps, respectively; $q_{\mathrm{rad,in}}$ and $q_{\mathrm{conv,in}}$ are the radiative and the convective heat fluxes from the outmost polymer film to the room side, respectively; subscripts "in" and "ext" indicate interior and exterior, respectively; subscripts "cond", "rad", and "conv" indicate conduction, radiation, and convection, respectively; and "G", "gap", "P", and "Lowe" indicate window glass, air gap, polymer film and low-e coating, respectively.

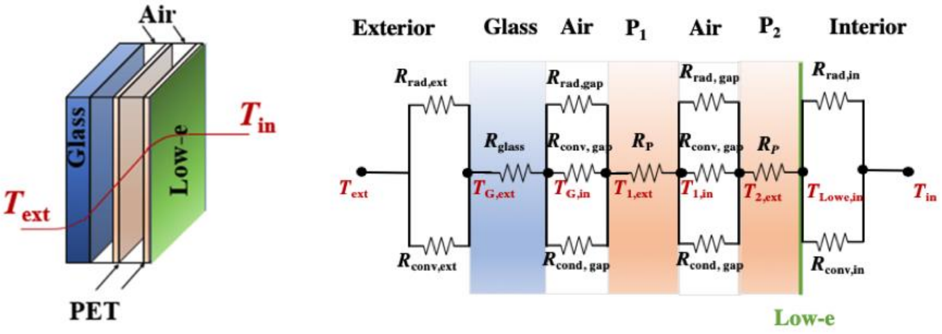

Figure 4.1 Thermal analysis for 2L-PAM. From the left to right, the thermal nodes represent T_{ext}: the exterior temperature, $T_{\mathrm{G,ext}}$ and $T_{\mathrm{G,in}}$: the exterior and interior temperatures of window glass, $T_{\mathrm{P,ext}}$ and $T_{\mathrm{P,in}}$: the exterior and interior temperatures of polymer film, $T_{\mathrm{Lowe,in}}$: the interior temperatures of the polymer film with low-e coating, and T_{in}: the interior temperature. According to ASTM C1199 and ASHRAE Handbook [14], the exterior weather side and the room temperatures are set to T_{ext} = -18 ℃ and T_{in} = 21℃, respectively; the exterior heat transfer coefficient (h_{ext}) is 30 W/(m^2·K).

The conductive heat transfer in solid and air follows the Fourier law [15],

$$q_{\mathrm{cond}} = -k\nabla T \tag{4.1}$$

where ∇T is temperature gradient and k is the medium thermal conductivity. The radiative heat transfer between two nodes is governed by the Kirchhoff Law [13],

$$q_{\mathrm{rad},i} = \frac{\sigma\left({T_{i,\mathrm{ext}}}^4 - {T_{i-1,\mathrm{in}}}^4\right)}{\frac{1}{\varepsilon_{i,\mathrm{ext}}} + \frac{1}{\varepsilon_{i-1,\mathrm{in}}} - 1} \tag{4.2}$$

where the Stefan Boltzmann constant $\sigma = 5.67 \times 10^{-8}\ \mathrm{W/m^2K^4}$. The radiative heat transfer and the thermal resistance on the interior/exterior surface of PAM can be written as:

$$q_{\mathrm{rad,in}} = \varepsilon_{\mathrm{Lowe}}\sigma\left({T_{\mathrm{in}}}^4 - {T_{\mathrm{Lowe,in}}}^4\right) \tag{4.3}$$

$$q_{\mathrm{rad,ext}} = \varepsilon_{\mathrm{G}}\sigma\left({T_{G,\mathrm{ext}}}^4 - {T_{\mathrm{ext}}}^4\right)$$

The convective heat transfer in air gaps and at the outer surfaces of window glass and polymer film can be calculated by

$$q_{\mathrm{conv}} = h_{\mathrm{conv}}\Delta T \tag{4.4}$$

where h_{conv} is the convective heat transfer coefficient of air. Churchill and Chu [14] derived the following equation for air convection adjacent to a vertical plane:

$$h_{\mathrm{conv,in}} = \frac{Nu \cdot k_{\mathrm{air}}}{L} \tag{4.5}$$

where Nu is the mean Nusselt number [16][17], k_{air} is the thermal conductivity of air, and L is the surface height. The thermal resistance can be expressed as

$$R = \frac{\Delta T}{q}. \tag{4.6}$$

where ΔT is the temperature difference between two nodes and q is the heat flux through them. Finally, U-factor can be calculated as

$$U = \left[R_{\mathrm{rad,ext}} + R_{\mathrm{cond,G}} + \sum_{i=1}^{N} \left({R_{\mathrm{rad,gap,i}}}^{-1} + {R_{\mathrm{cond,gap,i}}}^{-1} + {R_{\mathrm{conv,gap,i}}}^{-1} \right)^{-1} + N \cdot R_{\mathrm{cond,P}} + \left({R_{\mathrm{rad,in}}}^{-1} + {R_{\mathrm{conv,in}}}^{-1} \right)^{-1} \right]^{-1} \tag{4.7}$$

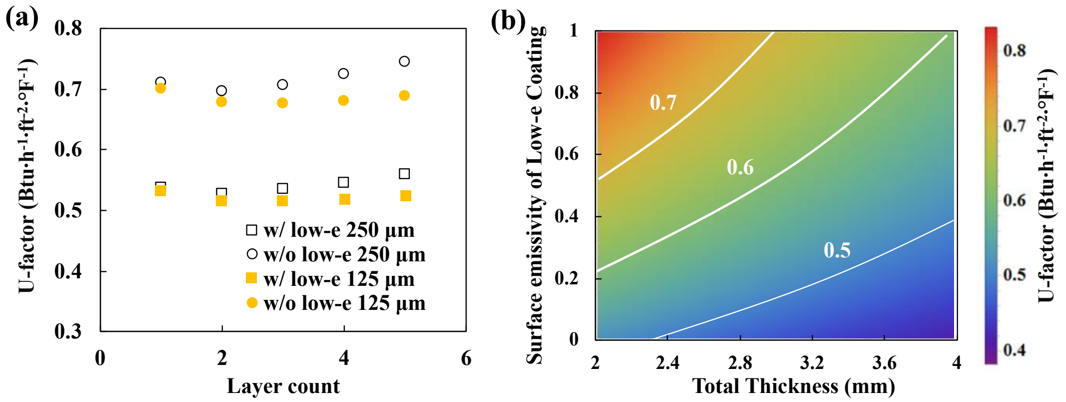

Figure 4.2 (a) The effects of the layer count and the low-e coating on the *U*-factor. The total thickness is 3 mm; "w/" indicates "with"; "w/o" indicates "without"; the numbers in the legend indicate the polymer layer thickness. The emissivity of low-e coating on the outer surface is 0.14. (b) The *U*-factor of 2L-PAM as a function of the total thickness and the surface emissivity of low-e coating.

The influence of the layer count and the low-e coating on the *U*-factor was analyzed. As shown in Figure 4.2(a), when the total thickness of PAM is 3 mm and the polymer layer thickness is 250 μm or 125 μm, the *U*-factor of 2L-PAM is lower than that of a 1-Layer PAM; i.e., the thermal insulating is more effective. When the layer count is further increased, although $R_{\mathrm{rad,gap}}$ is enhanced, $R_{\mathrm{cond,gap}}$ would be reduced, because the air gaps are thinner. Thus, the *U*-factor remains constant or even increase. With the overall optical properties of multiple polymer films being taken into consideration, the 2-layered design is optimum. Figure 4.2(b) shows the *U*-factor as a function of the total 2L-PAM thickness and the surface emissivity of low-e coating. The polymer film thickness is 250 μm. The glass thickness is 1 cm. The surface emissivity of glass and polymer film are 0.84 and 0.76, respectively. It can be seen that increasing the air gap thickness and reducing the surface emissivity are beneficial. With the low-e coating with the surface emissivity $\varepsilon = 0.14$, the *U*-factor of a 3-mm-thick 2L-PAM is ~0.52 Btu/(h$\cdot$ ft$^2 \cdot$ °F).

4.3 Experimental procedure and results

To investigate the 2-layered design experimentally, 2L-PAM sample was formed by two 250-μm-thick 0.3×0.3 m polyethylene terephthalate (PET) films, while the second layer being coated by a 3M Thinsulate CC7 low-e film (Fig.4.3). The PET films were ultrasonically cleaned in isopropyl alcohol (IPA) for 10 min and then in de-ionized (DI) water for 5 min. The 3M low-e film was firmly attached on the surface of a PET film. The low-e coated PET film was separated from another uncoated PET film by four polycarbonate (PC) bars at the edges. The two-layered frame was mounted on a 10-mm-thick 355.6-mm-large glass pane, with two sets of 0.25’’-wide PC spacer bars along the boundary. The spacer thickness ranged from 1.5 mm to 2.5 mm, which controlled the air gap to the glass pane. The PC bars were affixed by an epoxy adhesive

(3M CA4) cured at room temperature. Figure 4.3 (b-c) show the typical sample configuration.

Figure 4.3(d) shows the installation procedure of 2L-PAM. First, window glass is measured. The polymer films and spacers are sectioned by a cutter into size. Then, through the adhesive layer of the low-e film, it is firmly attached to the outer PET film. The two PET films are assembled into a frame, and affixed to the glass pane through spacer bars. To save the installation time, the spacer can be L-shaped.

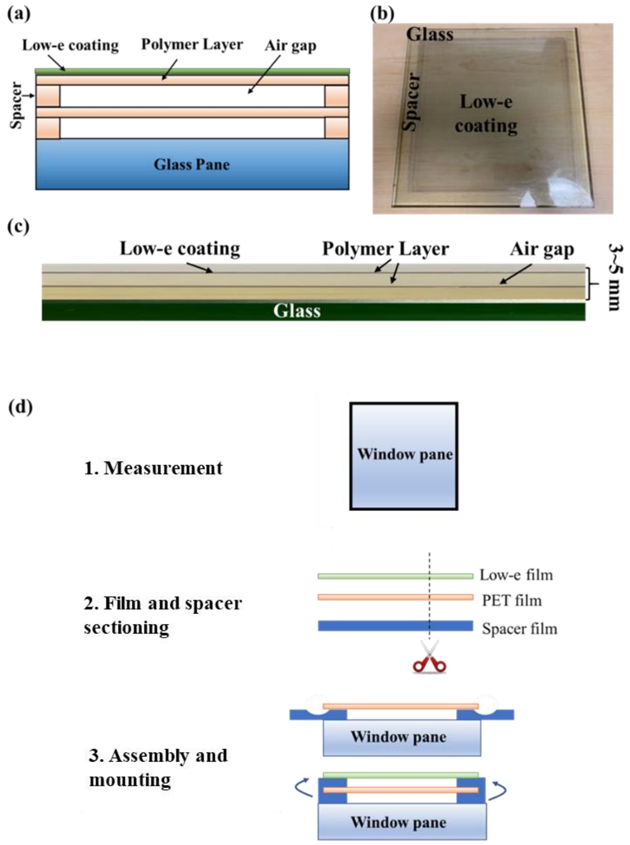

Figure 4.3 (a) A schematic of the 2L-PAM. (b) Top view and c) side view. (d) The installation procedure.

4.3.1 Sample characterization

U-factor measures the overall thermal transmittance, including conduction, convection, and radiation. A *U*-factor measurement system was designed and fabricated following ASTM C1199, ASTM C518, NFRC-100, and NFRC-102, originally developed by Dr. Jeongmin Kim in Professor Renkun Chen's group at the University of California, San Diego. Figure 4.4(a-b) shows the schematic and a photo. Inside a 0.39-m-long 0.47-m-wide 0.47-m-tall environmental chamber, T_{ext} was maintained at -18 °C. A 2L-PAM with glass pane was mounted on the opening of the side wall of the chamber. The 2L-PAM sample faced to the room, as shown in Figure 4.4(b). The room temperature (T_{in}), the chamber temperature (T_{ext}), the exterior surface temperature of glass ($T_{\mathrm{G,ext}}$), and the interior surface temperature of PAM ($T_{\mathrm{PAM,in}}$) were monitored by four Omega type-K thermocouples. A gSKIN-XI heat flux sensor was installed on the interior surface of the 2L-PAM to monitor the heat flux. A fan was operated in the chamber, to control the wind speed at the exterior side of window glass.

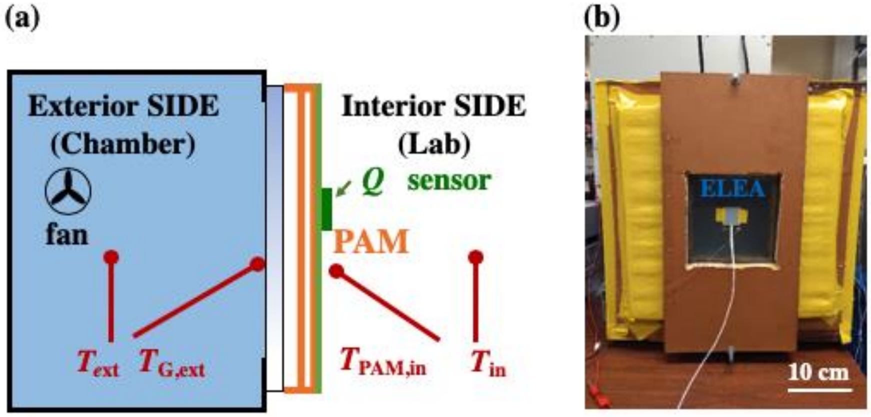

Figure 4.4 (a) Schematic and (b) a photo of the *U*-factor measurement setup.

U-factor is calculated as the reciprocal of the total thermal resistance:

$$U = \left(\frac{1}{h_{\mathrm{ST,ext}}} + \frac{T_{\mathrm{PAM,in}} - T_{\mathrm{PAM,ext}}}{q} + \frac{1}{h_{\mathrm{ST,in}}}\right)^{-1} \tag{4.8}$$

where, according to ASTM C1199 and NFRC-100, the standard boundary heat transfer coefficients to the exterior side ($h_{\mathrm{ST,ext}}$) is set to 30 W/(m^2·K); the interior side coefficient ($h_{\mathrm{ST,in}}$) is

$$h_{\mathrm{ST,in}} = 1.46\left[\frac{T_{\mathrm{in}} - T_{\mathrm{PAM,in}}}{H}\right]^{0.25} + \tag{4.9}$$

$$\sigma\varepsilon\left[\frac{(T_{\mathrm{in}}+273.16)^4 - \left(T_{\mathrm{PAM,in}}+273.16\right)^4}{T_{\mathrm{in}} - T_{\mathrm{PAM,in}}}\right];$$

H is the sample height (0.3 m); $\sigma = 5.67 \times 10^{-8}\ \mathrm{W/m^2 \cdot K^4}$ is the Stefan Boltzmann constant; and $\varepsilon = 0.14$ is the surface emissivity of low-e coating.

Figure 4.5(a-b) gives the measurement results of T_{ext}, T_{in}, $T_{\mathrm{PAM,ext}}$, and $T_{\mathrm{PAM,in}}$, and the heat flux q of a ~3 mm thick 2L PAM. The *U*-factor is 0.51 Btu/(h· ft^2 ·

°F), calculated from Eq.(3.2). Figure 4.5(c) shows the effects of the wind speed in the environmental chamber on the temperature difference across the 2L-PAM sample, and the adjusted *U*-factor. When the exterior heat transfer coefficient is changed by the wind speed, the temperature difference and the heat flux become larger. Since $h_{\mathrm{ST,ext}}$ is standard in Eq. (4.9), the adjusted *U*-factor is insensitive to the exterior wind speed.

Figure 4.5(d) shows the effects of the low-e coating and the total sample thickness. The solid lines are the numerical predication, and the data points are from the measurement. Clearly, the *U*-factor is much reduced when the sample is thicker or a low-e coating is applied.

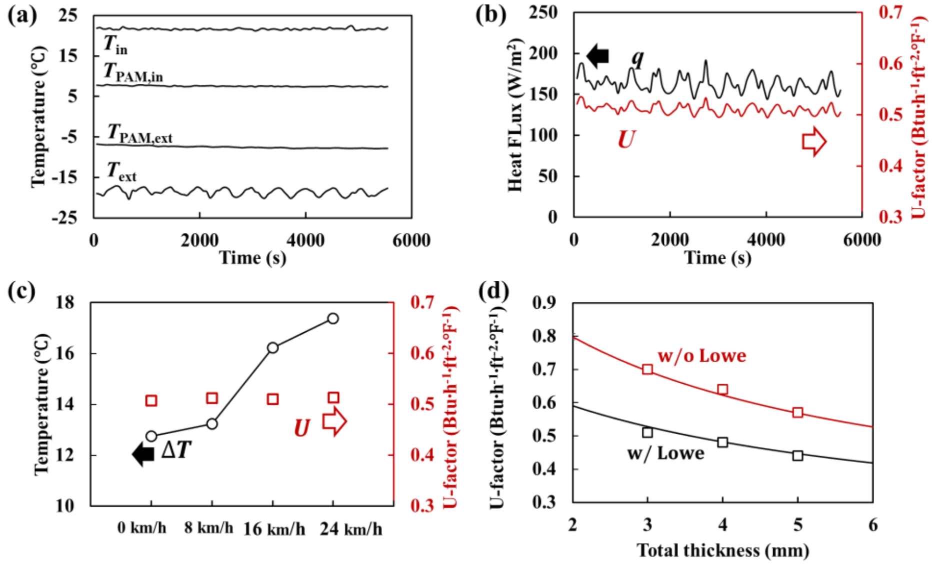

Figure 4.5 (a) T_{ext}, T_{in}, $T_{\mathrm{PAM,ext}}$, and $T_{\mathrm{PAM,in}}$ and (b) the heat flux *q* and the *U*-factor at the steady state. (c) The influence of the exterior wind speed on ΔT and *U*-factor. The total thickness of 2L-PAM is 3±0.1 mm. (d) the relationship between the *U*-factor and the total 2L-PAM thickness, and the low-e coating effect. “w/” indicates with; “w/o” indicates “without”; “lowe” indicates “low-e coating”.

4.3.2 Optical properties

Visual transmittance and haze measurement were conducted at the spectral range from 380 nm to 750 nm by a JASCO V770 UV-VIS spectrometer, following ASTM D1003. The spectrophotometer was equipped with an integrating sphere accessory. During the measurement, a 2L-PAM sample was placed in front of the sphere entrance port, through which light can pass into the sphere and be fully collected. The visible light transmittance (V_T) is defined in ASTM G173 as

$$V_T = \frac{\int \tau(\lambda)E(\lambda)d\lambda}{\int E(\lambda)d\lambda}, \qquad (4.10)$$

where $E(\lambda)$ is the solar spectral irradiance, $\tau(\lambda) = \tau_t/\tau_i$, τ_t is the light transmitted through the sample, and τ_i is the incident light. Haze can be calculated from the sample diffusion $\tau_{s,d}$ and the instrument diffusion $\tau_{i,d}$:

$$\text{Haze}= \tau_{s,d}/\tau_t - \tau_{i,d}/\tau_{i.} \qquad (4.11)$$

The transparency color perceptions of 2L-PAM was shown by the CIE 1931 chromaticity diagram, which is designed to represent the colors perceptible to human eyes. The CIE 1931 (x, y) chromaticity values are

$$x = \frac{X}{X+Y+Z} \qquad (4.15)$$

$$y = \frac{Y}{X+Y+Z}. \qquad (4.16)$$

among which X, Y, and Z are CIE tristimulus values, obtained by a CIE 1931 standard observer. The color difference between the TCS illuminated by the light through the sample and by the reference white light source was computed, and the color rendering index was assessed as

$$CRI = 100 - 4.6\Delta E_{\text{uvw}}, \tag{4.17}$$

where ΔE_{uvw} is the measured color difference.

Figure 4.6(a) shows the visual transmittance of 2L-samples with and without low-e coating. According to Eqs. (4.10) and (4.11), V_T of these samples are 70.8% and 83.6%, respectively. Although the low-e coating reduces V_T by nearly 13%, it reflects more infrared light and can block the radiation energy dissipation. The haze values are 0.4% and 0.8%, respectively, both adequate for window applications [8]. In Table 4.1, the values of color coordinates CIE 1931 (x, y) and CRI are shown. The color coordinates for both samples are located in the low colorfulness region in the CIE chromaticity diagram, indicating that the samples have desired ability to accurately present colors.

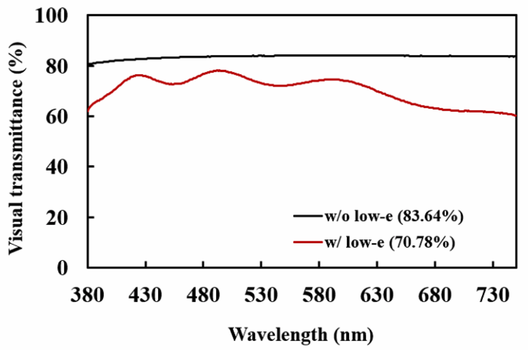

Figure 4.6 The visual transmittance of 2L-PAM with or without low-e coating.

Table 4.1 Summary of the optical properties of 2L-PAM (without glass)

Optical properties		without low-e coating	with low-e coating
V_T (%)		87.0	70.4
Emissivity (%)		76.4	14.2
Haze (%)		0.4	0.8
CRI	Color coordinates	(0.340305,0.351874)	(0.336798, 0.352643)
	CRI value (%)	99.68	94.29

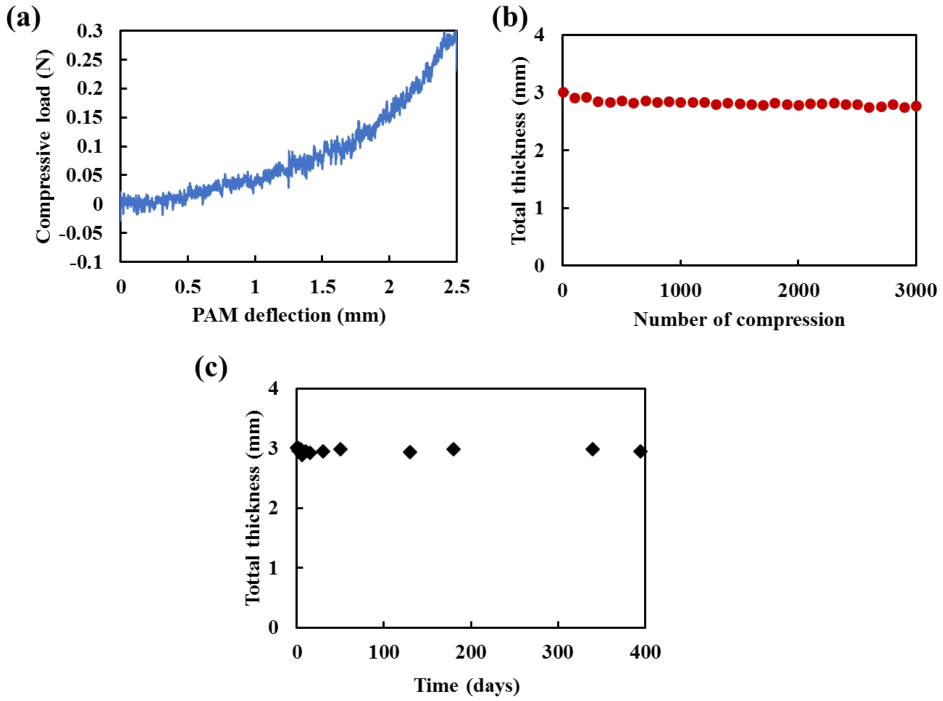

Figure 4.7 (a) A typical compression curve of a 2L-PAM sample. (b) The stability of air gaps upon repeated compression. (c) The stability of air gaps over time.

4.3.3 Structural properties

The structural integrate of a 0.3-m-large 2L-PAM was evaluated through compression tests in a Type 5582 Instron machine. The initial thickness of the 2L-PAM was 3 mm. The PET films were 0.25 mm thick and the air gap in between was 1.25 mm. The loading rod had a 5-mm-radius round tip. It was compressed by the Instron machine as a speed of 0.01 mm/s to the 2L-PAM sample. The total displacement was 2.5 mm. Figure 4.7(a) shows the compression test results. The force required to flatten the PAM sample was around 0.3 N. The sample was repeatedly flattened for more than 3,000 cycles, and the thickness of the center point was monitored by a micrometer. Figure 4.7(b) shows that the hollow structure was able, able to self-restore when the loading was removed. To monitor the long-term stability of 2L-PAM, a sample was placed in open lab air for one year, with the relative humidity of 50-60%. The gap thickness was monitored periodically, which was quite stable. Since the service lives of PET and low-e film are over 10 years [11][18], we expect that the service life of PAM will be at least 5 years.

4.4 Concluding remarks

We investigate the 2-layer polymer-air multilayer (2L-PAM) structure. It consists of 1 outer low-e coated polymer film and 1 inner uncoated polymer film, separated by a set of spacer bars. The 2L-PAM is mounted on the window glass, lifted by another set of spacer bars. Thanks to the air gaps and the low-e coating, the thermal transmittance (*U*-factor) of a 3-mm-thick 2L-PAM mounted on a 10-mm-thick window glass pane is as low as 0.51 Btu/(h$\cdot$ ft$^2 \cdot$ °F), as the conductive, convective, and radiative heat transfer are all suppressed. The visual transmittance and haze of 2L-PAM are around 70% and lower than 1%, respectively, satisfactory to the window applications. The emissivity of outer surface is 14%. Because of the excellent mechanical properties of PET films, the 2L-PAM structure is flexible and resilient. There is no sign of structural degradation upon 3000 loading-unloading cycles or after exposure to lab air for 1 year. This technique not only can be used for building windows, but also may have wide applications for electrical insulation, soundproof layers, etc.

Acknowledge

Chapter 4, in part, is currently being prepared to be submitted for publication. Rui Kou, Ying Zhong, Qingyang Wang, Jeongmin Kim, Jian Zeng, Renkun Chen and Yu Qiao. The dissertation author was the primary investigator and first author of the paper.

References

[1] US Department of Energy, Research and Development Roadmap for Emerging HVAC Technologies, US Dep. Energy, Build. Technol. Off. Washington, DC. (2014) 121.

[2] U.S. DoE, Buildings energy databook, Energy Effic. Renew. Energy Dep. (2011).

[3] Single -Pane Highly Insulating Efficient Lucid Designs (SHIELD) Program Overview, (2014) 1–13.

[4] Y.-L. He, T. Xie, Advances of thermal conductivity models of nanoscale silica aerogel insulation material, Appl. Therm. Eng. 81 (2015) 28–50.

[5] R.C. Team, J.M. (2012). T. (No. 536. 7). M.-H. (2012). T. (No. 536. 7). M.-H. ĐCengel, Y. A. B., ĐCengel, M. A. Y. A., Boles, M. A., ĐCengel, Y. A. C., ĐCengel, J. M. Y. A., & Cimbala, 1995. MILLS, Anthony F. Transferencia de calor. Irwin, G. Payerle, Silica aerogel granulate material for thermal insulation and daylighting, Prof. Psychol. 3 (1981) 45. doi:10.1163/_q3_SIM_00374.

[6] A. Kaklauskas, E.K. Zavadskas, S. Raslanas, R. Ginevicius, A. Komka, P. Malinauskas, Selection of low-e windows in retrofit of public buildings by applying multiple criteria method COPRAS: A Lithuanian case, Energy Build. 38 (2006) 454–462.

[7] G. Alvarez, M.J. Palacios, J.J. Flores, A test method to evaluate the thermal performance of window glazings, Appl. Therm. Eng. 20 (2000) 803–812. doi:10.1016/S1359-4311(99)00065-4.

[8] R. Kou, Y. Zhong, J. Kim, Q. Wang, M. Wang, R. Chen, Y. Qiao, Elevating low-emissivity film for lower thermal transmittance, Energy Build. 193 (2019) 69–77.

[9] Y. Zhong, R. Kou, M. Wang, Y. Qiao, Electrification Mechanism of Corona Charged Organic Electrets, J. Phys. D. Appl. Phys. (2019).

[10] R. Kou, Y. Zhong, Y. Qiao, Effects of anion size on flow electrification of polycarbonate and polyethylene terephthalate, Appl. Phys. Lett. 115 (2019) 73704.

[11] C. Schaefer, G. Bräuer, J. Szczyrbowski, Low emissivity coatings on architectural glass, Surf. Coatings Technol. 93 (1997) 37–45.

[12] R.J. Martın-Palma, L. Vazquez, J.M. Martınez-Duart, Silver-based low-emissivity coatings for architectural windows: Optical and structural properties, Sol. Energy Mater. Sol. Cells. 53 (1998) 55–66.

[13] W. Elenbaas, Heat dissipation of parallel plates by free convection, Physica. 9 (1942) 1–28.

[14] A. Handbook, Fundamentals, Am. Soc. Heating, Refrig. Air Cond. Eng. Atlanta. 111 (2001).

[15] T.L. Bergman, F.P. Incropera, D.P. DeWitt, A.S. Lavine, Fundamentals of heat and mass transfer, John Wiley & Sons, 2011.

[16] F.M. White, I. Corfield, Viscous fluid flow, McGraw-Hill New York, 2006.

[17] J.L. Wright, A correlation to quantify convective heat transfer between vertical window glazings, ASHRAE Trans. 102 (1996).

[18] S.C. Tjong, Structural and mechanical properties of polymer nanocomposites, Mater. Sci. Eng. R Reports. 53 (2006) 73–197.

Chapter 5 Elevating Low-emissivity Film for Lower Thermal Transmittance

5.1 Introduction

As discussed in the previous chapters, each year in the U.S., ~15 quads of energy is consumed for building heating, ventilation, and air conditioning (HVAC), ~25% of which (~4 quads) is lost through building windows in cold weather [1]. In newer buildings, double-pane windows have been widely adopted and they offer satisfactory thermal insulation [2]; in older buildings, however, single-pane windows are dominant, which accounts for over half of the total energy lost through building windows [3]. If all the remained single-pane windows could be replaced by double-pane windows, about 1.2 quads would be saved per year [1]. Yet, windows replacement is costly (\$50~100/ft^2 with installation [4]) and slow (only 2% single-pane windows per year are removed [5]). It is imperative to develop advanced and effective retrofitting techniques that are low cost, fast, and can offer a low thermal transmittance [6,7].

The unique functional requirements of window pane retrofitting impose tough technical challenges. Visual transmittance (V_T) must be high, desirably higher than 70%. Haze must be low, desirably less than 2%. The thermal insulation efficiency must be excellent, desirably with the thermal transmittance (*U*-factor) reduced from 1~1.2 Btu/h·ft^2·°F to less than 0.5 Btu/h·ft^2·°F. Moreover, the structure must be reliable and robust. A relatively mature technique of window insulation is to use low-emissivity (low-e) films [8]. With a thin coating of metal-based multilayer or doped semiconductor with a wide band gap, a low-e film minimizes the amount of the infrared (IR) light that passes through window glass [9,10]. One hurdle that blocks low-e films from being more widely applied is their time-consuming and expensive installation procedure [11]. To prevent wrinkle formation and to ensure perfect bonding with window pane, low-e film installation demands careful window pane preparation and is usually performed by professional installers. Probably more critically, in cold weather when the temperature difference across the coated window pane (∇T) is large, water condensation would be formed and with the large specific heat of the water layer, heat conduction becomes the dominant heat loss mechanism, and the benefit of the reduction in radiative heat transfer is significantly reduced.

In the current chapter, we investigate an alternative installation approach of low-e films. By using a polymer substrate, a low-e film can be conveniently elevated from window pane and form an air gap, improving the thermal insulation and preventing water condensation with a relatively large ∇T. It may be viewed as a simplified version of the 2-layer polymer-air multilayer (2L-PAM) presented in Chapter 4. Compared with 2L-PAM, the single-layer structure in this chapter is simpler, more cost efficient, easier to install, and has similar thermal and optical properties. The air gap increases the conductive thermal resistance and low-e coating decreases the IR heat transfer. Optical measurement indicates that desired visual transmittance and haze are achieved. Mechanical testing demonstrates satisfactory resilience and robustness.

5.2 Modelling of thermal properties

Figure 5.1 depicts an elevated low-e assembly (ELEA), consisting of a low-e film, a glass pane, and a mm-thick air gap in between. The low-e film is exposed to the interior temperature (T_{in}), and the glass pane faces the exterior temperature (T_{ext}). The aspect ratio of ELEA is greater than 40, and its thermal properties can be examined through one-dimensional parallel plate analysis [12]. We take into consideration the heat conduction of solid and air (R_{cond}), the convection in air gap and at outer surfaces (R_{conv}), and the radiation through reflective low-e surface and glass pane (R_{rad}). Conductive, convective and radiative thermal transfers through the air layer are characterized by parallel thermal resistance $R_{\mathrm{cond,gap}}$, $R_{\mathrm{conv,gap}}$ and $R_{\mathrm{rad,gap}}$ respectively. The radiative resistance ($R_{\mathrm{rad,ext}}$ and $R_{\mathrm{rad,in}}$) and convective resistance ($R_{\mathrm{conv,ext}}$ and $R_{\mathrm{conv,in}}$) are considered at the interior surface of low-e film and the exterior surface of window glass, in series with the conductive resistance of solid window glass ($R_{\mathrm{cond,G}}$) and low-e polymer film ($R_{\mathrm{cond,Lowe}}$). Subscripts “in” and “ext” indicate interior and exterior, respectively; subscripts “cond”, “rad”, and “conv” indicate conduction, radiation, and convection, respectively.

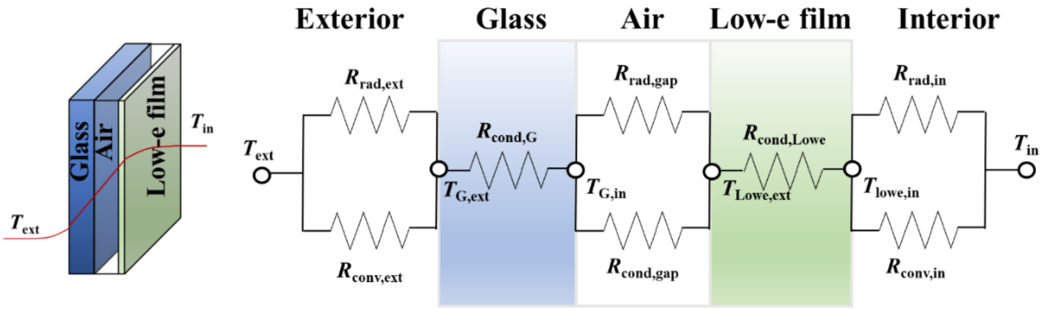

Figure 5.1 Schematic representation of the elevated low-e assembly (ELEA). The thermal nodes represent, from the left to right, T_{ext}: the exterior temperature, $T_{G,ext}$: the exterior temperature of window glass, $T_{G,in}$: the interior temperature of window glass, $T_{Lowe,ext}$: the exterior temperature of low-e film, $T_{Lowe,in}$: the interior temperature of low-e film, and T_{in}: the interior temperature.

Based on the Fourier's law [13], the conduction heat flux (q) in low-e film, air gap and glass is

$$q_{\mathrm{cond}} = -k\nabla T \tag{5.1}$$

where ∇T represents temperature gradient and k is the local thermal conductivity. The thermal resistance (R) can be expressed as the ratio of thickness (t_{G}, t_{gap}, t_{Lowe}) to thermal conductivity (k_{G}, k_{gap}, k_{Lowe}):

$$R_{\mathrm{cond}} = \frac{t}{k} \tag{5.2}$$

where t is the thickness of local component and subscripts "G", "gap" and "Lowe" indicate glass, air gap and low-e polymer film, respectively.

According to Kirchhoff's Law [20], the emissivity of each layer equals to its IR absorption, ε. The radiation thermal flux between two parallel surfaces is

$$q_{\text{rad,gap}} = \frac{\sigma\left({T_{\text{Lowe,ext}}}^4 - {T_{\text{G,in}}}^4\right)}{\frac{1}{\varepsilon_{\text{Lowe}}} + \frac{1}{\varepsilon_{\text{G}}} - 1} \tag{5.3}$$

where $\sigma = 5.67 \times 10^{-8}\ \text{W/m}^2 \cdot \text{K}^4$ is the Stefan Boltzmann constant. The radiation thermal resistance could be expressed as

$$R_{\text{rad,gap}} = \frac{T_{\text{Lowe,ext}} - T_{\text{G,in}}}{q_{\text{rad,gap}}} \tag{5.4}$$

Similarly, the radiation heat transfer and thermal resistance on the interior surface of low-e film can be written as:

$$q_{\text{rad,in}} = \varepsilon_{\text{Lowe}}\sigma\left({T_{\text{in}}}^4 - {T_{\text{Lowe,in}}}^4\right) \tag{5.5}$$

$$R_{\text{rad,in}} = \frac{T_{\text{in}} - T_{\text{Lowe,in}}}{q_{\text{rad,in}}} \tag{5.6}$$

The convective heat flux in the gap and at the interior surface of the low-e film is

$$q_{\text{conv}} = h_{\text{conv}} \nabla T \tag{5.7}$$

where h_{conv} is the thermal transfer coefficient of air convection in the gap or at a vertical surface. According to Churchill and Chu [14]:

$$R_{\text{conv,in}} = {h_{\text{conv,in}}}^{-1} = \frac{L}{Nu \cdot k_{\text{air}}} \tag{5.8}$$

where *Nu* is the mean Nusselt number and k_{air} is the thermal conductivity air phase and *L* is the surface height. *Nu* is a function of the Grashof number (Gr) and the Prandtl number (Pr). Pr is 0.70798 for air[15], and for free convection on the low-e surface, Gr is[16]

$$\mathrm{Gr} = \frac{g\beta dTL^3}{\nu^2} \tag{5.9}$$

where g is the gravitational constant (9.81 m/s^2), β is the thermal expansion coefficient, L is the sample height, ν is the dynamic viscosity of the air, and α is the air thermal diffusivity. Based on these values,

$$Nu = 0.68 + \frac{0.67\mathrm{Ra}^{1/4}}{\left[1+(0.492/\mathrm{Pr})^{9/16}\right]^{4/9}} \text{ for } \mathrm{Ra}_L \leq 10^9 \tag{5.10}$$

$$Nu = \left\{0.825 + \frac{0.387\mathrm{Ra}^{1/6}}{\left[1+(0.492/\mathrm{Pr})^{9/16}\right]^{8/27}}\right\}^2 \text{ for } 10^9 \leq \mathrm{Ra}_L \leq 10^{12} \tag{5.11}$$

where Ra is Rayleigh number and Ra=GrPr.

For the convective heat transfer in the enclosed air gap [16],

$$h_{\mathrm{conv,gap}} = \frac{t_{\mathrm{gap}}}{Nu \cdot k_{\mathrm{air}}} - h_{\mathrm{cond,gap}} \tag{5.12}$$

Nusselt number [16] can be obtained as,

$$Nu = \left[0.0605\mathrm{Ra}^{1/3}, \left(1 + \left[\frac{0.104\mathrm{Ra}^{0.293}}{1+(6310/\mathrm{Ra})^{1.36}}\right]^3\right)^{1/3}, 0.243\left(\frac{\mathrm{Ra}}{L/t}\right)^{0.272}\right]_{\max} \tag{5.13}$$

where Ra=GrPr and the Gr number [16] also can be calculated by Eq. (5.9), in which L=t_{gap}.

The heat transfer in Figure 5.1 should be in balance at the steady-state. Thus,

$$q_{\text{rad,ext}} + q_{\text{conv,ext}} = q_{\text{cond,G}} \tag{5.14}$$

$$= q_{\text{rad,gap}} + q_{\text{cond,gap}} + q_{\text{conv,gap}} = q_{\text{cond,Lowe}}$$

$$= q_{\text{rad,in}} + q_{\text{conv,in}}$$

Hence, the thermal transmittance (*U*) is:

$$U = \Big[R_{\text{ext}} + R_{\text{cond,G}} + \left({R_{\text{rad,gap}}}^{-1} + {R_{\text{cond,gap}}}^{-1} + {R_{\text{conv,gap}}}^{-1}\right)^{-1} \tag{5.15}$$

$$+ R_{\text{cond,Lowe}} + \left({R_{\text{rad,in}}}^{-1} + {R_{\text{conv,in}}}^{-1}\right)^{-1}\Big]^{-1}$$

According to ASTM C1199 and ASHRAE Handbook [14], the boundary condition is set as T_{ext} = 18 ℃ and T_{in} = 21 ℃, and the exterior heat transfer coefficient (h_{ext}) is 30 W/(m^2·K).

Eq.(5.2) implies that $R_{\text{cond,gap}}$ increases linearly with the air gap thickness. Eqs.(5.3) and (5.4) suggest that $R_{\text{rad,gap}}$ would be reduced, if the temperature difference across the air gap rises. Since t_{air} is very thin, ranging from 3 mm to 5 mm, based on Eq.(5.13), *Nu* is reduced to be almost 1, and $h_{\text{conv,in}}$ is lower than 0.1% of that of air conduction, which is negligible. The overall relationship between the ELEA thickness and $R_{\text{cond,gap}}$ and $R_{\text{rad,gap}}$ is illustrated in Figure 5.2(a). Because the heat resistance of air gap is $R_{\text{gap}} = \left({R_{\text{rad,gap}}}^{-1} + {R_{\text{cond,gap}}}^{-1}\right)^{-1}$and $R_{\text{cond,gap}}$ is much smaller than $R_{\text{rad,gap}}$, the heat flux in air gap mainly depends on $R_{\text{cond,gap}}$; the effect of $R_{\mathrm{rad,gap}}$ is secondary. Hence, a thicker air gap tends to improve the thermal resistance. Figure 5.2(b) demonstrates that, by decreasing the surface emissivity of the low-e film, $R_{\mathrm{rad,in}}$ is enhanced, which can overcome the slightly decrease of $R_{\mathrm{conv,in}}$ due to larger temperature difference between the low-e surface and the interior room temperature. Therefore, with a lower emissivity, the interior boundary heat resistance R_{in} is still much increased. Figure 5.2(c) shows the relationship among the *U*-factor, the total ELEA thickness, and the surface emissivity of low-e film. The low-e film thickness t_{Lowe}=500 μm; the glass thickness t_{G}=1 cm; the glass surface emissivity ε_{G}=0.84; the back-surface emissivity of low-e film is the same as that of polyethylene terephthalate (PET) substrate, $\varepsilon_{\mathrm{Lowe,ext}}$= 0.76. Clearly, increasing air gap thickness and reducing surface emissivity are beneficial. If the low-e film surface emissivity is ~0.1 and the air gap thickness is ~3.5 mm, the thermal transmittance (*U)* can be reduced to below 0.5 Btu/h·ft^2·°F.

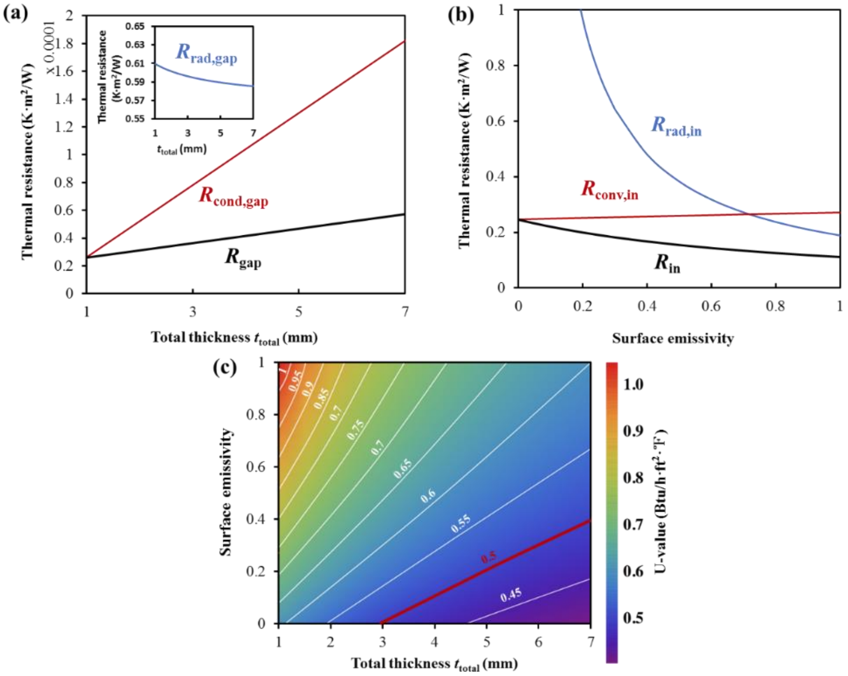

Figure 5.2 (a) The thermal conductive and the radiative resistance as functions of the total ELEA thickness ($\varepsilon_{\mathrm{Lowe,ext}}$= 0.76). (b) The convective and radiative resistance at interior surface of ELEA, as functions of the surface emissivity (t_{total}= 5 mm). (c) The value of U as a function of the total ELEA thickness (t_{total}) and the surface emissivity of low-e film ($\varepsilon_{\mathrm{Lowe}}$). The sample size L = 0.3048 m and the low-e film thickness t_{Lowe}= 500 µm.

5.3 Experimental procedure and results

ELEA samples were assembled by using 3M Thinsulate CC75 low-e films. A 500-µm-thick 0.3048 m by 0.3048 m large PET substrate was ultrasonically cleaned first in isopropyl alcohol (IPA) for 10 min and then in de-ionized (DI) water for 5 min. CC75 low-e film was firmly attached on the PET surface. The compound low-e layer was mounted on a 9.5-mm-thick 0.3556-mm-large glass pane by four 0.2794-m-long 12.7-mm-wide polycarbonate (PC) frame bars at the edges. The frame bar thickness ranged from 2.5 mm to 4.5 mm, which determined the thickness of the air gap between the low-e layer and the glass pane. The frame bars are affixed by adhesives (3M CA4) that cures at ambient temperature. Figure 5.3(a) ~(c) shows a typical sample.

Assembly and installation of ELEA structure to the real window may be relatively easy and fast, as shown in Figure 5.3(d). First, clean the window glass and measure its height and width. Second, section the frame bars and low-e film according to the dimension of the window. Then, attach the frame bars on window pane. Finally, mount the sectioned low-e layer on the frame bars.

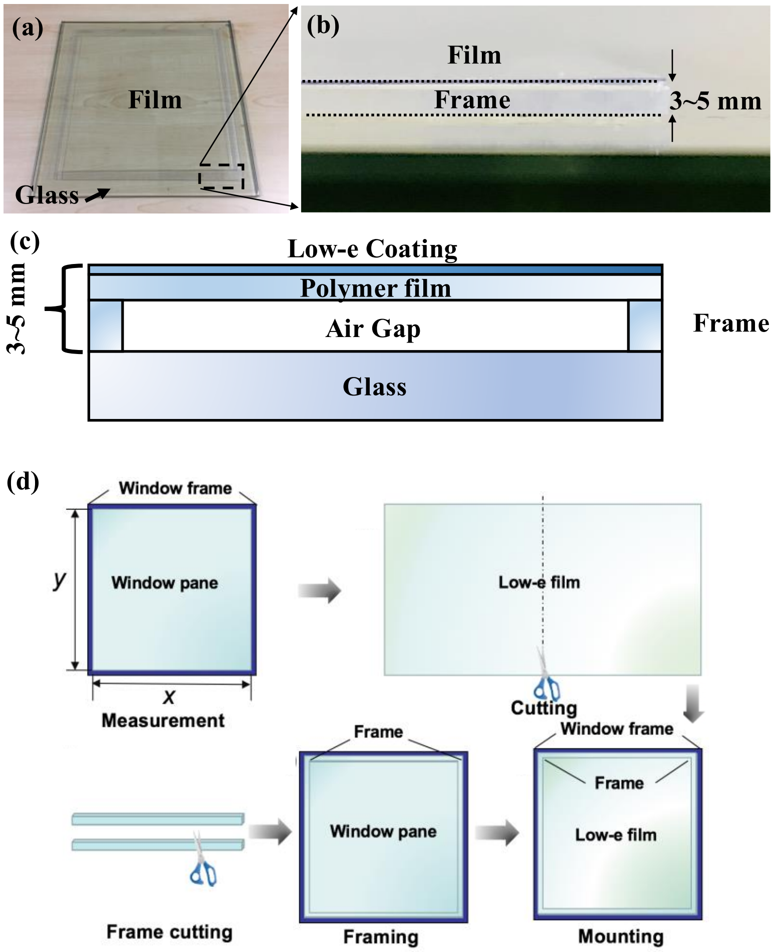

Figure 5.3 A typical ELEA sample: (a) top view, (b) side view, (c) a schematic and (d) the installation procedure

5.3.1 Thermal properties of ELEA

A thermal transmittance measurement system was fabricated, following ASTM C1199, ASTM C518, NFRC-100, and NFRC-102. As shown in Figure 5.4, inside a 0.39-m-long 0.47-m-wide 0.47-m-tall environmental chamber, T_{ext} was maintained at ~255 K. An ELEA sample was mounted at the opening of a side wall of the chamber.

The opening was 0.37-m by 0.37-m large. Four Omega K-type thermal couples were used to measure T_{ext}, T_{in}, the outer surface temperature of glass ($T_{\mathrm{G,ext}}$), and the inner surface temperature of low-e assembly ($T_{\mathrm{Lowe,in}}$). A gSKIN®-XI heat flux sensor was attached on the exterior surface of the ELEA. The temperature variation in the chamber was less than 1 °C. Ambient temperature (T_{in}) was ~294 K in all the tests.

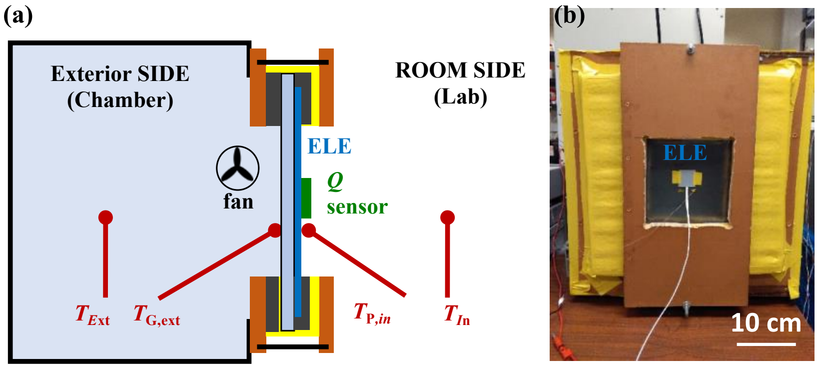

Figure 5.4 (a) Schematic and (b) a photo of the thermal transmittance measurement setup, with temperature being monitored by four thermocouples and the heat flux being measured by the *Q* sensor.

In our experiment, the exterior heat transfer coefficient was not a standard or constant value. The total thermal resistance was converted to *U* by adding standard boundary thermal transfer coefficients to the exterior ($h_{\mathrm{ST,ext}}$) and the interior ($h_{\mathrm{ST,in}}$). Based on ASTM C1199 and NFRC-100, $h_{\mathrm{ST,ext}}$ was set to 30 W/(m^2·K) and

$$h_{\mathrm{ST,in}} = 1.46\left[\frac{\left(T_{\mathrm{in}} - T_{\mathrm{Lowe,in}}\right)}{H}\right]^{0.25} + \sigma\varepsilon\left[\frac{(T_{\mathrm{in}} + 273.16)^4 - \left(T_{\mathrm{Lowe,in}} + 273.16\right)^4}{\left(T_{\mathrm{in}} - T_{\mathrm{Lowe,in}}\right)}\right] \tag{5.16}$$

where H is the sample height and $T_{\mathrm{Lowe,in}}$ and $T_{\mathrm{G,ext}}$ are respectively the measured temperatures at interior and exterior boundaries of ELEA. Consequently,

$$U = \left(\frac{1}{h_{\mathrm{ST,ext}}} + \frac{T_{\mathrm{Lowe,in}} - T_{\mathrm{G,ext}}}{q} + \frac{1}{h_{\mathrm{ST,in}}}\right)^{-1} \tag{5.17}$$

where q is the measured heat flux. The surface emissivity of low-e film and PET were taken as 0.14 and 0.76, respectively.

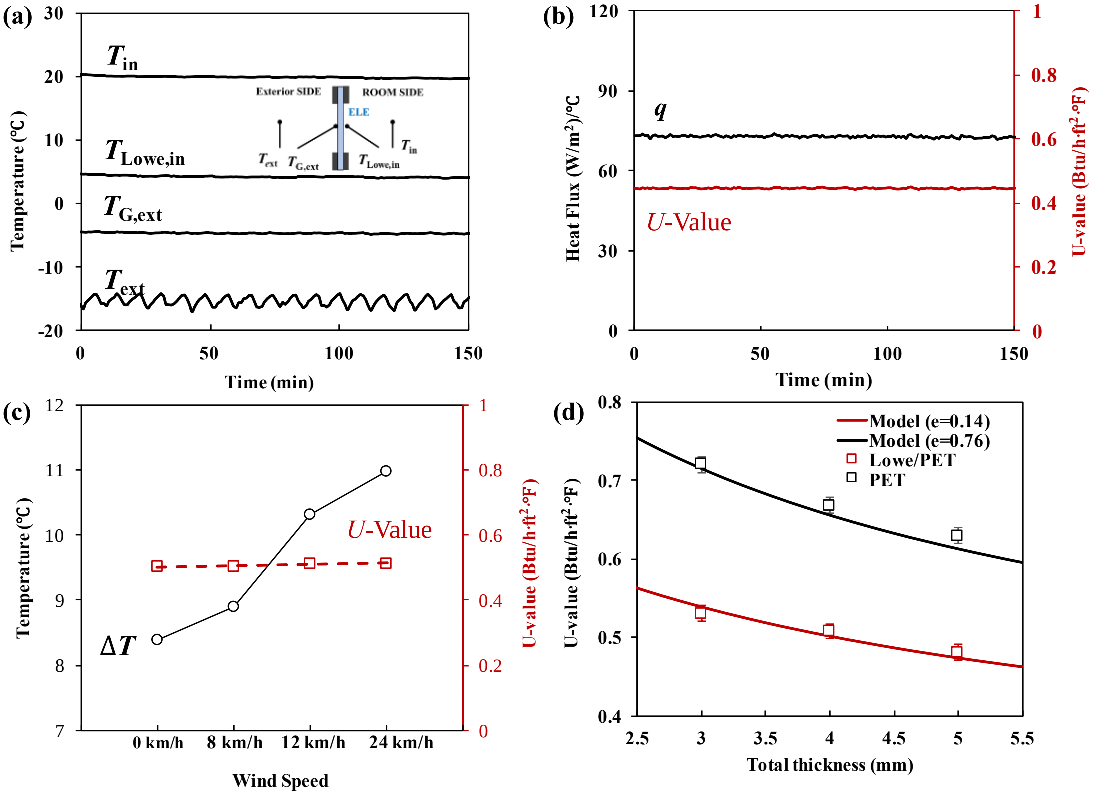

Figure 5.5 (a) T_{ext}, T_{in}, $T_{\text{G,ext}}$, and $T_{\text{Lowe,in}}$ and (b) the heat flux q and U at the steady state (t_{air}=4.5 ±0.1 mm). (c) The exterior wind speed effect on the temperature difference across ELEA and the U (t_{air}=3.5 ±0.1mm). (d) The relationship between the U and the total ELEA thickness.

Figure 5.5(a,b) show the measurement result of the temperatures and the heat flux of ab ELEA sample with the total thickness (t_{total}) of 5±0.1 mm. The thermal transmittance (U) is calculated by Eq. (5.17) to be ~0.445 Btu/h·ft^2·°F. Since the heat transfer coefficient is standardized, if the exterior heat transfer coefficient varies, the validated U should not be influenced. This is confirmed by controlling the wind speed in the environmental chamber, the temperature at the exterior side of glass pane ($T_{\text{G,ext}}$), and the temperature at the interior side of low-e film ($T_{\text{Low,in}}$). Figure 5.5(c) shows the measured temperature difference across and the validated U of an ELEA with t_{total} = 4±0.1 mm with various wind speeds. As the wind speed rises, the heat transfer coefficient becomes larger, so is the temperature difference across the sample, while the validated *U* keeps stable, as it should.

The aforementioned heat transfer model suggests that the air gap thickness (t_{gap}) and the surface emissivity are two vital factors for the U-factor. We tested ELEA samples with different t_{gap}; the PET substrates were either coated with CC75 low-e films (Lowe/PET) or pristine (PET). The results are summarized in Figure 5.5(d). The solid lines are numerical prediction. The thermal transmittance is much reduced when the surface emissivity of low-e film decreases from 0.76 (PET) to 0.14 (Lowe/PET) and when the air gap thickness increases. Clearly, a lower emissivity leads to a higher IR reflection, which blocks the irradiation heat loss; with a thicker air gap, thermal resistance is increased. A single glass pane typically has the *U* around 1.1 Btu/h·ft^2·°F [17], compared with which the *U* of ELEA mounted is considerably lower by nearly 50%.

As the thermal resistance was improved by ELEA, the water condensation resistance of the structure is significantly enhanced. We compared the temperature at the interior of ELEA assembly to the dew point (T_{dp}). The interior temperature (T_{in}) was standardized to be 294 K and the relative humidity (*RH*) was set to 30% and 50%. Other parameters are the same as the thermal modelling. The dew point is a function of air temperature (T_{in}) and *RH* [18]:

$$T_{\mathrm{dp}} = \frac{243.5\left(lnRH + \frac{17.67T_{\mathrm{in}}}{243.5+T_{\mathrm{in}}}\right)}{17.67 - lnRH - \frac{17.67T_{\mathrm{in}}}{243.5+T_{\mathrm{in}}}} \tag{5.18}$$

Under the testing condition (RH=30%) discussed in Section 5.3.1, the calculated dew point is 2.77 °C. If *RH* is increased to 50%, T_{dp}=11 °C. Figure 5.6 shows that compared with a window pane with directly coated low-e film, the ELEA can lower $T_{\mathrm{sur,in}}$ by 5~10 °C; with *RH* of 30% or 50%, the critical exterior temperature of water condensation is reduced by 7~10 °C and 3~5 °C, respectively.

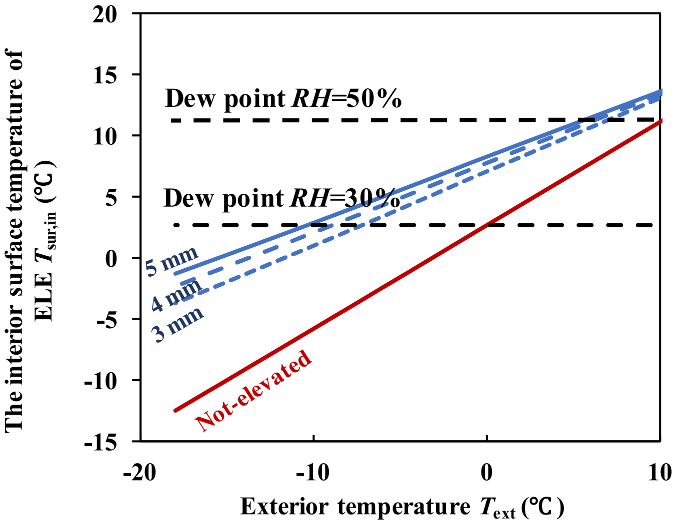

Figure 5.6 The relationship between the interior surface temperature and the exterior temperature. The total thickness of ELEA is 3 mm, 4 mm, or 5 mm. The dew point is calculated by Eq. (5.18), with the interior temperature being 21 °C and *RH* being 30% or 50%.

5.3.2 Optical Properties of ELEA

The visual transmittance and haze of ELEA were characterized by a JASCO V770 UV-VIS spectrometer, equipped by an integrating sphere, following ASTM D1003. An UV-Vis spectrophotometer was employed as the light source. The surface of the integrating sphere was coated with barium, and the signals collected by it were detected by a photomultiplier tube detector. The visible light transmission (V_T) was calculated by ASTM G173:

$$V_T = \frac{\int \tau(\lambda)E(\lambda)d\lambda}{\int E(\lambda)d\lambda} \tag{5.19}$$

where $E(\lambda)$ is the solar spectral irradiance.

The total light transmittance was evaluated by $\tau_t = \tau_2/\tau_1$, where τ_2 is the light transmitted through the sample and τ_1 is the incident light. With light scatter, we define $\tau_s = \tau_4 - \tau_3\tau_2/\tau_1$, where τ_3 is the instrument diffusion and τ_4 is the sample diffusion. The diffuse transmittance is measured by $\tau_d = \tau_s/\tau_1$. In our experiment, the incident light (τ_1) was measured with no ELEA sample mounted at the sample beam entrance aperture on the integrating sphere. A white standard was placed at the exit aperture. The light transmittance (τ_2) was measured by placing an ELEA sample at the sample beam entrance aperture, with everything else unchanged. The instrument diffusion was measured as the scattered light when the entrance and exit apertures were empty. The sample diffusion was measured with an ELEA sample at the sample beam entrance aperture and a white standard at the exist aperture. The haze value is defined as:

$$\text{Haze}= \tau_{\mathrm{d}}/\tau_{\mathrm{t}} = \tau_4/\tau_2 - \tau_3/\tau_{1.} \tag{5.20}$$

The transparency color perception ELEA was depicted using the CIE 1931 chromaticity diagram. The transmitted light was represented by the product of the ASTM G173 solar spectrum and the transmission spectrum of each sample. The CIE tristimulus values were obtained using a Type-1931 standard observer:

$$X = \int_{380}^{780} SPD(\lambda)\bar{x}(\lambda)d\lambda \tag{5.21}$$

$$Y = \int_{380}^{780} SPD(\lambda)\bar{y}(\lambda)d\lambda \tag{5.22}$$

$$Z = \int_{380}^{780} SPD(\lambda)\bar{z}(\lambda)d\lambda \tag{5.23}$$

where $\bar{x}(\lambda)$, $\bar{y}(\lambda)$, and $\bar{z}(\lambda)$ are the standard observer's color matching functions (CMFs) from ASTM E308 and *SPD* represents the spectral power distribution of the transmitted light. The CIE 1931 (x, y) chromaticity was calculated as

$$x = \frac{X}{X+Y+Z} \tag{5.24}$$

$$y = \frac{Y}{X+Y+Z} \tag{5.25}$$

The color rendering index (*CRI*) was obtained by averaging 8 standard test color samples (TCS), with the reflectance spectrum given in CIE-2004. Based on transmittance spectrum of low-e film and the reflectance spectrum of the TCS, the CIE

1931 (x, y) chromaticity of TCS was assessed under illumination and was converted into CIE-1964 color space. Finally, the color difference between the TCS illuminated by the light through the sample and by the reference white light source was computed, and

$$CRI = 100 - 4.6\Delta E_{\mathrm{uvw}}, \tag{5.26}$$

where ΔE_{uvw} is the color difference.

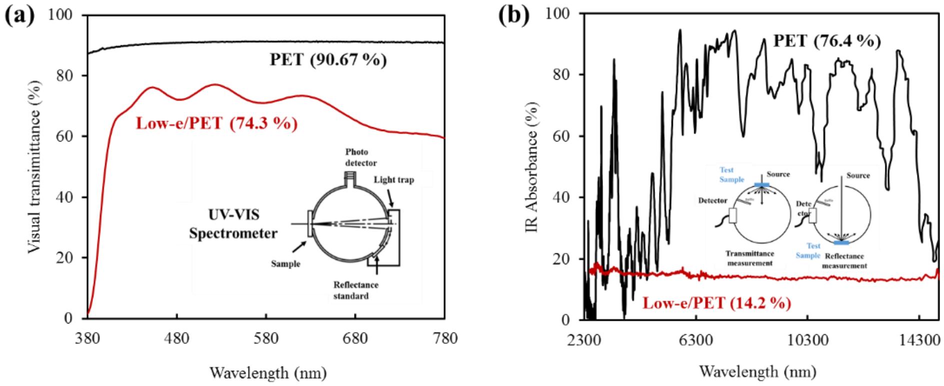

Figure 5.7 (a) V_T of PET and Low-e/PET layers. The inset shows the schematic of JASCO UV-VIS spectrometer with a 150-mm integrating sphere. (b) IR absorbance of PET and Low-e/PET layers. The insets are schematics of the FTIR spectrophotometer.

Table 5.1 Summary of the optical properties of PET

Optical properties		Pristine PET	CC75 coated PET
V_T (%)		90.7	74.3
Emissivity (%)		76.4	14.2
Haze (%)		0.2	1
CRI	Color coordinates	(0.339319, 0.352434)	(0.343153, 0.354865)
	CRI value	99.66	98.9

The measurement setup of emissivity consisted of a FTIR spectrophotometer with an integrating sphere attachment. FTIR spectrophotometer worked as the light source in the IR spectral region. The integrating sphere collected all the light transmitted or reflected by the sample, including both specular and diffuse transmittance or reflectance. It was coated with gold on the interior wall, which could scatter mid-IR light uniformly. Signals collected by the integrating sphere were detected by a MCT detector. This device could measure emissivity from 2300 nm to 15000 nm. Taking 1 as the total amount of energy in the incident IR light beam, at a certain temperature, the law of conservation of energy demands that $1 = \alpha' + \gamma + \tau$, where α' is the absorptivity, γ is the reflectance, and τ is the transmittance. As indicated by Kirchhoff's law, the emissivity of a surface equals to its absorptivity.

The procedure of IR transmittance measurement was similar to the measurement of V_T. For IR reflectance measurement, we put the sample at the reflectance port of the integrating sphere and let IR beam to go through the entrance port of the integrating sphere.

Figure 5.7(a) shows V_T of pristine PET film and low-e coated PET (lowe/PET) layers. The former is 90.7% and the latter is 74.3%. Although the low-e coating reduces V_T, the coating reflects more infrared light and can block the radiation energy dissipation. As shown in Figure 5.7(b), the low-e coating decreases the emissivity (equal to IR absorbance) from 76.4% to 14.2%. The haze values of these samples are shown in Table 5.1, both lower than 1%, suggesting that the low-e film does not induce much light scatter, superior to silica aerogels [19,20]. Table 5.1 also gives the color coordinates CIE 1931 (x,y) and CRI values. The color coordinates are located in the low colorfulness region in the CIE chromaticity diagram [21], indicating good achromatic or neutral color sensations when looking through the samples under standard white light source. The color rendering properties prove that the samples are capable of providing high-quality illumination with achromatic sensation.

5.3.3 Structural Integrity of ELEA

The structural integrity of 0.3048-m-large ELEA was evaluated through compression tests in a Type 5582 Instron machine, as shown in Figure 5.8. The PET layer thickness was 250 μm, 375 μm, or 500 μm. The air gap thickness was 3 mm. The crosshead speed was set to 0.01 mm/s and the total displacement was the same as the air gap thickness. Figure 5.8(a) indicates that the force needed to flatten an ELEA increases with the PET thickness, as it should.

Finite element analysis (FEA) was conducted with COMSOL Multiphysics, to quantitatively analyze the relationship between the compression force and the PET deflection. The polymer film was modeled with the same geometry and material as the testing sample, with linear elastic-plastic model; the Young's modulus was E = 2.4 Gpa; the Poisson's ratio was μ = 0.37; the mass density was 1190 kg/m^3. The compressive load was applied at the central 5-mm-radius circular area of the polymer film, the same as the size of the compression rod in the experiment. Rigid boundary condition was employed. Free triangular mesh was used, and the maximum and minimum element size were set to 610 μm and 61 μm, respectively. Geometric nonlinearity was taken into consideration. As shown by the solid lines in Figure 5.8(a), the numerical result matches well with the experimental data.

After repeated complete flattening, the hollow structure would be restored instantaneously as the loading was removed. Figure 5.8(b) shows the force-displacement curves of the first 10 cycles. A micrometer was used to monitor the thickness at the center point of the ELEA. More than 4000 cycles were applied, and no sign of degradation could be observed, as shown in Figure 5.8(c). Because of the large aspect ratio, even when the air gap is fully compressed, the maximum strain is only ~0.3%, order-of-magnitude smaller than the linear elastic limit (1.5-2% for most polymers [22,23]). That is, the ELEA configuration is deformable and resilient.

The ELEA sample was also constantly exposed to lab air (relative humidity: 50 to 60%), and the total thickness at the center point of the ELEA was monitored in about one year. As shown in Figure 5.8(d), the air gap in ELEA has a desirable long-term stability. Since the expectance life of low-e film is also 10 years and beyond and PET substrate has excellent long-term dimensional stability, the ELEA structure may be on active serve for more than 10 years.

To maximize the service life of ELEA, care should be taken not to scratch and tear the Low-e film. During the cleaning operation, users should try to avoid using a high pressure or any abrasive materials. Regular window cleaning solutions and clean synthetic sponge are recommended.

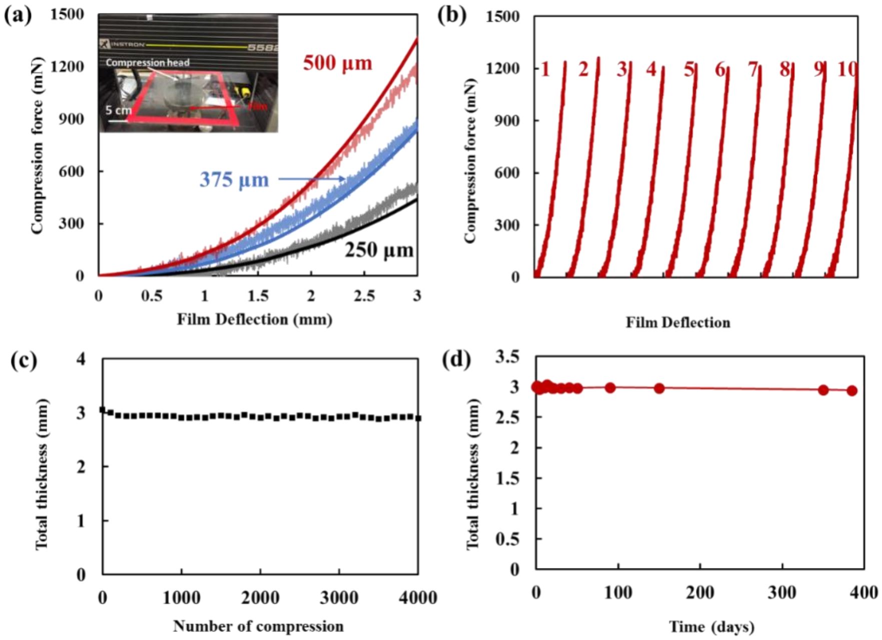

Figure 5.8 (a) Experimental and modelling results of compression of ELEA. The numbers indicate the PET substrate thickness; the inset is a photo of the compression testing setup. (b) Repeated flattening of ELEA for 10 cycles. (c) The stability of air gap thickness upon compression test; the cycle numbers are shown. (d) The stability of air gap over time.

5.4 Energy saving performance

To analyze the energy saving performance of ELEA installed single-pane, double-pane and triple-pane windows, their thermal transmittance can be calculated according to the model shown in section 5.2. In this analysis, we assume that the glass thickness is 1 cm, the gap in double-pane or triple-pane window is ½ inch, and the air thickness in ELEA is 5 mm. Other environmental parameters are the same as in ASTM C1199. The reduced heat flux through window can be evaluated by $q=(U_{\text{original}}-U_{\text{ELEA}})\Delta T$, where ΔT is the temperature difference between the interior and exterior sides. We assume that the service life (t_{service}) of ELEA is 10 years. As the heating energy price (p) in U.S. is taken as 0.1040 \$/kWh, the total energy saving can be assessed as qpt_{service}. As shown in Table 5.2, ELEA sis most cost-efficient for single-pane windows, since it can save ~1391 \$/m^2 in 10 years. If the total cost of installed ELEA is ~50/m^2, the recoup time is 4~5 months.

Table 5.2 Energy saving of ELEA

	Original U (W·m-2·K-1)	U (with ELEA) (W·m-2·K-1)	Reduced heat flux (W/m2)	Heat energy cost ($/kWh)	Money saving in 10 years ($/m2)
Single-Pane	6.60	2.69	152.5	0.1040	1390.7
Double-Pane	2.92	1.62	50.7		463.6
Triple-Pane	1.66	1.18	18.7		171.6

5.5 Concluding Remarks

In summary, we investigate a simple and cost-efficient installation approach of low-e films. The low-e film is attached to a transparent polymer substrate and mounted on glass pane with frame bars. The polymer layer and the glass pane are separated by a 3~5 mm thick air gap. Such an elevated low-e assembly (ELEA) can have a low thermal transmittance (U) less than 0.5 Btu/h·ft^2·°F, due to the reduction in conductive and radiative heat transfer. The U-factor can be further improved if the air gap thickness is increased and/or the emissivity is reduced. The visual transmittance and haze of ELEA are >70% and <2%, respectively, satisfactory for the window pane retrofitting applications. The hollow structure helps mitigate water condensation, by increasing the inner surface temperature and suppressing heat conduction of water layer. The installation of ELEA is fast and does not require processional skills. ELEA is flexible and resilient. Repeated flattening does not induce evident structural degradation. We envision that the ELEA design can not only be applied to present-day low-e films, but also be adaptive to future window coating materials, such as advanced silica aerogels and polymer aerogels.

Acknowledge

Chapter 5, in part, is a reprint of the material as it appears in Energy and Buildings. Rui Kou, Ying Zhong, Jeongmin Kim, Qingyang Wang, Meng Wang, Renkun Chen and Yu Qiao. Elevating low-emissivity film for lower thermal transmittance. 193, pp.69-77. The dissertation author was the primary investigator and first author of the paper.

References

[1] US Department of Energy, Research and Development Roadmap for Emerging HVAC Technologies, US Dep. Energy, Build. Technol. Off. Washington, DC. (2014) 121.

[2] J. Carmody, S. Selkowitz, E. Lee, D. Arasteh, T. Willmert, Window System for High-Performance Buildings, (2004).

[3] U.S. DoE, Buildings energy databook, Energy Effic. Renew. Energy Dep. (2011).

[4] How Much Does Window Replacement Cost? | Angie's List, (2015).

[5] Single -Pan Highly Insulating Efficient Lucid Designs (SHIELD) Program Overview, (2014) 1–13.

[6] U. Berardi, Stakeholders' influence on the adoption of energy-saving technologies in Italian homes, Energy Policy. 60 (2013) 520–530.

[7] B.P. Jelle, A. Hynd, A. Gustavsen, D. Arasteh, H. Goudey, R. Hart, Fenestration of today and tomorrow: A state-of-the-art review and future research opportunities, Sol. Energy Mater. Sol. Cells. 96 (2012) 1–28.

[8] A. Kaklauskas, E.K. Zavadskas, S. Raslanas, R. Ginevicius, A. Komka, P. Malinauskas, Selection of low-e windows in retrofit of public buildings by applying multiple criteria method COPRAS: A Lithuanian case, Energy Build. 38 (2006) 454–462.

[9] C. Schaefer, G. Bräuer, J. Szczyrbowski, Low emissivity coatings on architectural glass, Surf. Coatings Technol. 93 (1997) 37–45.

[10] R.J. Martın-Palma, L. Vazquez, J.M. Martınez-Duart, Silver-based low-emissivity coatings for architectural windows: Optical and structural properties, Sol. Energy Mater. Sol. Cells. 53 (1998) 55–66.

[11] Single -Pane Highly Insulating Efficient Lucid Designs (SHIELD) Program Overview, (2014) 1–13.

[12] J.L. Wright, A correlation to quantify convective heat transfer between vertical window glazings, ASHRAE Trans. 102 (1996).

[13] T.L. Bergman, F.P. Incropera, D.P. DeWitt, A.S. Lavine, Fundamentals of heat and mass transfer, John Wiley & Sons, 2011.

[14] A. Handbook, Fundamentals, Am. Soc. Heating, Refrig. Air Cond. Eng. Atlanta. 111 (2001).

[15] F.M. White, I. Corfield, Viscous fluid flow, McGraw-Hill New York, 2006.

[16] A. Bejan, Convection heat transfer, John wiley & sons, 2013.

[17] J. Carmody, S. Selkowitz, D. Arasteh, L. Heschong, Residential windows: a guide to new technologies and energy performance, WW Norton & Company, 2007.

[18] D. Bolton, D. Bolton, The Computation of Equivalent Potential Temperature, Mon. Weather Rev. 108 (1980) 1046–1053.

[19] M.A. Aegerter, N. Leventis, M.M. Koebel, Aerogels handbook, Springer Science & Business Media, 2011.

[20] A.C.P. and, ‡ Gérard M. Pajonk*, Chemistry of Aerogels and Their Applications, (2002). doi:10.1021/CR0101306.

[21] T. Smith, J. Guild, The CIE colorimetric standards and their use, Trans. Opt. Soc. 33 (1931) 73.

[22] D.R.H. Jones, M.F. Ashby, Engineering materials 2: an introduction to microstructures and processing, Butterworth-Heinemann, 2012.

[23] K.K. Chawla, M.A. Meyers, Mechanical behavior of materials, Prentice Hall Upper Saddle River, 1999.

Chapter 6 Improving Visual Transmittance by Anti-Reflection Coating

6.1 Introduction

In Chapters 2-5, we presented our work on the polymer-air multilayer (PAM) technique [8,10], as shown in Figure 6.1. PAM can simultaneously reduce conductive and radiative heat transport. It contains multiple polymer layers separated by air gaps, with spacers on the edges. The outer polymer layer can be coated by a low-e film. The layer separation is ensured by in-plane tension, and enhanced by polymer electrification [10,11]. Under a compressive loading the layers may be flattened, but upon unloading the hollow structure can be self-restored. The air gaps offer low thermal conductivity ~0.026 W/(m·K).

One issue of PAM is that, it uses polymer films that have relatively high refractive index. For instance, the refractive index of polyethylene terephthalate (PET) is 1.58 [12]. Because each PET layer would reflect a certain portion of incident visible light, the overall visual transmittance may be low if the layer count is too large. Some other transparent polymers, such as polydimethylsiloxane (PDMS) and polytetrafluoroethylene (PTFE), have lower refractive indexes (1.41 and 1.35, respectively for PDMS and PTFE) [12]. However, their mechanical properties, especially the long-term stability, are poor. Poly(methyl methacrylate) (PMMA) is clear, strong, and stable. Its refractive index is 1.49. Yet, PMMA films thinner than 200 μm are expensive and often unavailable. In view of these considerations, in the current chapter, anti-refraction (AR) techniques will be investigated. The study is focused on PET films, the top candidate of polymer films used in the previous chapters. With the optical properties, compatibility with PET, and the cost-performance balance being taken into consideration, the candidates of AR coating material are chosen to be PMMA and PDMS.

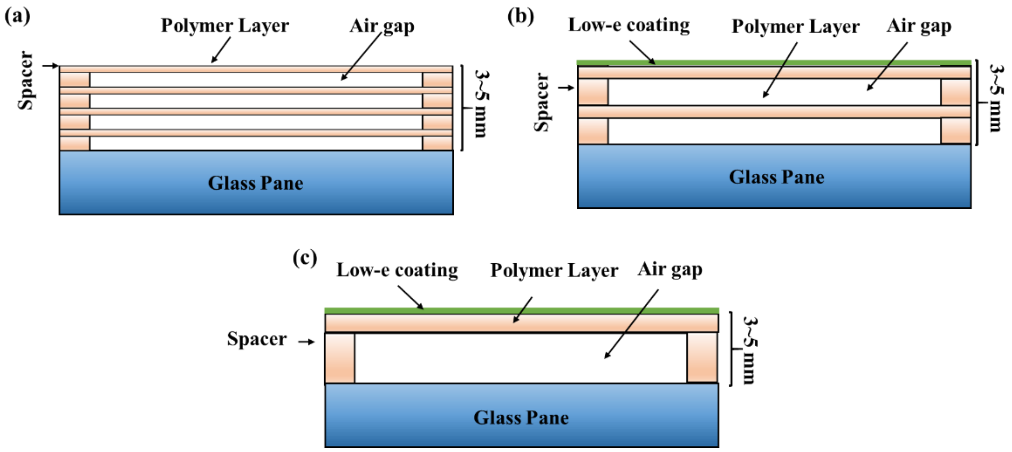

Figure 6.1 A schematics of a) 4-Layer polymer-air multilayer (PAM), b) 2-Layer PAM, and c) 1-Layer low-e PAM.

6.2 Experimental

6.2.1 Materials preparation

125-μm-thick PET films were obtained from McMaster-Carr (Product No. 8567K52), and squared with dimensions of 20×20 mm. They were ultrasonically cleaned in acetone for 10 min, and in de-ionized (DI) water for 5 min. The PET films were then dried in vacuum at 60 °C for 24 hr, followed by plasma treatment for 1 min in the corona charging system discussed in Chapter 2. The corona treatment was conducted at room temperature, with the needle voltage of 20 kV and the grid voltage of 2 kV. The needle height was 4 cm, and the grid height was 1 cm.

The PMMA source was an A2 resist solution obtained from MicroChem Corp; the PMMA concentration was 2 wt%, and the solvent was chlorobenzene. The PDMS source was a 2 wt% hexane solution. The PDMS base (Sylgard 184, Dow Corning Corporation) was mixed with its curing agent with the mass ratio of 10/1 in a Thinky Mixer at 1500 rpm for 3 min, and subsequently ultrasonically dissolved in hexane (Aldrich chemicals, CAS Number: 110-54-3) for 5 min.

6.2.2 Spin coating and dip coating

Two AR coating methods were investigated: spin coating and dip coating. Laurel Spin Coater was employed for the spin coating. A PET film was mounted on the spin vacuum chunk at the center. Spin coating began with depositing the solution dropwise onto the PET surface. After the resist covered the PET film completely, the spin coater was turned on. The spinning rate ranged from 2000 rpm to 3000 rmp; the duration was 60 seconds. For PMMA coating, the coated PET film was rested at 80 ℃ for 90 seconds; for PDMS, the PET film was heated at 100 ℃ for 20 min. The sample was cooled down in ambient area. For some samples, the same procedure was repeated for the other side of the PET films.

Dip coating was performed by immersing the cleaned PET film into the PMMA or PDMS solution. The film was attached to the loading grip of a type-5582 Instron machine by duct tapes, and lowered into the container of the PMMA/PDMS solution for 60 sec. Then, the film was pulled out at a constant rate of 4 mm/s, dried for 20 min in ambient air, and cured at 80 °C for 90 seconds for the PMMA coating or at 100 °C for 10 min for the PDMS coating.

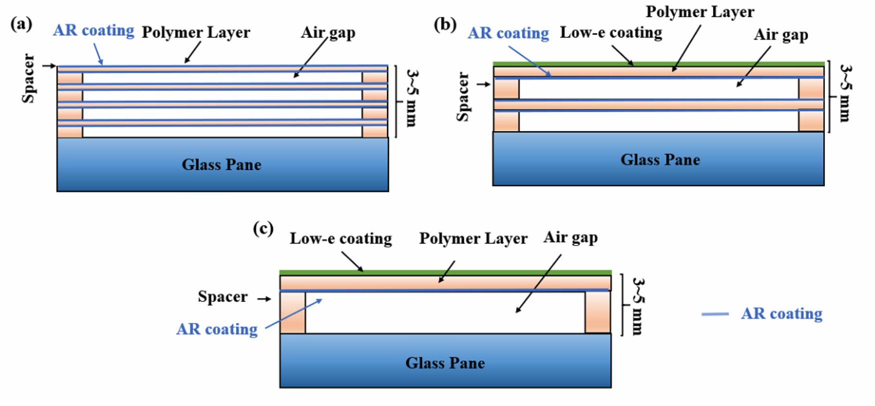

Figure 6.2 Schematics of AR coated a) 4-layer PAM, b) 2-layer PAM and c) 1-layer PAM.

6.2.3 PAM assembling

The AR coated 125-µm-thick PET films were cut into 20×20 mm large square pieces. A PAM sample was formed by *N* layers of the films with *N* sets of spacers at the edges in between adjacent layers. The spacers were made of 3-mm-wide 500-µm-thick polycarbonate bars (McMaster Product No. 85585K15). The layer count (*N*) was either 1, 2, or 4. For some 1-layer and 2-layer PAM samples, 3M Thinsulate CC75 low-e films were firmed attached to the outer surfaces of the AR coated PET films. The spacers were adhered by 3M CA5 epoxy adhesive, cured at room temperature for 1 day. Figure 6.2 depicts the configurations of the 4-layer, 2-layer, and 1-layer PAM samples.

6.2.4 Measurement of optical properties

The visual transmittance and haze of the polymer films and the PAM samples were characterized by a JASCO V770 UV-VIS spectrometer, equipped with an integrating sphere, following ASTM D1003. An UV-Vis spectrophotometer was employed as the light source. The spectral ranges from 380 nm to 750 nm. To measure the visual transmission, samples were placed in front of the light entrance port of the integrating sphere. The visible light transmission (V_T) was defined by ASTM G173 as

$$V_T = \frac{\int \tau(\lambda)E(\lambda)d\lambda}{\int E(\lambda)d\lambda} \tag{6.1}$$

where $E(\lambda)$ is the solar spectral irradiance, $\tau(\lambda)$ is the light transmission at certain wavelength. Following ASTM D1003, haze can be calculated as:

$$\text{Haze}= \tau_4/\tau_2 - \tau_3/\tau_1 \tag{6.2}$$

among which τ_2 is the light transmitted through the sample, τ_1 is the incident light, τ_3 is the instrument diffusion, and τ_4 is the sample diffusion. The detailed procedure was similar to the V_T and haze measurement in previous chapters.

6.3 Numerical modeling

The visual transmission model for PAM was based on the EnergyPlus 8.5 [13], developed by the Department of Energy as a standard building energy simulation tool.

Consider N layer of polymer films, as shown in Figure 6.3. $T_{i,j}$ indicates the visual transmittance through polymer layer i to j; $R^f_{i,j}$ and $R^b_{i,j}$ indicate the front and the back visual reflectance from polymer layer i to j, respectively. Layer 1 is the outer layer and layer N is the inner layer. These relations account for multiple internal reflections of the polymer films. The optical properties are dominated by the following recursion relations of $T_{i,j}$:

$$T_{i,j} = \frac{T_{i,j-1}T_{j,j}}{1 - R^f_{j,j}R^b_{j-1,j}} \tag{6.3}$$

$$R^f_{i,j} = R^f_{i,j-1} + \frac{T^2_{i,j-1}R^f_{j,j}}{1 - R^f_{j,j}R^b_{j-1,i}} \tag{6.4}$$

$$R^b_{j,i} = R^b_{j,j} + \frac{T^2_{j,j}R^b_{j-1,i}}{1 - R^b_{j-1,i}R^f_{j,j}} \tag{6.5}$$

where $T_{i,j} = 1$ and $R_{i,j} = 0$, if $i<0$ or $j>N$.

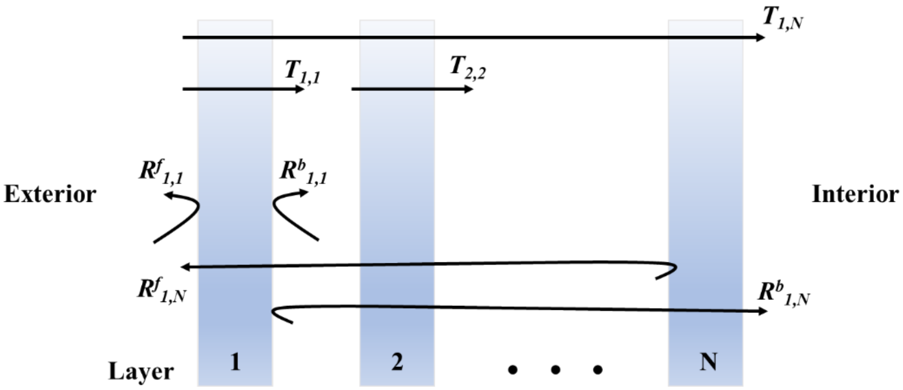

Figure 6.3 Schematic of visual transmission and reflection in a PAM

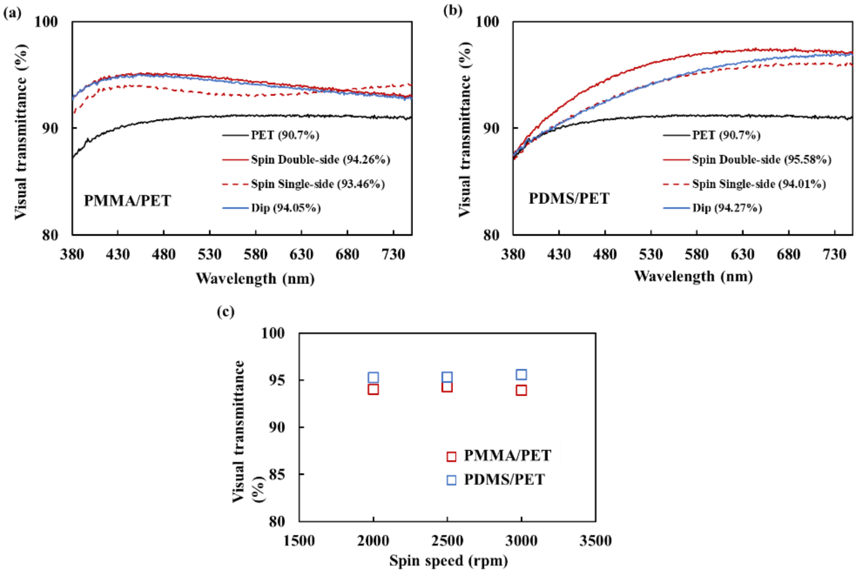

Figure 6.4 UV-Vis-NIR transmission spectra of: a) PMMA single-side spin coated, double-side spin coated, and dip coated PET films (the spin rate is 2500 rpm); and b) PDMS single-side spin coated, double-side spin coated, and dip coated PET films (the spin rate is 3000 rpm). c) The spin rate effect on V_T of PMMA and PDMS coated PET films.

6.4 Results and discussion

Anti-reflection (AR) coatings of PMMA and PDMS were applied on the PET films to decrease the visual reflection and to increase the light transmission. Figure 6.4 shows the UV-Vis-NIR spectra of pristine and PMMA/PDMS coated PET films in the wavelength range of 380-750 nm, with the weighted average V_T value for each sample being shown in the legend. Pristine PET had a V_T of 90.7%. With desirably low refractive indexes, PMMA coating and PDMS coating increased V_T to 94.26% and 95.58%, respectively. In the figure, “PMMA/PET” and “PDMS/PET” indicate PMMA and PDMS coated PET films, respectively. Moreover, double-sided coating increased

V_T more than single-sided coating. For example, V_T of PMMA double-sidedly coated PET (94.26%) is 0.8% higher than that of the single-side coated sample (93.46%).

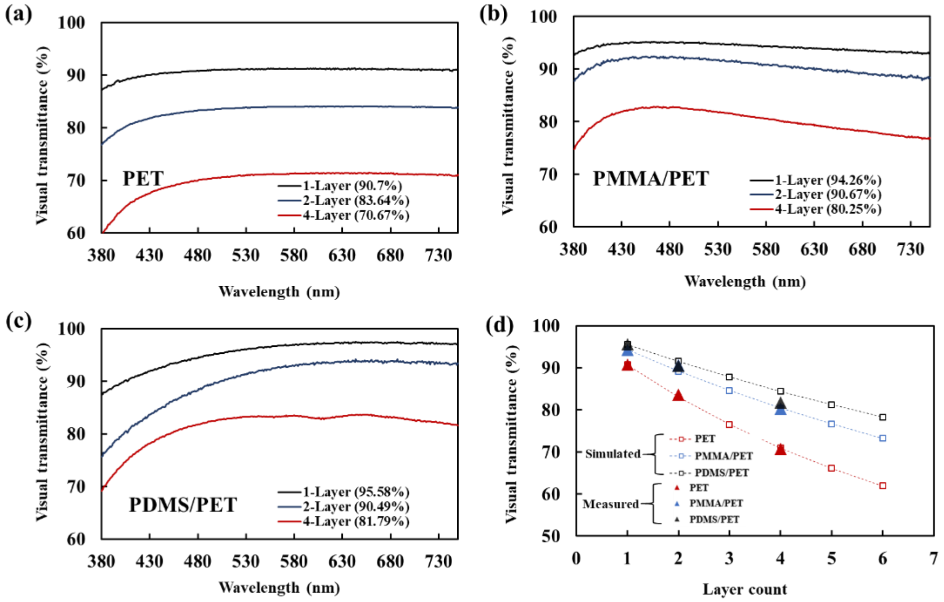

Figure 6.5 UV-Vis-NIR transmission spectra of 1-layer, 2-layer and 4-layer of a) pristine PET films; b) PMMA double-side coated PAM (the spin speed is 2500 rpm); and c) PDMS double-side coated PAM (the spin speed is 3000 rpm). (d) The simulation and the measurement results of the effects of layer count on the visual transmittance.

The spin speed in spin coating would affect the final coating thickness. However, it did not have any significantly influence on the V_T values, as illustrated in Figure 6.4(c). Clearly, the critical factor of the AR coating was the reduced difference in the indexes of refraction between solid and air, and the coating thickness effect was secondary.

The V_T values of PMMA and PDMS dip-coated PET films could also reach 94.05% and 94.27%, respectively, quite close to the effects of spin coating. Because the vital parameter is the refractive index of the coating material, not the coating thickness, even when the dip-coated surface layer is thicker, the final V_T is similar. Since dip coating is faster, lower cost, and able to simultaneously handle both sides of the PET films, it is preferred for mass manufacturing.

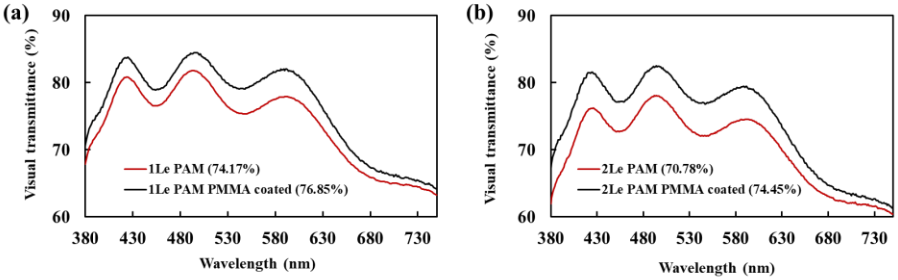

Figure 6.6 UV-Vis-NIR transmission spectra of a) uncoated and PMMA coated 1-layer PAM and b) uncoated and PMMA coated 2-layer PAM. The spin speed of PMMA coating is 2500 rpm.

Figure 6.5(a-c) are UV-Vis-NIR spectra of 1-layer (1L), 2-layer (2L), and 4-layer (4L) PAM constructed by uncoated and PMMA and PDMS double-sidely coated PET films. Figure 6.5(d) compares the simulated and measured V_T of PAM with different layer counts. The V_T measurement data fit well with the model prediction. With an increasing layer count, V_t would be reduced. With the PMMA or PDMS coating, V_T of 4L PAM can be enhanced to 80.25% and 81.79%, respectively.

Figure 6.6(a,b) are UV-Vis-NIR spectra of uncoated and PMMA coated 1L and 2L PAM with low-e coatings. It can be seen that the PMMA coating significantly increases V_T by 2.8% to 3.7%.

Table 6.1 Haze of uncoated, PDMS coated, and PMMA coated PAM (%)

	Uncoated	PDMS coated	PMMA coated
1-Layer PAM	0.2	1.1	0.2
4-Layer PAM	0.8	4.3	1

Table 6.2 Haze of uncoated and PMMA coated 1L and 2L PAM, with low-e coating (%)

	Pristine	PMMA coated
1L PAM	0.6	0.6
2L PAM	0.8	0.8

Table 6.1 shows the haze measurement results of uncoated and PDMS and PMMA coated 1L and 4L PAM (without low-e coating). PMMA coating does not increase the haze, suggesting there is little additional light scatter. PDMS coating increases the haze from 0.2 to 1.1 for 1-layer PAM; for 4-Layer PAM, haze is raised to 4.3, exceeding the window application requirement (2%). The high haze of PDMS coating should be associated with the relatively poor adhesion between PDMS and PET,

which causes microscopic scale markings and wrinkles. Table 6.2 summarizes the haze measurement results of uncoated and PMMA coated 1L and 2L PAM (with low-e coating). Again, the PMMA coatings do not affect haze.

6.5 Conclusion

In summary, to improve the overall visual transmittance, we investigated the AR coating technique using PMMA and PDMS. AR layer can be coated through either spin coating or dip coating. Because the coating thickness is a secondary factor, the two methods lead to similar AR effects. As dip coating is faster and lower cost, it may be the preferred choice for mass manufacturing. Between PMMA and PDMS, PMMA is better. Although PDMS coating improved V_T slightly more than PMMA, it also considerably increased haze, due to the relatively weak PDMS-PET bonding. Both model prediction and experimental data suggested with increasing the layer count, V_T would be reduced. However, with PMMA coating, V_T of 4-layer PAM could still reach 80.3%. If low-e layer was applied, for 1-layer PAM and 2-layer PAM, V_T was 76.9% and 74.5%, respectively. All of these visual transmittance values exceeded the building window applications (70%). Hazes of 4-layer, 2-layer and 1-layer PAM were respectively 1%, 0.8%, and 0.6%, satisfactory to the window-pane retrofitting requirement (2%).

Acknowledge

Chapter 6, in part, is currently being prepared to be submitted for publication. Rui Kou, Ying Zhong, Qingyang Wang, Yun Zhou, Renkun Chen and Yu Qiao. The dissertation author was the primary investigator and first author of the paper.

References

[1] T. Gao, B.P. Jelle, T. Ihara, A. Gustavsen, Insulating glazing units with silica aerogel granules: The impact of particle size, Appl. Energy. 128 (2014) 27–34.

[2] H. Maleki, L. Durães, A. Portugal, An overview on silica aerogels synthesis and different mechanical reinforcing strategies, J. Non. Cryst. Solids. 385 (2014) 55–74.

[3] R.P. Patel, N.S. Purohit, A.M. Suthar, An overview of silica aerogels, Int. J. ChemTech Res. 1 (2009) 1052–1057.

[4] Y.-L. He, T. Xie, Advances of thermal conductivity models of nanoscale silica aerogel insulation material, Appl. Therm. Eng. 81 (2015) 28–50.

[5] J. FRICKE, E. Hümmer, H.-J. Morper, P. Scheuerpflug, Thermal properties of silica aerogels, Le J. Phys. Colloq. 50 (1989) C4-87.

[6] C. Schaefer, G. Bräuer, J. Szczyrbowski, Low emissivity coatings on architectural glass, Surf. Coatings Technol. 93 (1997) 37–45.

[7] R.J. Martın-Palma, L. Vazquez, J.M. Martınez-Duart, Silver-based low-emissivity coatings for architectural windows: Optical and structural properties, Sol. Energy Mater. Sol. Cells. 53 (1998) 55–66.

[8] R. Kou, Y. Zhong, J. Kim, Q. Wang, M. Wang, R. Chen, Y. Qiao, Elevating low-emissivity film for lower thermal transmittance, Energy Build. 193 (2019) 69–77.

[9] E. Ando, M. Miyazaki, Moisture degradation mechanism of silver-based low-emissivity coatings, Thin Solid Films. 351 (1999) 308–312.

[10] R. Kou, Y. Zhong, Y. Qiao, Effects of anion size on flow electrification of polycarbonate and polyethylene terephthalate, Appl. Phys. Lett. 115 (2019) 73704.

[11] Y. Zhong, R. Kou, M. Wang, Y. Qiao, Electrification Mechanism of Corona Charged Organic Electrets, J. Phys. D. Appl. Phys. (2019).

[12] S. Bäumer, Handbook of plastic optics, Wiley Online Library, 2010.

[13] V.A.C. da Costa, V.F. Roriz, K.M.S. Chvatal, Modeling of slab-on-grade heat transfer in nergyPlus simulation program, Ambient. Construído. 17 (2017) 117–135.

Chapter 7 Conclusion and Future Work

7.1 Conclusion

A low-cost, resilient, and transparent retrofitting technique of single-pane windows, polymer-air multilayer (PAM), was developed and characterized. PAM comprises one to four polyethylene terephthalate (PET) layers fully separated by air gaps. The layer separation is achieved through in-plane tension and assisted by polymer electrification. All of the conductive, convective, and radiative heat transport are reduced by PAM. To further improve the radiative heat resistance, a low-emissivity (low-e) film can be coated on the outer polymer layer. Our study is mainly focused on three types of PAM: 1-layer low-e (1L) PAM, 2-layer low-e (2L) PAM, and 4-layer (4L) PAM. The overall visual transmittance of PAM can be enhanced by anti-reflection (AR) coating, through either spin coating or dip coating. As summarized in Table 7.1, the visual transmittance (V_T) of 4L PAM can reach 80.3%; V_T of 1L and 2L PAM can reach 76.9% and 74.5%, respectively. Haze of 1L, 2L and 4L PAM is 0.6%, 0.8% and 1%, respectively. The color render index of them is 97.74%, 95.55% and 94.43%, respectively. A 4-mm-thick 1L PAM, 3-mm-thick 2L PAM, or a 6-mm-thick 4L PAM can reduce the U-factor to around 0.5 $\mathrm{Btu \cdot h^{-1} \cdot ft^{-2} \cdot {}^{\circ}F^{-1}}$, which nearly halves the energy compared to a regular single-pane window. PAM is flexible and resilient. There is no sign of degradation upon loading-unloading for over 4000 cycles, or exposure to lab air for 1 year.

Table 7.1 Summary of *U*-factor and optical properties of PAMs

	1-Layer low-e (1L)	2-Layer low-e (2L)	4-Layer (4L)
U-factor ($\mathrm{Btu \cdot h^{-1} \cdot ft^{-2} \cdot {}^{\circ}F^{-1}}$)	0.507	0.510	0.501
V_{T} (%)	76.85	74.45	81.79
Haze	0.6	0.8	1
CRI（%）	97.74	95.55	94.43
Thickness (mm)	4	3	6

7.2 Future work

The effective thermal conductivity of PAM, k_{PAM}, can be modeled as a series of thermal resistors of polymer and air layers:

$$k_{\mathrm{PAM}} = \left(\frac{t_{\mathrm{a}}}{k_{air,eff}} + \frac{t_{\mathrm{p}}}{k_{\mathrm{p}}}\right)^{-1}(t_{\mathrm{a}} + t_{\mathrm{p}}) \tag{7.1}$$

where k_{p} is the thermal conductivity of polymer, typically 0.2~0.4 $\mathrm{W \cdot m^{-1} \cdot K^{-1}}$ [1]; t_{a} and t_{p} are the thicknesses of air gap and polymer films, respectively. $k_{\mathrm{air,eff}}$ is related to the air gap thickness, which can expressed by [2]:

$$k_{\mathrm{air,eff}} = \frac{15\rho(2RT_0)^{3/2}b}{16D + 28\sqrt{\pi}} \tag{7.2}$$

where ρ is the air density, R is the gas constant, T_0 is the average temperature, b is air gap thickness, and D is the inverse Knudsen number. We envision that if the air gap can be reduced to below 200 nm, the air thermal conductivity can be much lowered. Such a nanometer scale PAM may be referred to as nanoPAM. The effective thermal conductivity of nanoPAM is shown in Figure 7.1. For micro-sized PAM, $k_{air,\mathrm{eff}}$ is in the range from 0.026~0.03 W·m^{-1}·K^{-1}. For nanoPAM, $k_{air,\mathrm{eff}}$ can be lower than 0.02 W·m^{-1}·K^{-1}. According to Eq. 3.18, the U-factor of PAM highly depends on its thermal conductivity. Thus, nanoPAM may offer much improved thermal insulating properties than microscopic PAM.

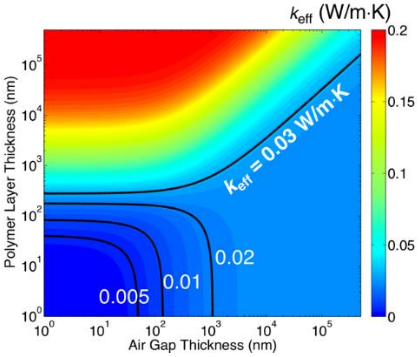

Figure 7.1 Contour plot of the thermal conductivity of PAM.

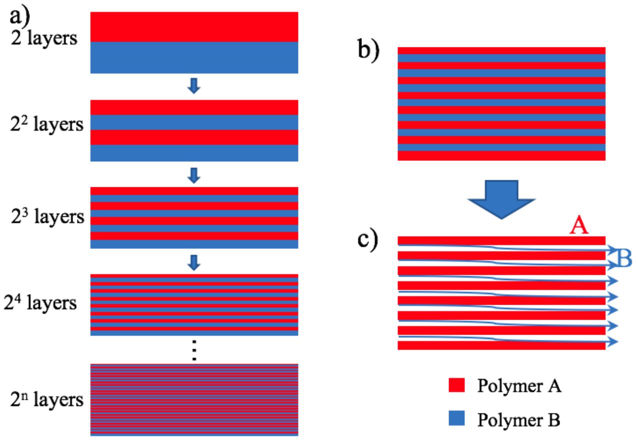

Figure 7.2 manufacturing process of nanoPAM. a) Coextrusion. b) A nano-alternating-layers made of polymers A and B. c) Removal of polymer B.

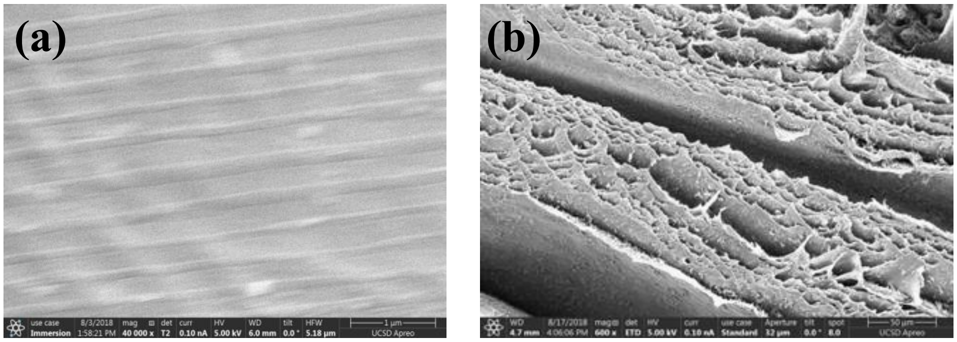

Figure 7.3 SEM photos of a) a PA/PC nano-alternating-layers (with the layer thickness of 400 nm/500 nm) and b) a PA nanoPAM

We have investigated nanoPAM processing, as sketched in Figure 7.2. The coextrusion system at PolymerPlus (Valley View, Ohio) was employed to manufacture nano-alternating-layers. Polyamide (Ultramide B36) and polycarbonate (Makronlon 2407) were selected as the layer materials. They were coextruded together at 250 ℃ to form 1024 layers of PA/PC nano-alternating-layers, with the layer thickness around

400-500 nm. PA is chemically resisted to chloroform, while PC can be dissolved in chloroform. Thus, we used chloroform (CAS Number: 67-66-3) to rinse the PC nanolayers away, at 40 ℃ for 1 day. Finally, supercritical drying was carried out in Tousimis Autosamdri 815B to replace the chloroform by carbon dioxide (CO_2). Typical SEM photos are shown in Fig.7.3.

A main issue of PA nanoPAM was that its visual transmittance and haze were poor. The possible reasons include 1) the instability of polymer A nanolayers, associated with thermal mismatch, internal stress, and swelling in solvent; and 2) the light scattering by the remnant of polymer B materials. In the future, we plan to 1) process new materials with higher dimensional stability, e.g. polyamide (PA) and polyvinylidene difluoride (PVDF); 2) perform a detailed parameterized study to optimize the coextrusion process, to minimize the internal stresses and thermal mismatch; 3) optimize the solvent and the etching setup to fully remove material B; 4) use AR coating to reduce the surface defects and also to improve the optical properties; 5) use corona charging to improve the layer separation.

References

[1] C.L. Choy, Thermal conductivity of polymers, Polymer (Guildf). 18 (1977) 984–1004.

[2] S. Zhang, D.B. Bogy, A heat transfer model for thermal fluctuations in a thin slider/disk air bearing, Int. J. Heat Mass Transf. 42 (1999) 1791–1800.

[3] M. Ponting, A. Hiltner, E. Baer, Polymer nanostructures by forced assembly: process, structure, and properties, in: Macromol. Symp., Wiley Online Library, 2010: pp. 19–32.